



HAL
open science

Thermo electric properties of nanocomposite materials

Chandan Bera

► **To cite this version:**

Chandan Bera. Thermo electric properties of nanocomposite materials. Other. Ecole Centrale Paris, 2010. English. NNT: 2010ECAP0027 . tel-00576360

HAL Id: tel-00576360

<https://theses.hal.science/tel-00576360>

Submitted on 14 Mar 2011

HAL is a multi-disciplinary open access archive for the deposit and dissemination of scientific research documents, whether they are published or not. The documents may come from teaching and research institutions in France or abroad, or from public or private research centers.

L'archive ouverte pluridisciplinaire **HAL**, est destinée au dépôt et à la diffusion de documents scientifiques de niveau recherche, publiés ou non, émanant des établissements d'enseignement et de recherche français ou étrangers, des laboratoires publics ou privés.

Thermo Electric Properties Of Nanocomposite Materials

By

Chandan Bera

Laboratoire d'Énergétique Moléculaire et Macroscopique, CNRS
UPR 288, France
Ecole Centrale Paris

Under the supervision of

Sebastian Volz

Laboratoire d'Énergétique Moléculaire et Macroscopique, CNRS UPR 288,
Ecole Centrale Paris, France

Natalio Mingo

CEA, LITEN, 17 rue des Martyrs, BP166, 38042 Grenoble, France

Doctoral committee :

Dr. Natalio Mingo, LITEN, CEA, Grenoble, France

Prof. Sebastian Volz, EM2C, CNRS UPR 288, Ecole Centrale Paris, France

Dr. David Lacroix, Laboratoire d'Énergétique et de Mécanique Théorique et
Appliquée, Nancy, France

Dr. Olivier Bourgeois, Institut Néel, CNRS-UJF, 25 rue des Martyrs, BP166,
38042 Grenoble, France

Prof. Claude Godart, CNRS, ICMPE, CMTR, 2/8 rue Henri Dunant, 94320
Thiais, France

Acknowledgments

I was extremely fortunate for the opportunity to work with, learn from, and establish friendships with some of the finest people during my time in EM2C, Paris and in LITEN, CEA-Grenoble. First and foremost, I would like to thank my advisor, Professor Sebastian Volz and Professor Natalio Mingo for their support, energy, encouragement, and timely and insightful advice over the past three years. This dissertation would have been considerably more difficult and not nearly as complete without their guidance. I am grateful to them for their invaluable advising and for providing me with so many opportunities to learn new things.

I would like to thank other members of the LITEN-Thermoelectricity group: Dr. Marc Plissonnier, Dr. Emmanuelle Rouviere, Dr. Christele Navone, Dr. Julia Simon for giving me good direction and advice on my research. I would also like to thank my committee members Dr. David Lacroix, Dr. Olivier Bourgeois and Dr. Claude Godart for being a part of my thesis committee.

I am greatly thankful to Christele Navone for providing me samples for characterization and I greatly appreciate the assistance of Michael Bozlar with thermal characterizations of my samples and also thankful to Prof. Jinbo Bai for allowing me to work in his lab.

I would also like to thank David Hauser, Guillaume Savelli, and Mathieu Soulier who are great friends in addition to being labmate. I will always remember our passionate yet funny discussions on lot of subjects everyday in lab and sometime over the week end and their never ending efforts on teaching me French. I would also like to acknowledge the assistance and efforts offered by my labmates Emmanuel Rousseau, P.O. Chapuis, J-N Gillet, Yann Chalopin, Zhao wang, Shidong wang, Ivana Savic for sharing their knowledge and helping me during my stay in Paris and Grenoble. I am very much thankful to Zhao for providing me lot of help during my thesis writing.

I would like to thank my friends who always encouraged me and were very supportive of my Ph.D.: Abhijit Ghosh, Akash Chakraborty, Ananda shankar Basu, Anita Sarkar, Arpan krishna Deb, Arijit Roy, Ayan Bandyopadhyay, Biplab Bisaws, Kuheli Bandyopadhyay, Kalpana Mondal, Priyadarshini Chatterjee, Soumen Mondal, and Subhadeep Datta. I will always remember their help and support during my stay in Grenoble.

Finally, I wish to acknowledge my family who is always there to support me. I will always be indebted to my parents for their unconditional love and care, and for teaching me all the good values in life.

Dedication

To my parents

Contents

Acknowledgments	iii
Dedication	v
1 Introduction	3
1.1 Introduction on thermoelectricity	3
1.1.1 Thermoelectric device efficiency	5
1.1.2 Nanostructure for thermoelectric efficiency	7
1.2 Basic concepts in electron and heat transport	8
1.2.1 Electron Transport in Bulk Materials	8
1.2.1.1 Crystal Structure	8
1.2.1.2 Energy Band	9
1.2.1.3 Electron Scattering	12
1.2.1.4 Kinetic theory of Electron Transport	13
1.2.2 Phonon Transport in Bulk Materials	14
1.2.2.1 Phonon dispersion curves	14
1.2.2.2 Phonon energy	15
1.2.2.3 Phonon Scattering	17
1.2.2.4 Phonon thermal conductivity	19
1.2.3 The Boltzmann Transport Equation	20
1.3 Nanoscale Heat Transfer: State of the art	22
1.4 Objectives	24
2 Thermal Conductivity of Porous Materials	27
2.1 Introduction	27
2.2 Monte Carlo Method	30
2.2.1 MC simulation for porous materials	31
2.2.1.1 Initial conditions for MC	32

2.2.1.2	Phonon drift	34
2.2.2	Mean Free Path by MC method	35
2.3	Analytical method for the MFP calculation of Porous materials	38
2.4	Thermal Conductivity Calculation	41
2.4.1	Relaxation time approximation	41
2.4.2	Thermal conductivity of bulk materials	44
2.4.3	Thermal conductivity of porous materials	45
2.5	conclusion	51
3	Thermal Conductance of Nanowires	53
3.1	Introduction	53
3.2	Conductance of nano wire	55
3.2.1	Landauer Equation and Quantum of thermal conductance	55
3.2.2	Transmission function	56
3.2.3	Mean free path	58
3.2.4	Surface roughness	59
3.3	Transmissivity calculation by MC Simulation	61
3.4	Results	64
3.5	Conclusion	68
4	Thermo Electric Properties of SiGe NanoPowder	69
4.1	Introduction	69
4.2	Thermal Conductivity	72
4.2.1	Experimental Measurement	72
4.2.2	Theoretical model of Lattice Thermal conductivity	75
4.3	Electrical Properties	76
4.3.1	Experimental Measurement	76
4.3.2	Theoretical model for the Electrical Properties	76
4.4	Results	81
4.4.1	Modelling of Bulk Materials	81
4.4.2	Modelling of Nanograined sintered materials	88
4.4.3	Characterization and Modelling of larger grain sintered materials	91
4.4.4	The potential for further ZT improvement in nanograined SiGe	93
4.5	Conclusion	98
5	Conclusions and Future Work	101
5.1	Conclusions	101
5.2	Future Direction	103

A Appendix	105
Bibliography	111
Résumé	123
Abstract	125

Contents

1.1 Introduction on thermoelectricity	3
1.1.1 Thermoelectric device efficiency	5
1.1.2 Nanostructure for thermoelectric efficiency	7
1.2 Basic concepts in electron and heat transport	8
1.2.1 Electron Transport in Bulk Materials	8
1.2.1.1 Crystal Structure	8
1.2.1.2 Energy Band	9
1.2.1.3 Electron Scattering	12
1.2.1.4 Kinetic theory of Electron Transport	13
1.2.2 Phonon Transport in Bulk Materials	14
1.2.2.1 Phonon dispersion curves	14
1.2.2.2 Phonon energy	15
1.2.2.3 Phonon Scattering	17
1.2.2.4 Phonon thermal conductivity	19
1.2.3 The Boltzmann Transport Equation	20
1.3 Nanoscale Heat Transfer: State of the art	22
1.4 Objectives	24

1.1 Introduction on thermoelectricity

During the last two decades, increasing demand for energy and pollutants free environments has led to continuous investigation of leading-edge technological products with high energy efficient performance and low fabrication costs. World wide research

on the thermoelectric(TE) materials for their various applications, has been giving a constant improvement to the technology.

This new century has already witnessed various new technologies in the nano science field. Nanotechnology brings a lot of new disigns in the field of material science [1, 2, 3, 4]. This new field gives the ability to decrease the size of devices, together with the improvement of their efficiency. Recently, we have strong improvements of the thermoelectric material properties due to the nanostructuring of bulk materials [5, 6, 7, 8]. The systems based on these thermoelectric materials are expected to upgrade energy efficiency and to decrease pollutants. These devices will have vast application in automotive, microelectronics, space research and many other fields [9]. The following Figure.1.1 is an application of TE generator in automotive industry.

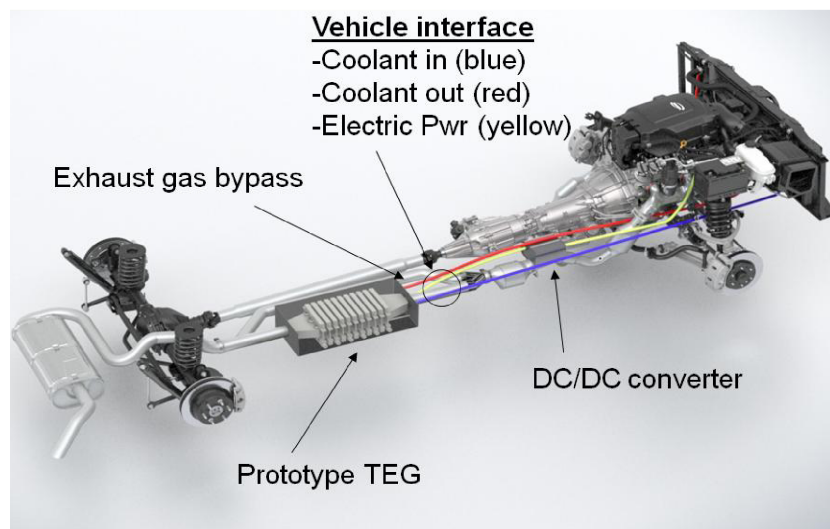


Figure 1.1: A prototype of TE generator in vehicle, which will convert energy from the heat loss.

Such technological innovations have been based on the numerous works in the field of transport properties of materials. Performance and efficiency of thermoelectric devices have been largely increased by improving the transport properties of materials and discovering new materials. The basic TE device consists in the Peltier pump or the TE cooler, which we present in the next section.

1.1.1 Thermoelectric device efficiency

A schematic diagram of thermoelectric cooler is shown in Fig.1.2.(A), from which several desired material properties become clear. This cooler (also known as Peltier cooler) is made of two legs, one of which is *n*type and contains mobile electrons and the other leg is *p*type which has positive charges called holes. These two legs are connected electrically in series and thermally in parallel. When the current is passed through the legs along the direction shown, both the electrons and holes flow away from the top of the device towards the bottom and carry heat from the junction at the top of the device towards the base, cooling the junction at the top.

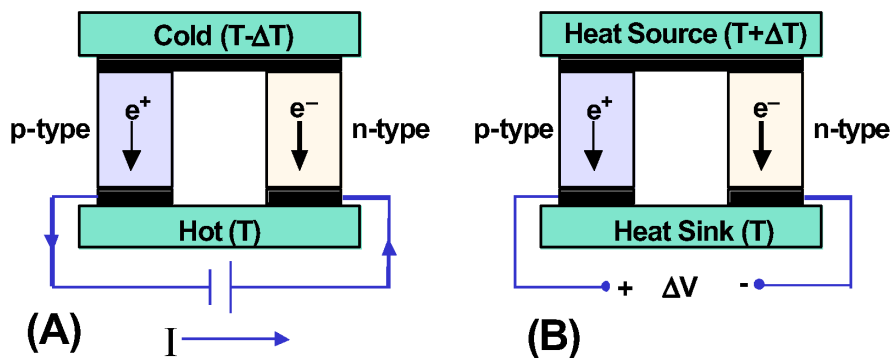


Figure 1.2: (A) A schematic diagram of thermoelectric cooler. Two electrically conducting legs are connected by a metal (black bar) at the top to make a junction. The right leg is "n-type" and contains mobile electrons and the left leg is "p-type" which has positive charge called holes. When the current passes as the direction shown, both electrons and holes flow away from the top of the device towards the bottom. In this process they carry energy in the form of heat from the cold side to hot side. (B) Instead of passing current through the device, a temperature gradient can be created by applying two different temperatures on the two sides to produce a voltage difference as shown.

Thermoelectric generator is the opposite of a Peltier cooler. Thermoelectric gen-

erator as demonstrated in Fig.1.2(B), generate power in the presence of an externally generated temperature gradient. In this case, both carriers conduct heat from the heated junction at the top to the cooled side at the base, and a voltage drop is generated between the electrode at the bottom.

In addition to cooling the top junction when the current is passed, there will be Joule heating in each leg. The amount of Joule heating is equal to the square of current times the electrical resistance of the materials. Therefore materials with low resistivity are required. Additionally to prevent the back flow of heat from hot to cold junction materials, low thermal conductivity is necessary. The final important parameter is Seebeck coefficient, which measure from the voltage generated across the material due to a temperature difference. From the above thermoelectric power generator (TEG) example, it is clear that large Seebeck coefficient is desired to maximize the voltage output for a given temperature drop. The voltage (V) generated by a TEG is directly proportional to the number of couples (N) and the temperature difference (ΔT) between the top and bottom sides of the TEG and the Seebeck coefficients of the ntype and ptype materials (S_n and S_p respectively).

$$V = N(S_p - S_n)\Delta T \quad (1.1)$$

Power output from a TEG is defined as,

$$\eta = \frac{T_h - T_c}{T_h} \frac{\sqrt{1 + ZT} - 1}{\sqrt{1 + ZT} + T_c/T_h}, \quad (1.2)$$

where T_h and T_c are the hot junction and cold junction temperature, T is the average temperature of the system between T_h and T_c and ZT is the dimensionless figure of merit of the TE materials which is used in the power generating device. ZT is defined as,

$$ZT = \frac{\sigma S^2 T}{\kappa} \quad (1.3)$$

where σ refers to the electrical conductivity, S represent to the Seebeck coefficient and κ corresponds to the thermal conductivity. To get an optimum device performance this figure of merit should be maximized. Materials with highest Seebeck coefficient, in general have low thermal conductivity but are also poor conductor of electricity. On the other hand, metals have high electrical conductivity but thermal conductivity also very high and Seebeck coefficient is small. The properties of Semiconductors which lie between metals and insulators are best for these three TE properties.

1.1.2 Nanostructure for thermoelectric efficiency

In the early stage of semiconductor physics it was mainly studied for the applications on thermoelectric rather than the applications in microelectronics. Almost every semiconductors were investigated for their potential application in TE. At the end of 1950's the best thermoelectric materials were found to be alloy of Bismuth telluride and Antimony, with ZT close to unity. After that few improvements on the ZT were achieved during the next forty years. In the early 1990's, by using nanotechnology we have noticed strong improvement on ZT and the new discovery show that nanostructure materials have better ZT compared to bulk materials.

In the following plot, we can observe the recent improvements of thermoelectric figure of merit, ZT for both *p*-type and *n*-type materials which was under unity during half a century.

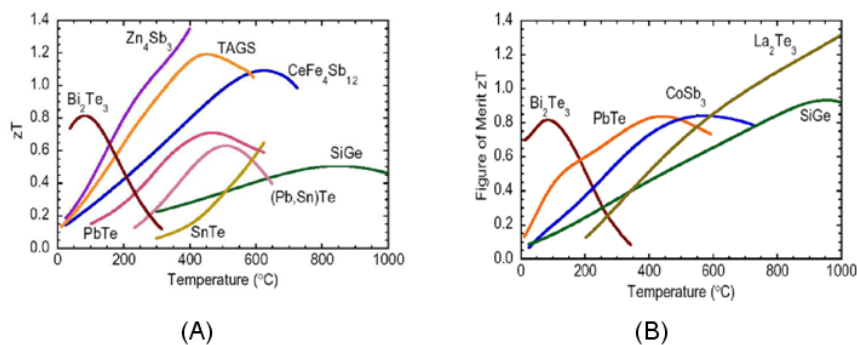


Figure 1.3: (A) *p*-type materials. (B) *n*-type materials.

In 1990's, Hicks, Dresselhaus and Harman suggested[10, 11] that the figure of merit could be improved if electrons were to be confined in two dimensions using so called quantum well superlattices, where superlattices are multilayers of thin films on the order of several nanometers in thickness. Hicks and Dresselhaus later extended their work to include one-dimensional conductors such as nanowires[12]. The primary reason for the enhancement in the figure of merit in these low-dimensional structures is through an increase in the electronic density of states per unit volume, which leads to an improved thermopower. However, low-dimensional structures often exhibit a reduced thermal conductivity when compared to bulk materials[13]. In fact, in some instances, the benefits came from the suppressed thermal conductivity which may outweigh any gains due to electron confinement. To study the thermoelectric

properties, we need a detailed knowledge on the transport properties, such as mobility, diffusivity, carrier lifetime, and surface effect, which will be now presented.

1.2 Basic concepts in electron and heat transport

1.2.1 Electron Transport in Bulk Materials

The transport properties of electron in a material are related to the energy band structure and the nature of collision processes. Again the characteristics of the energy band structure are related with the crystal structure.

1.2.1.1 Crystal Structure

Crystal structure is composed of a pattern, a set of atoms arranged in a particular way, and a lattice exhibiting long-range order and symmetry. Patterns are located upon the points of a lattice, which is an array of points repeating periodically in three dimensions. The points can be thought of as forming identical tiny boxes, called unit cells, that fill the space of the lattice. The lengths of the edges of a unit cell and the angles between them are called the lattice parameters. The symmetry properties of the crystal are embodied in its space group. Most of the useful and well-known compound semiconductor have one of the three structure: that of zinc blende (also known as sphalerite), the wurtzite (also known as zincite) or rock salt (also called sodium chloride).

In Zinc blende structure an atom of one kind constituting binary compound is surrounded by four equidistant atom of another kind, which occupy the vertex of a tetrahedron, the atom of the first kind being at its center. The orientation of the neighbouring atoms is such that the atoms also occupy the sites of two interpenetrating face-centered-cubic (fcc) lattice. The arsenides, antimonides, and phosphides of aluminium, indium, and gallium among the III-V compounds and sulphides, selenides, and tellurides of cadmium, zinc, and mercury among the II-VI compounds have the zinc blende crystal structure. Most well-known semiconductor silicon and germanium have essentially the same kind of crystal structure, but the two atoms forming the basis being similar, this type of structure is also known as diamond structure, has inversion symmetry.

In the wurtzite structure the basis arrangement of atoms is similar to the in the sphalerite structure. An atom of one kind is surrounded tetrahedrally by four atoms of another kind, but the tetrahedrons are oriented so that the location of the atoms fit two interpenetrating close-packed hexagonal lattices. In the III-V compounds,

the relatively unknown crystals of nitrides of aluminium, indium, and gallium have wurtzite structures. Most of the II-IV compounds have both a wurtzite and a sphalerite modification.

The arrangement of atoms in the rock-salt structure is such that atoms of the two kinds occupy alternate positions on a face-centered-cubic lattice. It may also be considered as two interpenetrating parallel face-centered lattices. The important compound semiconductors having the rock-salt structure are the sulphides, selenides, tellurides and lead. The band structure of these materials have broad similarity with those of the sphalerite and wurtzite structure, however due to the differences in the lengths of the basis vector, there are also some significant differences, the most important in this will be the position of the valence band maxima and the shape of the associated constant energy surface.

1.2.1.2 Energy Band

The forms of the energy bands are determined by the crystal structure. Information related to the band structure is generally presented by plotting the energy of electron, E for the value of wave vector, \bar{k} , limited to within the first Brillouin zone[14]. When we consider the transport properties of different materials, we are mainly concerned with the extrema of energy band. For different materials the properties change depending on the position of these extrema of the band and on the effective mass, m^* , of the band[15].

The characteristics of the energy bands are usually indicated by plotting the energy eigenvalues of the electrons for different values of \bar{k} in the Brillouin zone. The crystal potential is different in different directions because of the differences in the spacing of the atoms. Therefore the values of E depends on both the magnitude and the directions of \bar{k} . In the case of transport problem, we are generally concerned with the lowest minima and the highest maxima as these are populated respectively by electrons and holes. From Fig.1.4, it is clearly understood that the conduction band is higher than the valence band, has minima at the zone center (Γ point) and one minima on the $\langle 111 \rangle$ direction and another on the $\langle 100 \rangle$ direction. The valence band, which is at below of the conduction band, which is separated by a energy gap for the insulator or semiconductor from conduction band, generally has a maxima at the zone center.

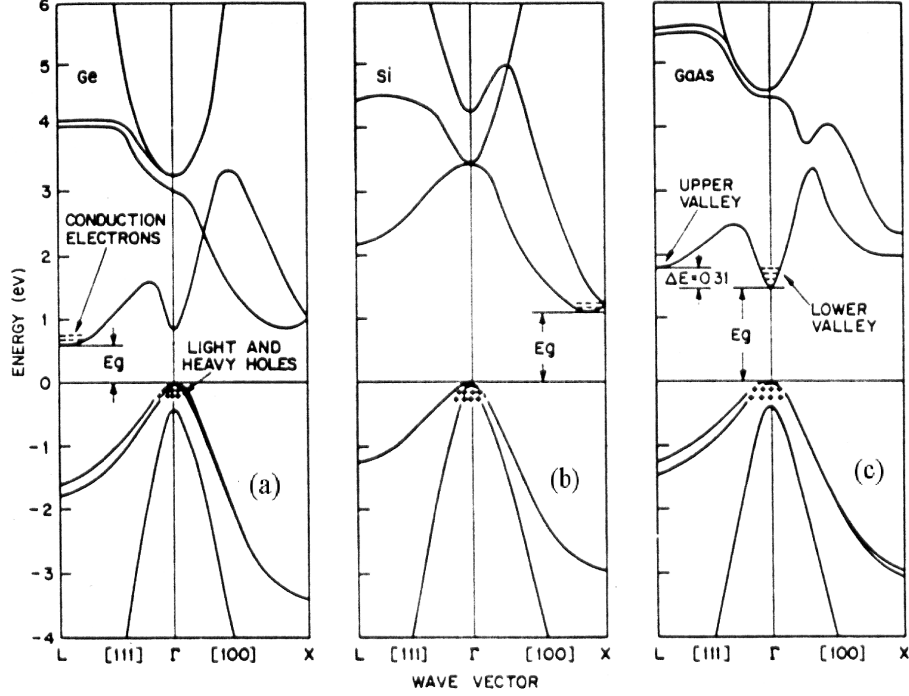


Figure 1.4: Energy band diagram of (a) germanium, (b) silicon and (c) gallium arsenide. Ref.[16]

If the energy E varies parabolically with $(\bar{k} - \bar{k}_0)$, where \bar{k}_0 is the values of \bar{k} at the extremum. The relation between E and \bar{k} at the Γ point can be expressed as[17]

$$E = \frac{\hbar^2 k^2}{2m^*} \quad (1.4)$$

where \hbar is the reduced Planck constant and m^* is the effective mass of these band. For the Γ - point, m^* is a scalar quantity.

The E and \bar{k} relation for the minima lying on the X and L directions is of the form

$$E = \frac{\hbar^2}{2} \left(\frac{k_l^2}{m_l} + \frac{k_t^2}{m_t} \right) \quad (1.5)$$

where k_l and k_t represents respectively the components of \bar{k} in a direction parallel to the direction of symmetry, measured from the position of the minimum, and in the transverse direction. The constant energy surface are spheroidal, and the shape of the

spheroid is generally prolate. The effective mass for these minima are tensor quantity, the tensor being diagonal, with diagonal quantity m_l , m_t , and m_t , when a direction of symmetry corresponding to the particular minimum is chosen as a reference axis.

In some cases the energy E for points in \bar{k} space away from the extrema varies nonparabolically with \bar{k} . In that case the nonparabolic E - \bar{k} relation can be written as [15],

$$E(1 + \alpha E) = \frac{\hbar^2 k^2}{2m^*} \quad (1.6)$$

where m^* is the effective mass for k tending to zero, and α is a constant which in many materials is approximately equal to $1/E_g$, E_g being the separation between the conduction band minimum and valence band maximum, i.e. band gap.

There are different methods to solve the energy band structure of materials. The detailed nature of the energy band may be worked out by solving the Schrödinger equation [15, 14]. There are also methods for the calculation of the band structure of the solid from first principles.

Electrons in the conduction band and holes in the valence band behave as free particles, and their distribution among the available energy levels, when in thermal equilibrium with the lattice, obeys Fermi-Dirac statistics. For the parabolic band the number of electrons occupying a particular energy level is given by,

$$n = 4\pi \left(\frac{2m^*}{\hbar^2}\right)^{3/2} \int_0^\infty \frac{E^{1/2} dE}{1 + \exp[(E - E_F)/k_b T]} \quad (1.7)$$

where h is the Planck's constant and k_b is the Boltzmann constant. The density of states in the energy space varies as $E^{1/2}$.

Integral in Eqn.1.7 in general cannot be evaluated analytically. But when E_F is negative and $|E_F|$ is much larger than $k_b T$, i.e. when the material is non-degenerate, the Fermi function simplifies to the Maxwellian function. Then by neglecting 1 in comparison to $\exp[(E - E_F)/k_b T]$, we get:

$$n = 2 \left(\frac{2\pi m^* k_b T}{\hbar^2}\right)^{3/2} \exp(E_F/k_b T) = N_c \exp(E_F/k_b T) \quad (1.8)$$

But in the degenerate case when E_F is positive and is not much lower than $k_b T$ of band edge, the integral has to be evaluated numerically. The integral in Eqn.1.7, can be written as:

$$n = N_c \frac{2}{\sqrt{\pi}} \int_0^{\infty} \frac{x^{1/2} dx}{1 + \exp(x - \eta)} = N_c F_{1/2}(\eta) \quad (1.9)$$

The integral in the above form is often called Fermi integrals, where $x = E/k_bT$ and $\eta = E_F/k_bT$. The distribution function F_i is call Fermi-Dirac distribution function[10] and is defined for any index i as:

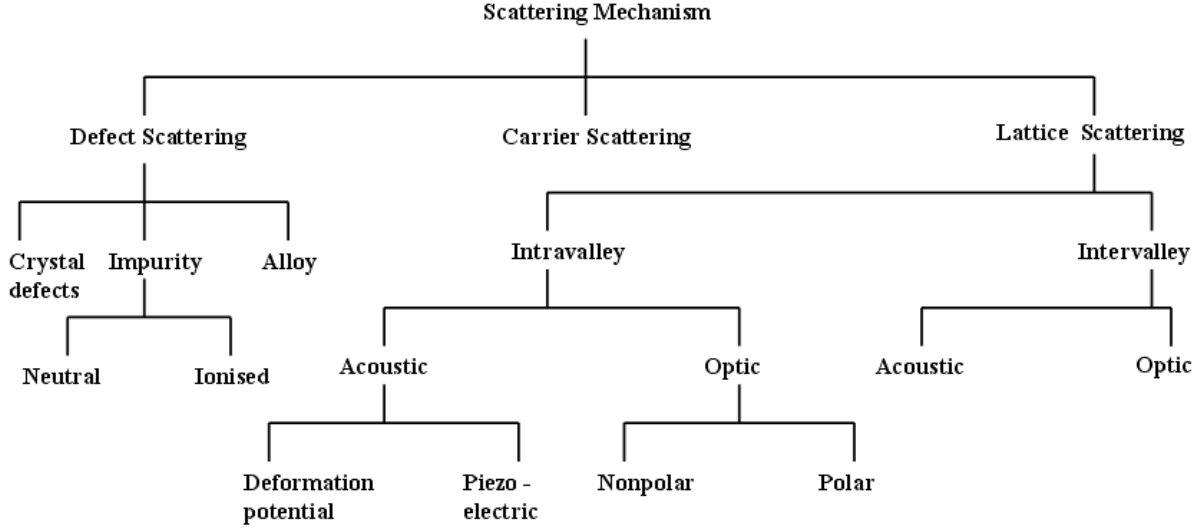
$$F_i = F_i(\eta) = \int_0^{\infty} \frac{x^i dx}{1 + \exp(x - \eta)} \quad (1.10)$$

From Eqns 1.7 and 1.9 we can relate the concentration of electron to the Fermi energy and to the density of states. Later we can determine the position of Fermi level for different impurity concentrations and temperature.

1.2.1.3 Electron Scattering

The motion of an electron is unhampered in a perfect crystal, in which the wave function of the electron is given by stationary Bloch functions, and the application of an external field would uniformly accelerate the electron causing a linear increase of the drift velocity with time in the direction of the field. But such linear increase in drift velocity with time does not occur in real crystals. The average drift velocity of the electron reaches a limiting value, which at low field will be proportional to the magnitude of the field. The limit is set by the interaction of the electron with the imperfection of the crystal through the process referred as scattering or collision processes. The electron continues to be in a stationary state until it comes close to an imperfection. After it interacts with the imperfection, the electron has a new wave function characterized by new wave vector and often different value of energy.

In a lattice crystal, there are different type of scattering mechanisms for different imperfection. The important of each kind of scattering varies from material to material, it also depends on temperature and carrier concentrations. Later we will discuss the importance electron scattering mechanism for Si, Ge, and SiGe alloy. In the bellowing Fig.1.5 we gave a list of all kind of electron scattering mechanisms.

Figure 1.5: *Electron scattering Mechanisms*

1.2.1.4 Kinetic theory of Electron Transport

After having defined the scattering mechanisms for different kind of materials, we have to know the different macroscopic transport coefficient to calculate the transport properties of the material. In the simplest kinetic method we can define some macroscopic properties of the materials by considering electron as a particle and following the motion of one of them at a time. Here the particle scattering is governed by the characteristic relaxation time τ when a particle collide with impurity or interact with phonons. For n electron per unit volume, we can define the electric current as,

$$\mathbf{J} = ne\bar{\delta v} = \frac{ne^2v\tau}{\partial E/\partial v}\mathbf{E} \quad (1.11)$$

where $\bar{\delta v}$ is the average drift velocity parallel to the Electric field \mathbf{E} . Now macroscopic relation defining the electrical conductivity, σ , Eqn.1.11 becomes,

$$\mathbf{J} = \sigma\mathbf{E} \quad (1.12)$$

Therefore,

$$\sigma = \frac{ne^2v\tau}{\partial E/\partial v} = \frac{ne^2\tau}{m^*} \quad (1.13)$$

In terms of electron mean free path, l_e , where $l_e = \tau v$, the electrical conductivity becomes,

$$\sigma = \frac{ne^2 l_e}{m^* v} \quad (1.14)$$

We can also relate the mobility(μ) of the material with the relaxation time and the carrier concentration, n as,

$$\mu = \frac{e\tau}{m^*} \quad (1.15)$$

because $\sigma = ne\mu$

1.2.2 Phonon Transport in Bulk Materials

In solid materials, heat is transported by the atomic lattice vibration, called phonons and charge carriers such as electrons and holes. The contribution of charge carriers in heat transport was discussed in earlier section. The electronic contribution explains the fact that good electrical conductors also have high thermal conductivity. Although electronic contribution in thermal conductivity is significant for highly doped materials and metals, the lattice contribution remains dominant in dielectric and semi-conductor materials.

1.2.2.1 Phonon dispersion curves

Atoms in solid are held together as a lattice by a chemical bond between them. These bonds are not rigid, but act like a spring which connects the atoms, by creating a spring-mass system as shown in Fig.1.6. When an atom or plane of atoms displace, this displacement can travel as a wave through the crystal, transporting energy as it propagate [18]. This wave can be longitudinal where the displacement of atoms are in the same direction of wave, or they can be transverse where in the three dimensional case the displacement of atoms are in the perpendicular direction of the wave propagation. These lattice vibrations are quantized and known as phonons.

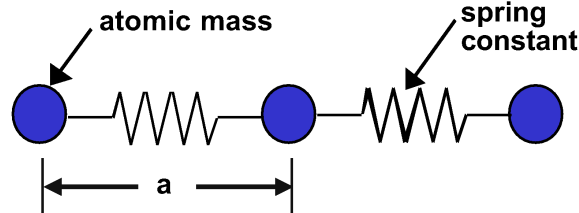


Figure 1.6: One dimensional representation of atoms and chemical bond as spring mass system. The chemical bond act as a spring and atom as mass. The distance between two adjacent atom is called lattice constant and represented by, a .

By solving equation of motion for these waves, we can determine the angular frequency of the waves (ω) for its different wave length (λ) or wave number (also called wave vector) (k), where $k = 2\pi/\lambda$. The relationship between k and ω is called the dispersion relation. From the slope of the dispersion relation, one can determine the speed of propagation of phonons, ($\frac{\partial\omega}{\partial k}$), which is also called group velocity. For a crystal that has at least two atoms in a unit cell (which may or may not be different), the dispersion relations exhibit two types of phonons, namely, optical and acoustic modes corresponding to the upper and lower sets of curves in the Fig1.7, respectively. The vertical axis is the energy or frequency of phonons, while the horizontal axis is the wave-vector.

Since the group velocity of the acoustic phonons is much larger than the one of optical phonons, the contribution in the thermal conductivity is mostly came from acoustic branch.

1.2.2.2 Phonon energy

As the dispersion relation of the phonon is known, one can determine the thermal properties of solid from there. The entire set of all possible phonons that are described by the above phonon dispersion relations combine in what is known as the phonon density of states which determines the heat capacity of a crystal. We consider our solid as an assembly of $3NV$ independent harmonic oscillators, one for each lattice mode, is capable of taking up one or more quanta of energy. Therefore phonons are 'Bose-Einstein particles' of which any number may go to any given energy level. The

equilibrium number of phonons with a polarization p and wave vector \mathbf{k} is given by

$$\langle n_{\mathbf{k},p} \rangle = \frac{1}{\exp\left(\frac{\hbar\omega}{k_b T}\right) - 1} \quad (1.16)$$

where k_b is the Boltzmann constant, and T is the temperature.

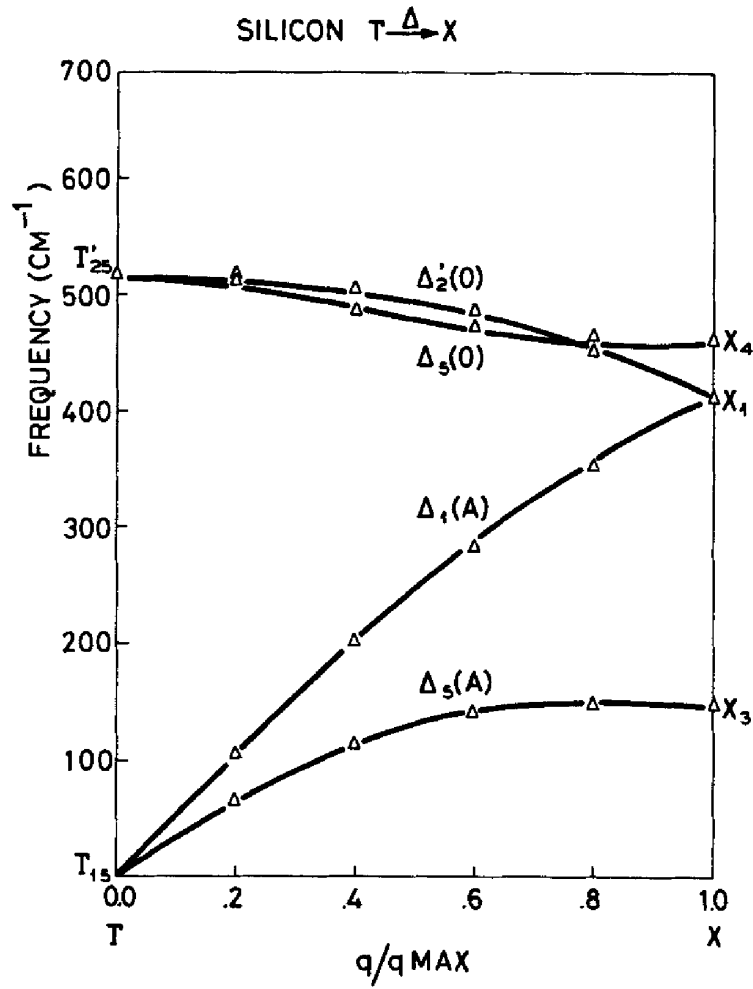


Figure 1.7: Dispersion relation of phonon. Ref[19]

The average energy of this mode is [20]

$$E = \sum_p \sum_{\mathbf{k}} (\langle n_{\mathbf{k},p} \rangle + \frac{1}{2}) \hbar \omega \quad (1.17)$$

Crystal volumic energy, E is obtained by summarizing each quanta $\hbar \omega$ over the two polarizations of phonon for longitudinal and transverse of acoustic and optical modes. Assuming that phonon wave vector \mathbf{k} are sufficiently dense in \mathbf{K} space, the summation over \mathbf{k} may be replaced by an integral[21],

$$E = \sum_p \int_{\omega} (\langle n_{\mathbf{k},p} \rangle + \frac{1}{2}) \hbar \omega D_p(\omega) g_p d\omega \quad (1.18)$$

where $D_p(\omega)d\omega$ is the number of vibrational mode in the frequency range $[\omega, \omega + d\omega]$ for polarization p and g_p is the degeneracy of the considered branch.

1.2.2.3 Phonon Scattering

When different kind of phonon wave propagate through the lattice, it is disrupted or scattered by the defects or dislocations, crystal boundary, impurities such as dopant or alloying components, or by interaction with another phonons. These different type of scattering can be divided in two groups, one elastic scattering where the frequency does not change after the scattering and another inelastic scattering where frequency changes after the scattering. The distance or the path traveled by phonon between two scattering event is generally defined by the phonon mean free path, l_p . Where

$$l_p = v\tau \quad (1.19)$$

v is the phonon velocity and τ is the relaxation time of the scattering events. Each scattering event has its own mean free path which depends on the materials and the temperature.

1. Normal and Umklapp Scattering. Inelastic scattering process arises due to the fact that forces between atoms are not purely harmonic. There are two types of phonon-phonon scattering, one is Normal and another is Umklapp which are generally referred as N and U scattering process. Normal scattering process is shown in Fig.1.8

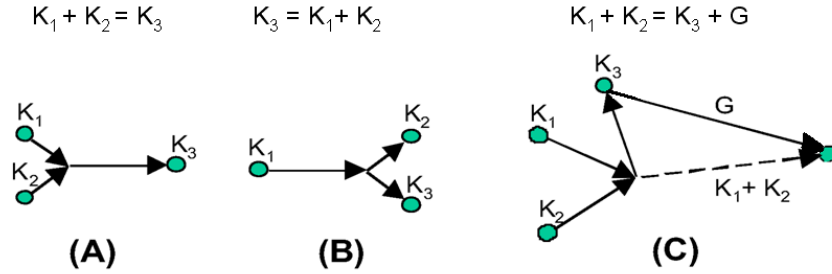


Figure 1.8: (A) Vectorial representation of a Normal phonon scattering where two phonons combine to create a third. (B) Normal processes where one phonon scatters into two phonons. (C) Umklapp processes where two phonons combine to create a third. Due to the discrete nature of the atomic lattice there is a minimum phonon wave length, which corresponds to a maximum allowable wave vector. If two phonons combine to create a third phonon which has wave vector greater than this maximum, the direction of the phonon will be reversed with a reciprocal lattice vector G , such that its wave vector is allowed. Ref.[22]

Where two phonons K_1 and K_2 interact with each other and produce another phonon K_3 or one phonon can be scattered into two phonons. In this scattering mechanism the phonon momentum does not change, so it does not put any resistance in the heat transport.

The Umklapp phonon scattering mechanism is described in Fig.1.8.(C), where after the scattering, new phonons may cross the first Brillouin zone and the momentum direction after the scattering is changed. Umklapp scattering is the dominant process for thermal resistivity at high temperatures for low defect crystals.

2. Scattering by defects, impurities, and boundary. In addition to phonon-phonon interaction, there may be phonon scattering by the imperfections in the crystal lattice. This imperfection may be due to the defects in the crystal, or due to impurities and the boundary of the crystal.

In the crystal lattice, imperfection occurs due to various reasons. All kinds of imperfection mostly have the same effect, i.e. reducing the heat transport. The types of defects are classified as isolated point imperfections (i.e., vacancies, chemical impurities, isotopes), line imperfections (typically dislocation), surface imperfections, e.g., grain boundaries, twin boundaries and stacking faults and

volume disorder as in the case of alloys [18].

Defects or dislocation in the atomic lattice have an effect as acting as different spring and mass constant to the incident phonon. The speed of sound related to the elastic stiffness(C) of the chemical bond is defined by the following equation,

$$v = \sqrt{\frac{C}{\rho}} \quad (1.20)$$

where ρ is the mass density and v is the speed of sound. So when a phonon encounters a change in mass or elastic stiffness, it scattered. The impurity atoms inside the host matrix with different mass and spring constant produced a disruption in the phonon transport. These impurity atoms can be in the form of dopant atoms or from the species introduced to form an alloy. Alloying is a very effective way to reduce thermal conductivity due to this kind of scattering.

The role of boundary scattering in limiting the phonon mean free path has long been considered as low temperature phenomena. Where in absence of other phonon scattering mechanism, boundary scattering observe as phonon mean free path approaches the sample dimensions[23]. As in the recent years interest has grown in the used of hot-pressed highly doped materials for the use in thermoelectric application, there are significant contribution from the boundary scattering as in the solid large proportional of heat was carried by low frequency phonons, boundary scattering effects can manifest themselves at high temperatures[24]. We will discuss the boundary scattering for different structure in details in chapters *II* and *III*.

1.2.2.4 Phonon thermal conductivity

In the kinetic formulation of thermal conduction, we can define the heat flux, \bar{q} , as equal to the product of thermal conductivity, κ and the negative local temperature gradient, $-\nabla T$. The heat flux is the amount of energy that flows through a particular surface per unit area per unit time. The final relation is also called Fourier's Law of thermal conduction.

$$\bar{q} = -\kappa \times \nabla T \quad (1.21)$$

Now if we suppose that each particle has an atomic heat capacity c , so that it requires an energy $c\delta T$ per particle to change the local temperature of the assembly by an amount δT and each particle traveling with a velocity v from one region to another

region. If the motion of one particle is unrestricted for a time t , the contribution of this particle to the thermal current per unit area, \bar{q} , will depend on the distance vt that it crosses before it is scattered. The average value of this over all particles is $v\tau$, where τ is the relaxation time. Summing over all the particles, we can write the heat current as

$$\bar{q} = -nc\tau\bar{v}^2 \cdot \nabla T, \quad (1.22)$$

where n is the total number of particles. Now the thermal conductivity, κ , is

$$\kappa = \frac{1}{3}C_p\bar{v}l_p \quad (1.23)$$

since nc corresponds to the total specific heat C_p , and l_p is given by Eqn.1.19.

From the Eqns 1.14 and 1.23 we can calculate very easily some important properties of material. From these two equations, we can also calculate the mean free path of the carriers without knowing details scattering mechanisms. By assuming $l_e = l_p$ we can write,

$$\frac{\kappa}{\sigma} = \frac{C_p m^* v^2}{3ne^2} \quad (1.24)$$

For the classical gas, where $\frac{1}{2}mv^2 = \frac{3}{2}k_bT$ and the specific heat is $\frac{3}{2}nk_b$, Eqn.1.24 becomes [25],

$$\frac{\kappa}{\sigma} = \frac{3}{2} \left(\frac{k_b}{e} \right)^2 T \quad (1.25)$$

The ratio $\kappa/\sigma T$ is called the *Lorenz number* and should be a constant, independent from temperature and from the scattering mechanisms. Eqn.1.25 is in fact the well known *Wiedemann-Franz law*.

1.2.3 The Boltzmann Transport Equation

Instead of following one particle from collision to collision, it is much instructive to consider the system as a whole at a fixed time. We can assume the form of the distribution function, $f(r, k, t)$, probability that the state (r, k) will be found occupied by an electron, or phonon or by particles at time t . This statement violates uncertainty principle according to which both position and momentum of the electron can not

be specified at the same time. However in most transport problem, the position of the carrier need to be fixed at the macroscopic scale. We assume that r is fixed with an interval Δr and that the carrier is spread over δk in k such that $\Delta r \Delta k > 1$. Therefore the specification of r and k are correct in $f(r, k, t)$ within Δr and Δk . The distribution function can be changed due to following mechanisms:

(a) Diffusion. Carriers from adjacent region enter into r , whilst other leave, as a result of their spatial velocity v_k . If f varies from point to point, there will be a tendency for it to change with time, at each point, at the rate:

$$f'_{diff} = -v_k \cdot \frac{\partial f}{\partial r} \quad (1.26)$$

(b) External fields. In the presence of external force the distribution function change as the occupation number of the states k will change. The rate of change is defined as,

$$f'_{field} = -\frac{e}{\hbar} (E + \frac{1}{c} v_k \times H) \cdot \frac{\partial f}{\partial k} \quad (1.27)$$

(c) Scattering. All the scattering mechanisms have the effect of throwing carriers from one state to another. This process gives rise to a net rate of change, f'_{scatt} .

which is the difference between the rate at which the state k is entered and the rate at which carriers are lost from it.

Making balance, we can write for the total rate of change of the distribution function,

$$f' = f'_{diff} + f'_{field} + f'_{scatt} \quad (1.28)$$

In the steady state, $f' = 0$, so the resulting equation becomes:

$$-v_k \cdot \frac{\partial f}{\partial r} - \frac{e}{\hbar} (E + \frac{1}{c} v_k \times H) \cdot \frac{\partial f}{\partial k} = -f'_{scatt} \quad (1.29)$$

This is the *Boltzmann's equation* in its general form. When the Eqn.1.29 is solved for f we can derive the electric current density as follows:

$$\mathbf{J} = \int e v_k f dk \quad (1.30)$$

and the flux of energy is yielded according to:

$$\Phi = \int E_k v_k f dk \quad (1.31)$$

The main problem of solving the transport equation by this way is the difficulty to find the proper scattering term for each mechanisms. We need to add together the transition rate from all other states into the k th state, and these will depend on the occupation number of those states. There are different procedures such as relaxation time approximation [15], variational method [26], iteration method [27], and Monte Carlo method [28] to solve this equation by considering different scattering mechanisms for carriers. We will implement Eqn.1.29 in our next modeling and investigate the transport properties of different kind of materials and structures by considering different scattering mechanisms.

1.3 Nanoscale Heat Transfer: State of the art

There are various ways to improve thermoelectric properties of current materials, several of which are subjected in recent reviews [5, 29, 30, 31, 32, 33, 34]. One particularly interesting approach is nanostructuring. With the recent advancements in the fields of microfabrication and nanoscale characterization, it is now possible to grow and analyze materials with atomic layer precision [35, 36]. A better understanding of transport phenomena such as mass, charge, and heat is essential in designing and/or improving the performances of such nanoscale devices. Although charge and mass transport at nanoscales have been studied extensively owing to the emergence of fields such as microelectronics and chemical and biological sensors [37, 38, 39], by comparison nanoscale heat transport has received little attention. The second law of thermodynamics requires that irreversible charge and mass transport must always be accompanied by heat transport with the environment. This heat transport may be useful or detrimental to the performance of the nanoscale device. Therefore, a detailed study of heat transport at the nanoscale is critical in improving the performance of low-dimensional devices [40].

Nanostructured materials (such as nanowire, nanotube, nanoparticles, nanofilms, superlattices) properties could be modulated by changing the density, nature and the ordering of the included nanostructure to obtain the best properties [41]. As we have discussed before, for the TE application, we need the materials with good electrical conductivity and low thermal conductivity which we can obtained by using superlattices [42], nanowires [43] and nanoparticles [44]. Heat conduction in nanostructure is also not same as in the macroscopic systems. Heat conduction calculation

in these nanostructured materials span the range from the numerical solution based on the Fourier's law [45] to the calculation based on the BTE [18, 46] to atomic level simulation. While in some cases (e.g., anharmonic phonon effects, isotopic defects, and point defects) understanding is well-developed, in others (e.g., interfaces, size effects of nanoparticles) current understanding is poor. In the nanostructure materials, there are non-Fourier effect due to nanometer size and the interfaces. To handle with these non-Fourier effects, there are models established depending on the Green-Kubo approach [47] in which the equilibrium fluctuations in the heat current are analyzed, the direct method such as Monte Carlo (MC) method[28], which mimics experiment by imposing a temperature gradient on the system and determining the thermal conductivity from Fourier's Law. MC method is very advantageous in the calculation of the boundary scattering and size effect. Modeling of the heat transport in complex nanostructure geometries was reported in publications[21, 48, 49] using MC method. In the next chapter we have discussed in details the physical properties of the nanocomposites using the MC method and an analytical approach.

Understanding of heat transport in nanowires is still in the primitive stage. Though only in past few years the growth of dense nanowire arrays become repeatable, the technique to measure the thermal conductivity of the single nanowire have only been recently developed [50, 51, 52]. As a result very little data is available in literature.

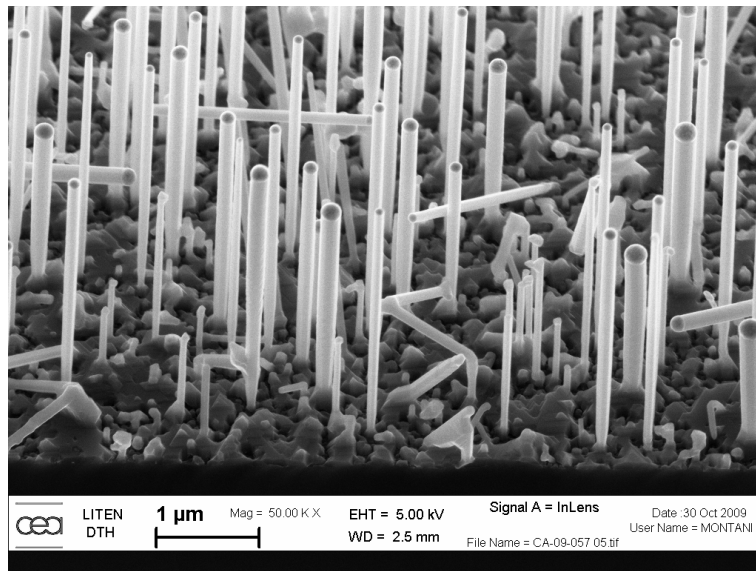


Figure 1.9: The array of nanowires was fabricated with CVD tool in CEA-Grenoble.

Though the physics of one dimensional electron transport is well understood in

the theoretical framework of Landauer theory [53, 54, 55], the phonon transport is very recently addressed in a few publications [56, 57, 58]. Some recent publications have also shown that nanowires could have a promising potential in thermoelectric applications [10, 59]. Still there are a lot of lacks of knowledge on the phonon transport which very much depends on the structure and surface of the wire. If we can control the heat transport mechanism from the fundamental approach, we can expect to achieve the best devices as per requirement.

1.4 Objectives

My works aim to develop a complete understanding of heat transport of porous materials at nanometer length scale, for which we need to understand different mechanisms that govern phonon transport in this scale. At the nanoscale, the mean free path and wavelength of different heat carriers become comparable to the size of the devices or structures themselves. Interface effects also become dominant and play a major role in defining the thermal characteristic of devices or structures. As we have seen in the publication by Mingo. et. al. [60], the presence of nanoparticle can increase the figure of merit 5 times of SiGe alloy at room temperature. This enhancement is mainly due to the large reduction of the thermal conductivity. This example illustrates the importance of understanding the transport in composites materials.

In this dissertation, I examine the heat transport in three dimensional (3D) nanoporous composites and nanowires. There is an ongoing debate in the research community regarding the size effect of the phonon transport in the composites materials. If we change the size of the embedded materials in the host matrix keeping the volume ratio fixed, the distance between the two phases and the view factor will also change and that could be affected the thermal transport. A numerical model was made to investigate the size effect in the transport properties.

My second research task involves studying the over all thermoelectric properties of the nanocomposites materials by considering different scattering mechanisms for the charge carriers and phonons comparing with the new and old experimental results. In much of the previous work many important parameters were varied between the measurement of different samples making it difficult to understand which parameters and hence which mechanisms are important. In this work, we have investigated all the mechanisms in details to present a best model for the thermoelectric properties.

This thesis manuscript is divided in the bellowing chapters:

In the 2nd chapter we will present in details the numerical method (Monte Carlo technique) used to obtain the mean free path of the porous materials together with an analytical model and we will calculate thermal conductivity of alloy and non-alloy

porous materials.

There will be a brief description of phonon transport in nanowire in the 3rd chapter. Ballistic phonon transport will be studied by using Monte Carlo Simulation. We will also discuss on how much phonon transmission can be restricted by engineering the nanowire shape.

The 4th chapter of this manuscript will focus on the thermoelectric properties of the SiGe alloys and also its individual components, i.e., Si and Ge. Here we will discuss the carrier mobility of these materials and the possibilities of further improvement of the thermoelectric properties and the figure of merit.

In the last chapter of this manuscript, complete discussion on the thermoelectric properties and their various implementations, possibility of the future improvement and a brief conclusion of all chapters will be presented.

Chapter 2

Thermal Conductivity of Porous Materials

Contents

2.1	Introduction	27
2.2	Monte Carlo Method	30
2.2.1	MC simulation for porous materials	31
2.2.1.1	Initial conditions for MC	32
2.2.1.2	Phonon drift	34
2.2.2	Mean Free Path by MC method	35
2.3	Analytical method for the MFP calculation of Porous materials	38
2.4	Thermal Conductivity Calculation	41
2.4.1	Relaxation time approximation	41
2.4.2	Thermal conductivity of bulk materials	44
2.4.3	Thermal conductivity of porous materials	45
2.5	conclusion	51

2.1 Introduction

There is common consensus that important thermal conductivity reductions should be expected in nano porous materials, as the diameter and distance between the nanopores are made smaller[61, 62, 63, 64]. However, concrete trends beyond this qualitative assessment are not yet clearly understood. In fact, we will show here that some of the dependencies previously predicted stem from oversimplifications in the model used, rather than from the real physical behavior of the system. Also, most previous efforts have concentrated on the thermal conductivity of nanoporous non-alloy matrices, such as pure Si. Previous works addressing SiGe considered nano composites comprising individual nanosized parts of pure Si and pure Ge, but they did not address the case where the matrix is a random alloy at the atomic level [65]. Here

we show that the thermal conductivity of nanoporous alloys behaves in a qualitatively different way than that of non-alloys, and this may be very advantageous for certain applications.

In this chapter, We have focused on the thermal conductivity of parallel pore arrangements, in the direction parallel to the pores. In this system heat(energy) propagates parallel to the pore length, as it was shown in the Fig.2.1. Where one side has been kept at high temperature, T_h and other side at low temperature, T_c . We have considered there is an average temperature, T all over the system between these two sides.

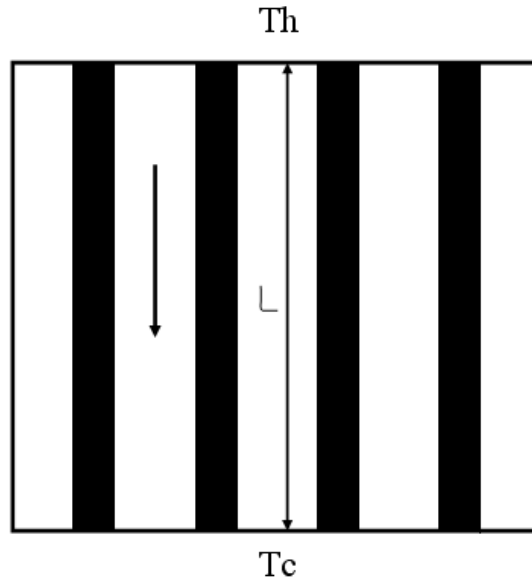


Figure 2.1: *Cylindrical pores embedded in a host matrix. Heat propagate in the direction of the pore length.*

To investigate these systems, a cylindrical geometry approximation (CGA) was proposed in Ref.[63], where the thermal conductivity was found by numerical solution of the frequency independent Boltzmann transport equation. In parallel, the CGA was also employed in Ref.[62], which provided the exact analytical solution to the Boltzmann equation for this geometry. An extension of this analytical calculation to the frequency dependent case was given in Ref.[66]. The CGA consists in replacing the porous medium by a single pore surrounded by a specularly reflecting cylindrical boundary[62, 63]. This in principle should mimic the fact that when a phonon gets away from the pore, it will approach a different pore nearby. The other boundary

condition, at the surface of the pore, can be chosen to be partly or totally diffusive.

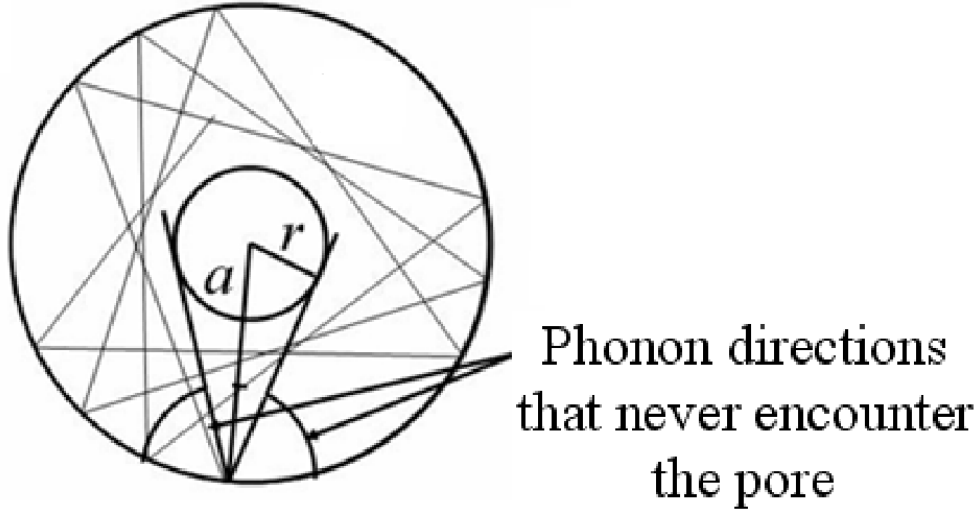


Figure 2.2: A drawback of the CGA: in the small pore radius limit some phonons never collide with the pore.

The results presented in Refs.[63] and [62] numerically agree with each other, as they should. However, the CGA employed there leads to the peculiar result that, for fixed pore volume fraction (or porosity), the thermal conductivity does not decrease indefinitely upon pore size reduction, but saturates below a certain pore size. The reason why this occurs is implicit in the analytical solution[62], which shows the presence of a continuous range of phonon directions that keep circling around the system without ever colliding with the pore (see Fig.2.2). This finite fraction of phonons gives a contribution equal to the bulk thermal conductivity weighted by the fraction of angles in which the infinite circling occurs, $F = 1 - \frac{2 \times \arcsin(\sqrt{\epsilon})}{\pi}$, where ϵ is the porosity. So the saturated thermal conductivity for infinitely small, infinitely close pores, is given by $\kappa = (1 - \epsilon) \times F \times \kappa_{bulk}$. Obviously, this result is linked to the model, and the question is whether the predicted saturation has any physical meaning. Intuitively, it is apparent that the real pore configuration will not show any continuous range of angles that do not intersect a pore: sooner or later, a line in any chosen direction should hit a pore. (This excludes high symmetry directions, if one considers ordered arrangements; but even then, the range of "unblocked" angles is not continuous, in contrast with the CGA.) Thus, the answer to whether a saturation

should occur is not obvious, and the way the thermal conductivity might depart from the CGA prediction is a priori unclear.

To answer these questions we have implemented a Monte Carlo (MC) simulation of phonon transport through a 3 dimensional array of parallel pores. We discuss Monte Carlo simulation technique in details in the section.2.2.

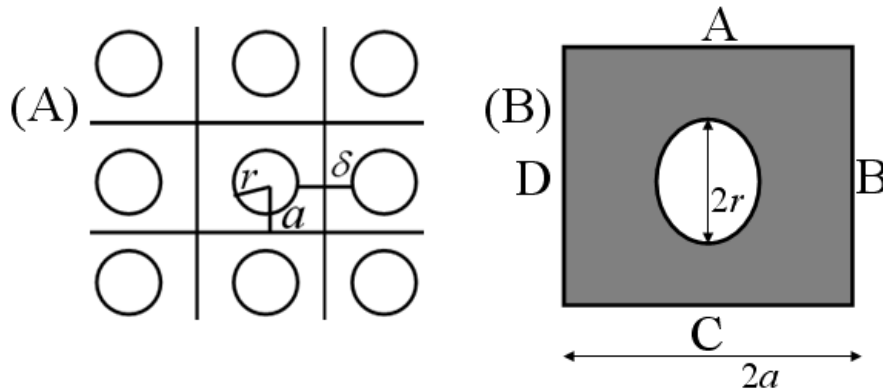


Figure 2.3: (A) Top view of the nanopore array. (B) 2 dimensional square arrangement geometry used for the Monte Carlo calculation.

2.2 Monte Carlo Method

Nowadays the Monte Carlo (MC) method is used in a lot of research areas. This method is very popular among the statisticians [67] and chemists [68, 69]. MC method also can be applied for neutron fluxes [70] and in the calculations of fluid flows [71].

Boltzmann transport equations (BTE) for phonons can be solved by Monte Carlo simulation technique in a statistical framework in an arbitrary geometry. MC simulation has been widely used to solve the radiative transfer equation and the Boltzmann equation for electrons and holes in semiconductor[37, 72, 73, 74, 75]. Recently publications have also addressed the MC simulation for the phonon transport in various complex geometries[76, 48, 77, 21, 78]. In all these modeling phonon transport had been simulated for bulk and nanostructured materials. In an arbitrary geometry, it is difficult to solve the BTE for phonons by deterministic approach such as the discrete ordinate method (DOM) because the number of independent variables are too large and the non-linear scattering events are difficult to incorporate without an overall relaxation time approximation. Individual scattering events can not be treated by the exact solutions such as which provided by molecular dynamics, is limited to very

small structures. Therefore, the alternative is to solve the BTE for phonon in an arbitrary geometry using MC simulation technique. The MC method takes microscopic constituents into account by sampling them in a relevant way, in order to produce the most accurate statistical averages possible on the basis of a limited number of operations. Its numerical accuracy only depends on the number of samples used and therefore we can independently follow each scattering mechanism (i.e., phonon-phonon, phonon-impurity, phonon-boundary scattering processes). MC simulation is very efficient for the phonon transport in complex three dimensional nanostructures, i.e., nanocomposites. MC method is also very advantageous to the implementation of periodic boundary condition and to the study of the size effect of thermal conductivity in nanocomposites. In this section, we will discuss the heat (phonon) flux calculation by MC method. Here the heat flux is generated by the atomic motion, the atom is treated as a point mass with known trajectory i.e., position and velocity.

2.2.1 MC simulation for porous materials

In the modeling of nano structured materials, it is assumed that the phonon spectrum is same as in bulk materials.

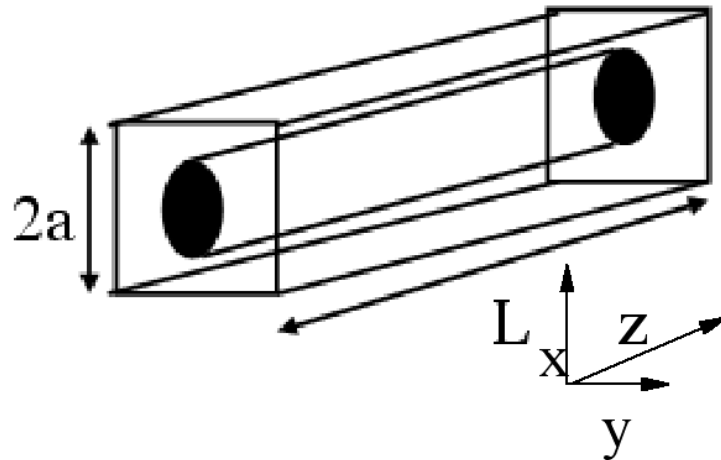


Figure 2.4: Square arrangement geometry used for the 3 dimensional Monte Carlo calculation.

We have implemented MC simulation for the cylindrical nanoporous system, described in the Fig.2.2 and Fig.2.3(a). The pores are organized in a square mesh configuration described in Fig. 2.3(a). This allows to reduce the simulation to a cell containing one pore, with periodic boundary conditions (Fig. 2.4).

First we have investigated how much the mean free paths Λ are affected due to the presence of the pores. Λ is computed as a function of the bulk mean free path Λ_0 , the pore radius r , and the porosity ϵ (as reported in Fig.2.4). The interpore distance, δ , is related to the pore radius and porosity as $\delta = 2r((0.5/\sqrt{\frac{\epsilon}{\pi}}) - 1)$. An additional variable is the length of the system, L (Fig.2.2), which needs to be taken in the long length limit.

To obtain the effective mean free path of the system, one launches a large number N of particles (phonons) from one end of the system ($z=0$), and let them evolve until they come out through either side ($z=L$ or $z=0$). We have initialized conditions before launching a phonon from $z=0$ as explained in the following:

2.2.1.1 Initial conditions for MC

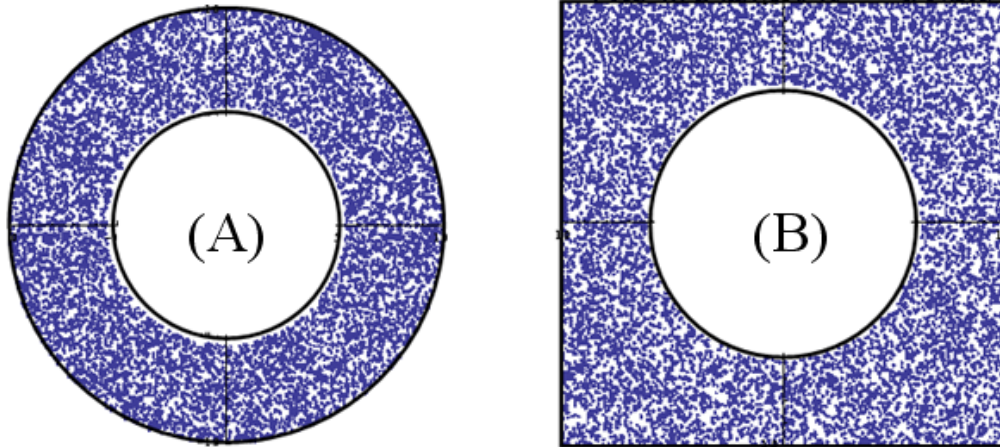


Figure 2.5: (A) Random position of points (phonons) in a 2D surface of a cylindrical wire system. The inner circle corresponds to pore surrounded by a cylinder. (B) Random position of phonons on the wall of a square mesh configuration, inside circle is the wire like pore and outside square is a periodic boundary.

1. **Phonon position.** The first step is to initialize the position of phonon on one side of the wall. we arbitrarily choose the position of each phonon on the surface (on the XY plane) of the wall of our system, Fig.2.3.(b). In the figure (Fig.2.5), we show the random positions of points (phonons) on the 2D wall ($Z = 0$) for

two geometrical systems.

2. **Velocity.** Each phonon has a random velocity in the three dimensions (3D). All the direction which can be viewed from the wall is randomly chosen for each of the particle. The directions of the total number of phonon which was launched from the one side of the wall is sampled in such a manner that the number of phonon in each random direction remain equally distributed. We consider Cartesian coordinate system for the direction of phonons, so we defined three random numbers between 1 and -1.
3. **Free Path.** Before launching the phonons from the wall, we define the free path (free flight) length of each phonon from the probabilistic equation[28],

$$p(s) = e^{-s/\Lambda_0}, \quad (2.1)$$

where Λ_0 is the mean free path of the bulk and s is the distance traveled. For randomly sampling this free flight trajectory, we consider $p(s)$ as a random number between 0 and 1.

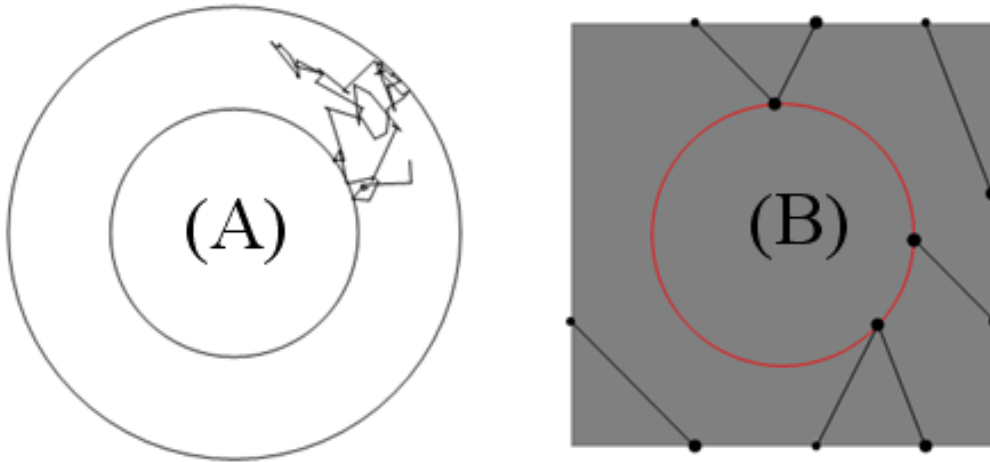


Figure 2.6: (A) Particle trajectory in 2D for the CGA model. (B) particle trajectory in 2D square geometry.

4. **Boundary condition.** We put a periodic boundary condition on the four sides (sides A, B, C, and D in Fig.2.3(b)) of the cube surrounding the cylindrical pore. When phonon (particles) cross one of these four sides, we launch another phonon

from the opposite side. For the boundaries of the cube we used Cartesian coordinate and for the cylindrical pore we used cylindrical coordinates. In cylindrical boundary approximation (CGA), we considered specular boundary conditions [62, 63] on the outer cylinder and diffusive boundary condition on the inner cylinder. In Fig.2.6, we have shown the trajectory of the particle (phonon) projected in 2D for the cylindrical geometry approximation (CGA) and square system. This figure reveals the periodic (Fig.2.6 (B)) and reflective (Fig.2.6 (A)) boundary conditions.

5. **Scattering.** We have considered two types of scattering mechanisms, phonon-phonon scattering and phonon-boundary scattering. Boundary scattering occurs when the phonon particle reaches the inner cylinder surface diffusively and the surface of the outer cylinder (for CGA model) specularly. As we consider diffusive boundary condition on the cylindrical pore surface, phonons are scattered diffusively in all directions with a new free path(s) calculated from Eqn.2.1. If it collides with the outer surface (in the CGA model), it is specularly reflected with the same velocity. In the periodic boundary approximation, if the phonon crosses any of the four surfaces of the cube surrounding the pore, we again inject a phonon from the opposite side with the same velocity and with the remaining free path. Phonon-phonon (particle-particle) collision occurs when the free path(s) is less than the length(L) of the system. After the phonon crossed the system a new phonon with new velocity and new free path(s) is generated.

2.2.1.2 Phonon drift

After initializing those above conditions, we launch particles (phonons) from the plane $z = 0$ and let them evolve along the system length (L). Then we calculate the number of phonons which fly along the opposite side of the wall at $z=L$. The fraction of particles that transmit across the whole length, $N_{through}$, reaches a diffusive type of transport given by[59]:

$$N_{through}/N \simeq (1 + L/\Lambda)^{-1}, \quad (2.2)$$

where Λ refers to the effective phonon mean free path. We perform the simulation enlarging the system's length, L , until the above behavior is attained with enough precision. We have fixed the system length L at such manner that we obtain a constant slope for $N/N_{through}$. The slope is dependent very much on the system length. When the distance is very small (i.e., $L \ll \Lambda_0$) the transport is of ballistic type. For a diffusive type drift transport, L is set larger than Λ_0 . If the system length is very

long, we have very large number of phonon-phonon collisions and the calculation starts to be very much unstable and much more time consuming. So we chose the slope on a region where the particles reach diffusive limit and L was increased until a good accuracy was obtained ($\geq 99\%$.)

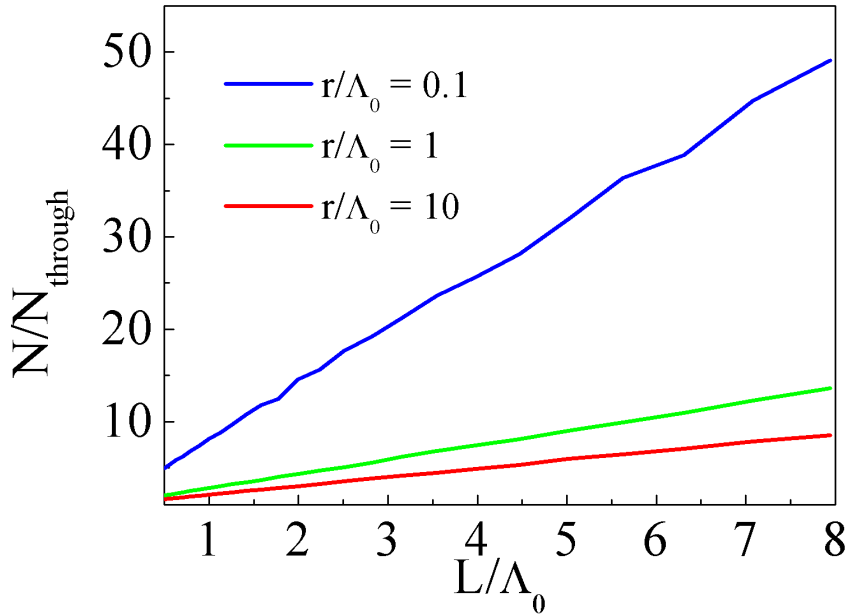


Figure 2.7: Length dependency of the transmission is described by the summation of ballistic and diffusive contribution. Ratio of launched and transmitted phonon for different length of the system at porosity, $\epsilon = 0.6$.

It can be verified that this model is equivalent to other descriptions based on time steps discretization [48, 21], and that it yields the correct solution to the diffusion equation. The simulations employed 10^6 phonons, which ensures satisfying statistical averages.

2.2.2 Mean Free Path by MC method

The mean free path of the system is evaluated from the slope of the inverse throughput fraction, using Eqn.2.2. In order to verify that this method accurately yields the mean free paths, we have first applied it to reproduce the CGA results given analytically in Ref.[62]. As shown in Fig.2.8, the numerical MC results (open symbols) are in very

good agreement with the exact analytical results (red lines). This makes us confident that our computations for the fully 3D square geometry are accurate.

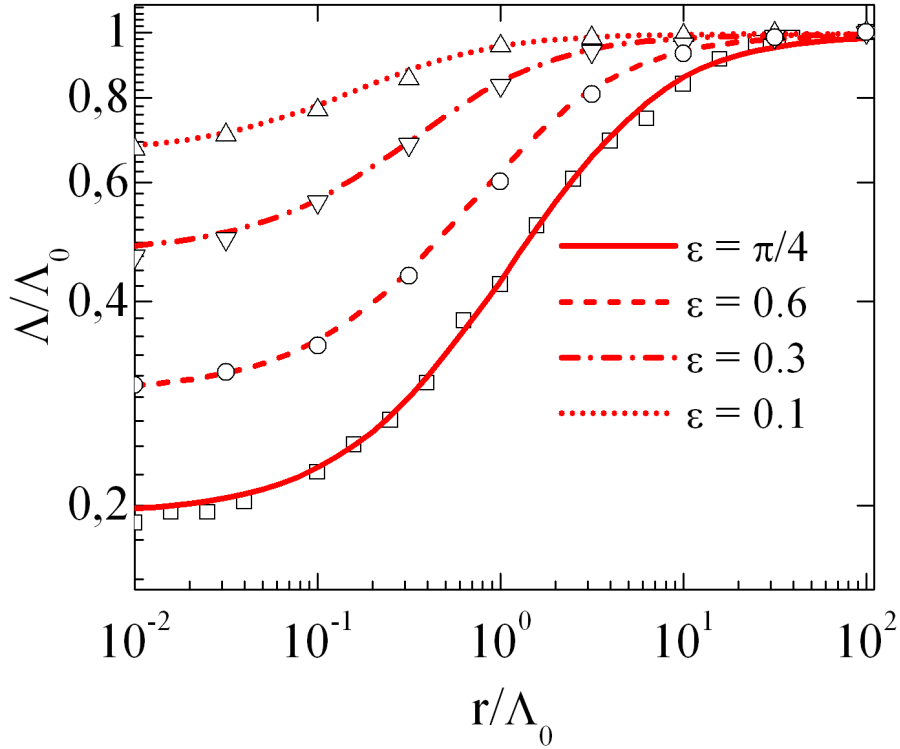


Figure 2.8: Dimensionless mean free path for porosity, $\epsilon = 0.1, 0.3, 0.6,$ and $\pi/4$, calculated by: MC CGA approximation (open symbols), analytical CGA (red lines).

Then we calculated the mean free path of the cylindrical porous wire nanocomposites considering periodic boundary condition in 3D as described previously. In Fig.2.9 the filled symbols represents the MC calculations and the solid lines corresponds to the analytical calculation which we will discuss in the next Section.

The shortening of the mean free path with pore size for the real systems is shown in Fig. 2.9. The figure shows that when the intrinsic bulk mean free path Λ_0 is larger than the pore size and interpore separation, the size effect becomes important. However, contrary to the CGA's prediction (red lines), no saturation occurs at small

pore size. This is clearly due to phonon-boundary scattering which is increased, when we decreased the pore radius for a fixed porosity, ϵ . In the previous CGA model due to the oversimplification of the boundary condition, some fraction of the phonon-boundary scattering was neglected. Therefore, by introducing a periodic boundary condition, we have overcome this problem and have obtained the accurate mean free path of the phonon for the cylindrical porous wire system. It can be also possible to predict this kind of mean free path (MFP) dependency for porous materials by an analytical solution as presented in the next section.

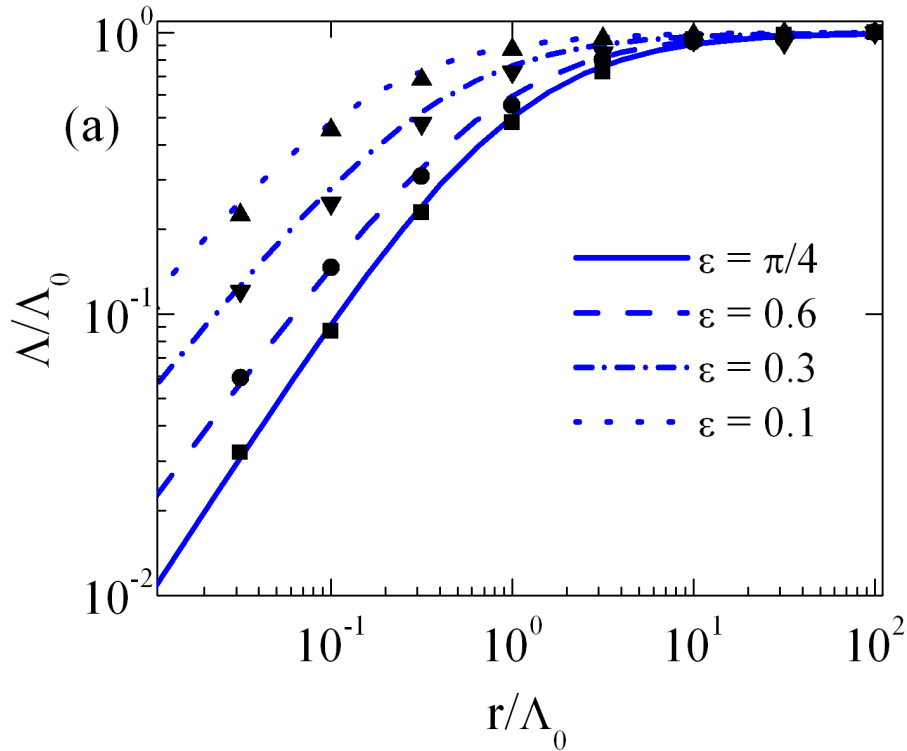


Figure 2.9: Dimensionless mean free path for porosity, $\epsilon = 0.1, 0.3, 0.6,$ and $\pi/4$, calculated by: MC fully 3D periodic boundary (closed symbols), analytical (blue lines).

2.3 Analytical method for the MFP calculation of Porous materials

By using the MC simulation technique for the porous materials, we have seen that the mean free path keeps decreasing indefinitely as the pores become smaller. It is tempting to associate the decrease with a formula of the Casimir type, in which the role of the system's size would be played by the inter-pore separation d , as $\Lambda \sim d$ [18].

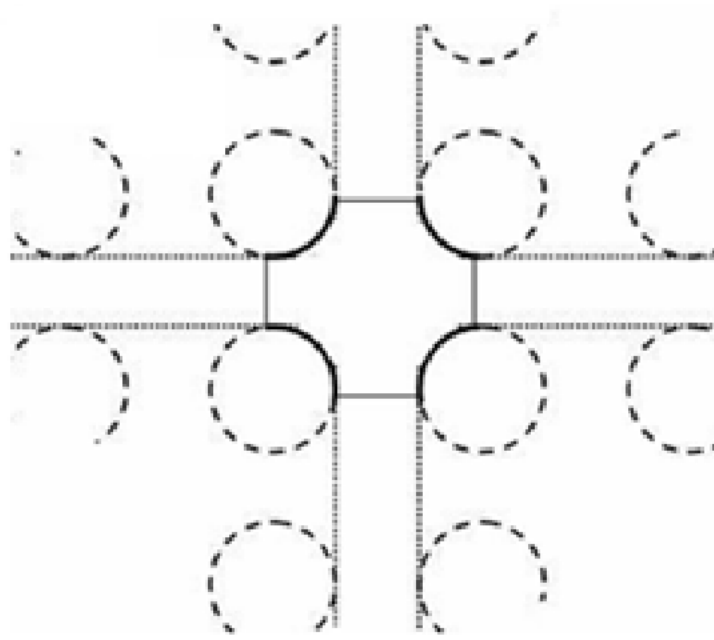


Figure 2.10: Geometry used for the analytical interpolation eqn. (2.5).

However, the log-log plot in Fig. 2.9 shows that this oversimplified form does not match the results, except when the volume fraction exceeds $\frac{\pi}{4}$. When $\epsilon > \frac{\pi}{4}$ the nanopores touch each other, so that the system becomes an array of parallel independent nanowires, which is well described by $\Lambda \sim d$ [79]. However, for $\epsilon < \frac{\pi}{4}$ the system becomes connected, and the thermal conductivity depends on d more slowly.

We can understand this behavior as follows. Within the unit mesh depicted in Fig. 2.10, we have a fraction of the boundary $C = 1/(1 + 2\delta/\pi r)$ (thick solid line)

that is covered by the pores. The remaining fraction, $1 - C$ (thin solid lines), is open and it allows the particles to traverse into a neighboring mesh.

Most of the phonons that traverse to a neighboring mesh via the opening between pores, will do so in a rather shallow angle. This means that the effective row of pores seen by those phonons looks more like two continuous parallel plates (dotted lines in Fig. 2.10). One can therefore try to interpolate the total mean free path as a simple combination of the Casimir type mean free path for a wire of radius r [18],

$$\Lambda_{casimir}(\omega) = (1/\Lambda_0(\omega) + 1/(2Br))^{-1} \quad (2.3)$$

and the mean free path for a thin film given by Lucas [80],

$$\Lambda_{Lucas}(\omega, D) = \Lambda_0(\omega) \left(1 - \frac{3\Lambda_0(\omega)}{4D} \int_0^1 2(x - x^3)(1 - e^{-D/x\Lambda_0(\omega)}) dx \right) \quad (2.4)$$

where B is a parameter associated to the shape of the wire's cross section, and D is the thickness of the equivalent film.

Therefore, a plausible form for the system described in Fig.2.10 is

$$\Lambda(\omega) \simeq C\Lambda_{casimir}(\omega) + (1 - C)\Lambda_{Lucas}(\omega, A \times r/\sqrt{\epsilon}) \quad (2.5)$$

where $A \equiv D\sqrt{\epsilon}/r$ is the only adjustable parameter, corresponding to the effective thickness of the equivalent thin film. B should not be considered adjustable; rather, it corresponds to the case of $\epsilon = \frac{\pi}{4}$, when the system becomes a nanowire array.

We have calculated parameter B in the following way. In the $\epsilon = \frac{\pi}{4}$ case for different pore radius, the pore wire touch each other and the system look like as a nanowire with the shape black cross section area described in Fig.2.11

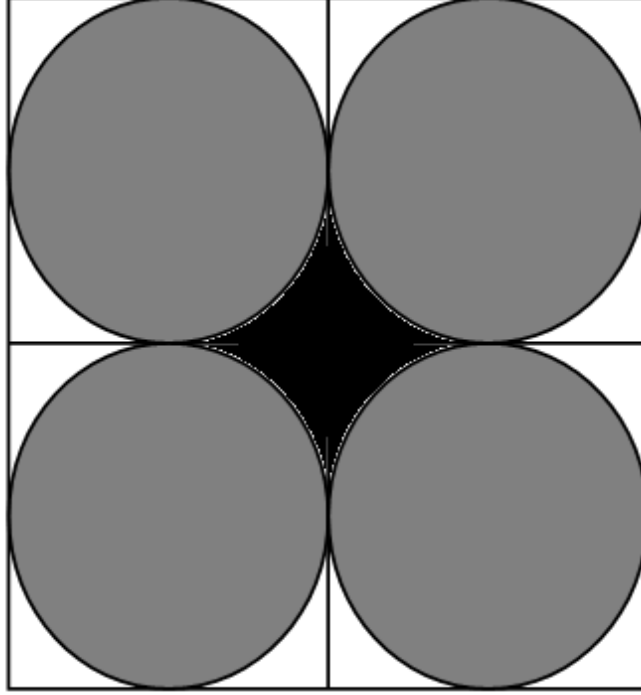


Figure 2.11: Top view of the cylindrical pore wire when porosity, $\epsilon = \frac{\pi}{4}$. In this case the system becomes nanowire with the shape as depicted by black colour.

According to Casimir formula, the boundary scattering MFP, (Λ_B) for any geometrical structures can be expressed as

$$\Lambda_B(\omega) = \int_{-1}^1 \frac{3 \langle \rho \rangle}{\sqrt{1 - \cos^2 \theta} \frac{d(\cos \theta)}{2}} = \frac{3\pi}{4} \langle \rho \rangle \quad (2.6)$$

where ρ is the distance of the lattice point from the boundary and θ is the direction of the velocity.

We can obtain $\langle \rho \rangle$ for different geometries from the following

$$\langle \rho \rangle = \int \int \rho(\varphi, x, y) \frac{d\varphi}{2\pi} \frac{dS_c}{S_c}, \quad (2.7)$$

where S_c is the cross section of the solid system. Now we can analytically solve the

Eqn.2.7 for the simple geometry such as cylindrical and square rod. The analytical solution of Λ_B for the cylindrical and square wires are $2R$ and $1.12D$ respectively, where R is the radius of the cylinder and D is the side of the square.

For the complex system as described in Fig.2.11, it is very difficult to solve the above integration. Therefore, we calculated the total area by generating a random mesh of points by using a METROPOLIS scheme. The parameter B is the ratio between the number of points inside this special shape and the total number of points all over the square of the side $2a$. From this model we obtained $B = 0.85$. The proposed formula for the porous cylinder (Eqn.2.5) works remarkably well. Fig. 2.9 shows a comparison between the MC (filled symbols) and analytical (blue lines) results for a large range of porosities and pore sizes. The best fit was obtained for $A = 1.85$. This formula is extremely practical, because it allows for a very fast computation of the effective mean free paths (mfp) of the nanoporous material, for any values of Λ_0 , r , and ϵ , with good accuracy. This is advantageous in the application of these results to compute the thermal conductivity of concrete nanoporous materials.

2.4 Thermal Conductivity Calculation

2.4.1 Relaxation time approximation

In the relaxation time approximation, the thermal conductivity can be expressed as an integral over frequencies of the form Ref.[79]

$$\kappa = \int_0^{xc} \frac{df_B}{dT} \Lambda(\omega) \mathcal{T}_0(\omega) \hbar \omega d\omega / 2\pi \quad (2.8)$$

where $\mathcal{T}_0(\omega) = \frac{1}{2} \sum_{\alpha=1}^6 \int_{BZ} \delta(\omega - \omega_{\alpha}(\vec{q})) \left| \frac{d\omega_{\alpha}(\vec{q})}{dq_x} \right| d\vec{q} / 2\pi$, $\Lambda(\omega)$ is the total mean free path, and f_B is the Bose distribution.

The thermal conductivity of the nanoporous material is therefore calculated by the equation above, using the mean free paths computed via the MC simulation, $\Lambda(\omega) = \Lambda_{MC}(\Lambda_0(\omega), \delta, r)$, where $\Lambda_0(\omega)$ is the bulk mfp of the matrix material. The phonon dispersion relations for Si and Ge were obtained via the Harrison interatomic potential[79, 59]. The phonon dispersion for SiGe was considered in the standard virtual crystal approximation, by averaging the force constants of Si and Ge. The bulk mfp's $\Lambda_b(\omega)$ for Si and Ge were computed in the way explained in Ref.[79], and they yield a good match to the bulk crystal thermal conductivity in the 50-900K temperature range. The bulk mean free path are given by calculating relaxation time

due to different scattering mechanism. The total relaxation time is given by the Mathiessen's rule. For the bulk materials the expression used for the anharmonic, and impurity scattering are,

$$\tau_a^{-1} = BT\omega^2 e^{-C/T} \quad (2.9)$$

$$\tau_i^{-1} = A\omega^4 \quad (2.10)$$

where A, B and C are numerical constant. The constant B and C are adjusted to reproduce the experimental values of bulk materials, here $B = 1.73 \times 10^{-19} s/K$ and $C = 137.3K$. Parameter $A = 1.32 \times 10^{-45}$ is analytically determined from the isotope concentration, and it should not be adjusted so we maintain the same value given by the Ref.[81].

The full dispersion relation of *Si*, *Ge* and *SiGe* virtual crystal, has been computed from Harrison's potential[82], and are shown bellow,

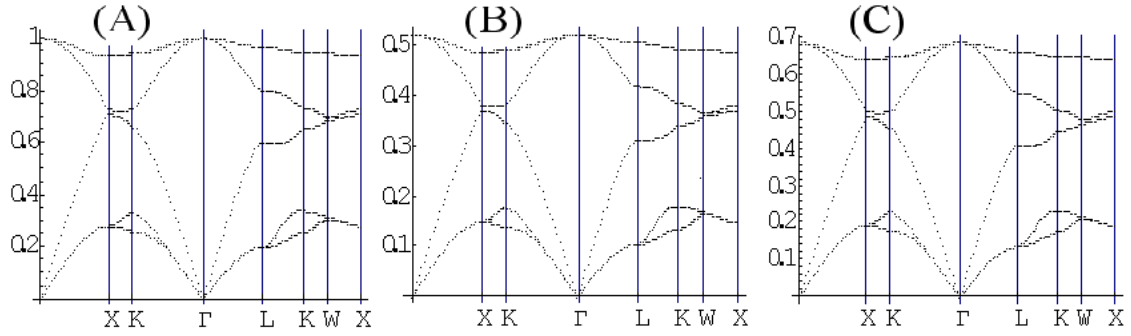
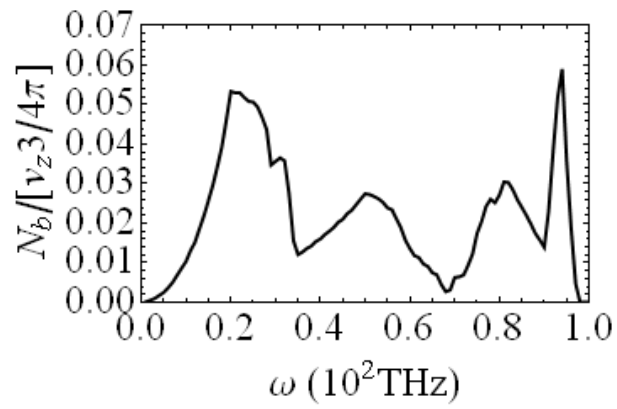


Figure 2.12: The dispersion relation of (A) *Si*, (B) *Ge*, and (C) *Si_{0.5}Ge_{0.5}*. Angular frequency is in the unit of 100 THz.

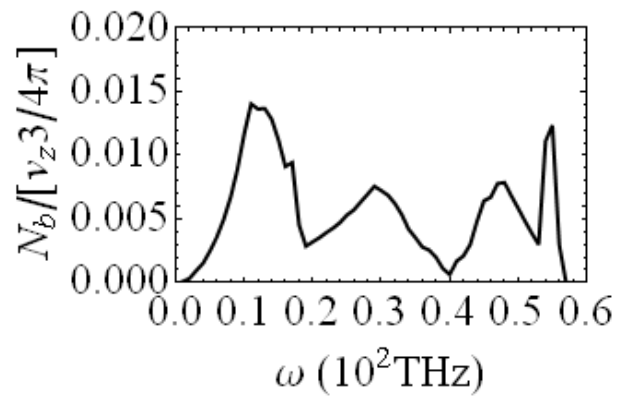
The average group velocity in the axial direction can be defined from the transmission function. Where the density of states $N_b(\omega)$, is defined as the number of phonon subbands crossing the frequency interval $[\omega, \omega + d\omega]$. Therefore, the average group velocity is,

$$\langle v_z(\omega) \rangle = \left(\sum_{\zeta} v_z(\zeta, \omega) \right) / N_b(\omega), \quad (2.11)$$

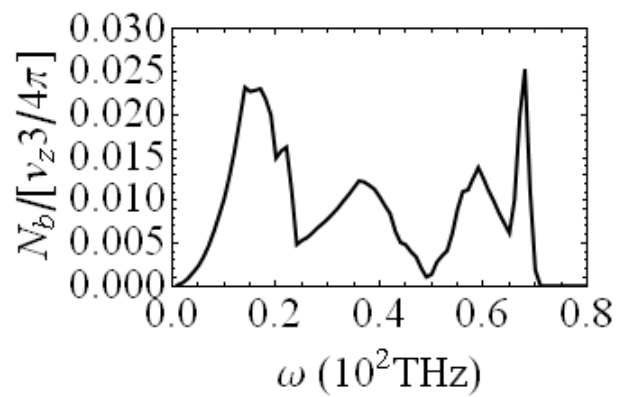
where ζ is a set of discrete quantum numbers labeling the particular subbands that are crossing the frequency ω . We have in Fig.2.13 the function $N_b(\omega)$ for Si, Ge and *Si_{0.5}Ge_{0.5}* from where we later calculate the group velocity.



(A)Si



(B)Ge



(C)SiGe

Figure 2.13: Function $N_b(\omega)$ calculated using the total dispersion relations.

2.4.2 Thermal conductivity of bulk materials

From the dispersion relation, we have obtained the group velocity for different frequency and the bulk mfp, $\Lambda_0(\omega)$, has been calculated from the different scattering mechanisms. So from Eqn.2.8, we have calculated the thermal conductivity of the pure Si and $Si_{0.5}Ge_{0.5}$ to verify the model. In the bellowing figure, the bulk thermal conductivity of Si is reported and agrees well with the experimental results.

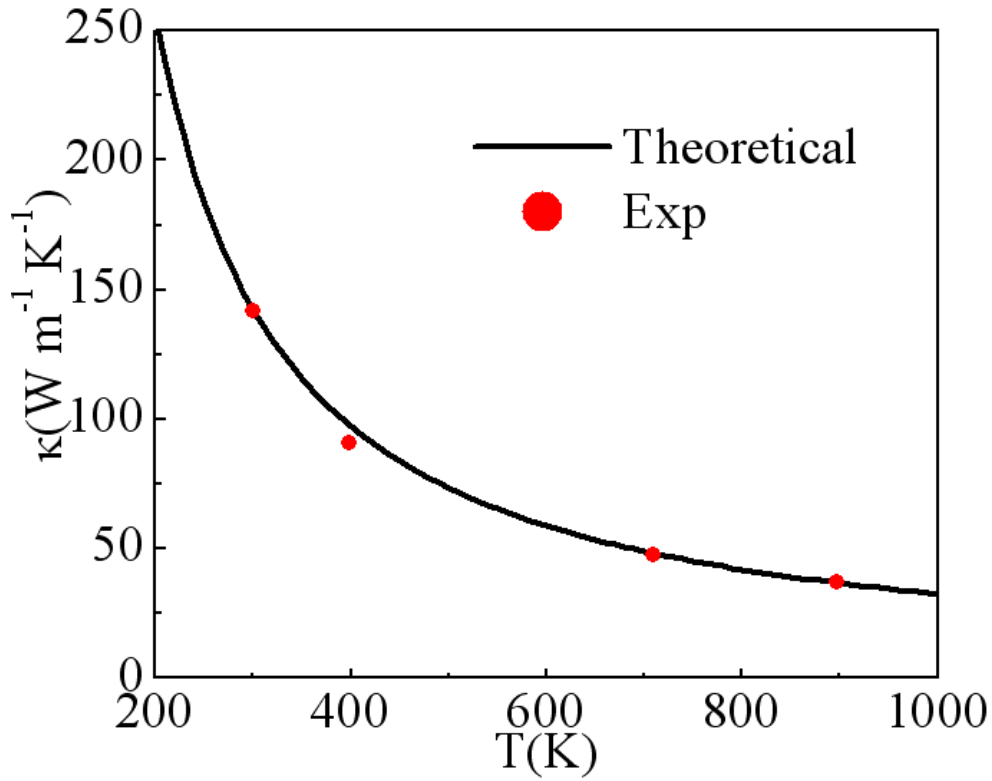


Figure 2.14: Bulk thermal conductivity of Si. Experimental results are form Ref.[83]

The bulk mfp for the alloy includes the additional *alloy scattering term* [60, 84]. The alloy scattering relaxation term can be expressed as

$$\tau_{al}^{-1} = x(1-x)\alpha\omega^4 \quad (2.12)$$

where x is the volume fraction of Ge in the $SiGe$ alloy, $\alpha = ((M_{Ge}-M_{Si})/M)^2\delta^3/(4\pi v_{sige}^3)$ and δ^3 is the volume around one atom in the lattice, M and v_{sige} are the mass

and mean group velocity of Si_xGe_{1-x} alloy respectively. Alloy disorder scattering becomes zero in the case of pure Si and Ge. Also the parameter B in Eqn.2.10 for the alloy is calculated from the weighted average of Si and Ge in the alloy, as $B = xB_{Si} + (1 - x)B_{Ge}$ and similarly for the derivation of C .

We verified that the experimental bulk alloy thermal conductivity[84] is well explained up to temperatures of 900K.

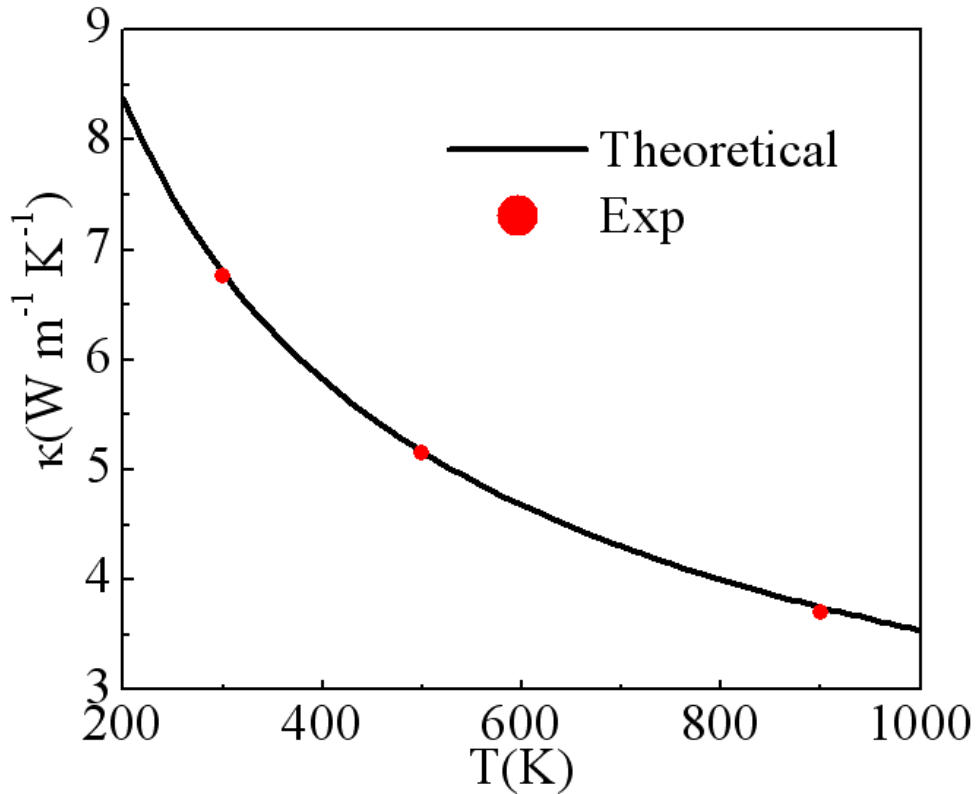


Figure 2.15: Bulk thermal conductivity of $Si_{0.5}Ge_{0.5}$. Experimental results are from Ref.[84]

2.4.3 Thermal conductivity of porous materials

Using the interpolation expression, Eqn. 2.5, combined with the knowledge of the bulk mfp, $\Lambda_0(\omega)$, allows to efficiently compute κ for the porous materials because we obtained $\Lambda(\omega)/\Lambda_0(\omega)$, where $\Lambda(\omega)$ is the mfp of the porous bulk materials from the MC simulation and also from the analytical formula.

The computed room temperature thermal conductivities of nanoporous Si, Ge, and

$\text{Si}_{0.5}\text{Ge}_{0.5}$ are shown in Fig. 2.16 as a function of pore radius, for various porosities. For comparison, results using the CGA mean free paths are also plotted for the Si case (filled symbols). The differences become very large as the pore radius becomes small enough to visibly affect the mean free path. This graph shows that the CGA yields a quite inaccurate representation of the phonon mfp and κ of the nanoporous system.

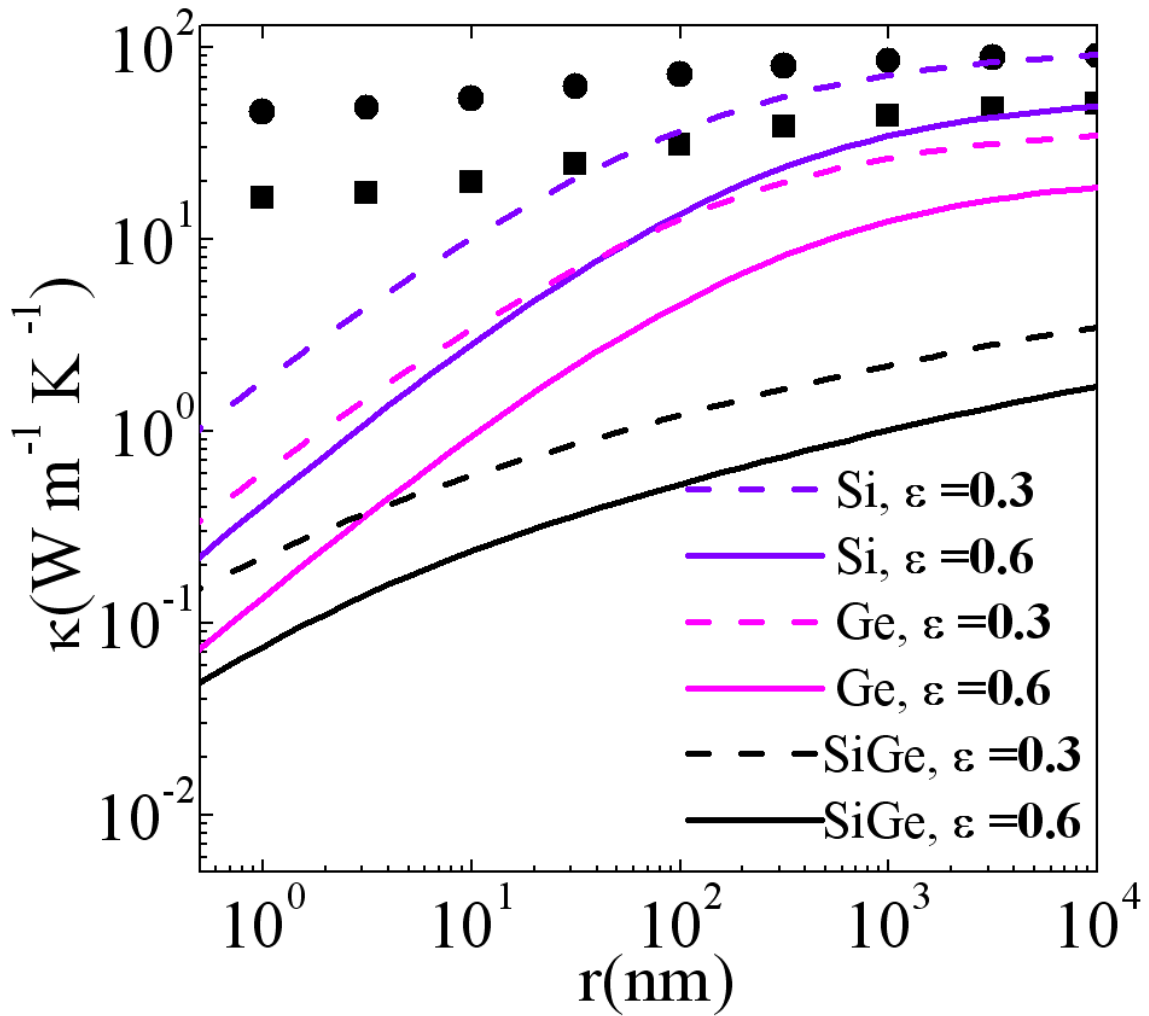


Figure 2.16: Conductivity of Si, Ge and $\text{Si}_{0.5}\text{Ge}_{0.5}$ at 30% and 60% porosity. The symbols correspond to the CGA result for Si with $\epsilon = 0.3$ (circles) and $\epsilon = 0.6$ (squares).

In addition to the full dispersion approach just described, we also tried the non-dispersive model introduced at the end of Ref.[59] (see Eq.(15) in this reference, and also Refs.[60, 79]), obtaining results very close to the ones yielded by the full dispersions model.

An even more striking finding is the noticeably different behavior of the alloy and non-alloy material thermal conductivities as a function of pore size. This is clear on the plot of the porous material conductivity normalized by the bulk material conductivity, in Fig. 2.17. The alloy material is considerably affected by the presence of a 10% porosity already at pore sizes of 1000 nm, whereas the pure Si and Ge cases are barely affected at this pore size. Only below 100 nm pore size do the 10% porosity pure Si and Ge matrices start displaying a size effect.

These pore sizes become about 5 times bigger for porosities close to the nanowire limit ($\epsilon = \pi/4$.) The room temperature thermal conductivity of bulk $\text{Si}_{0.5}\text{Ge}_{0.5}$ is just one order of magnitude smaller than those of Si or Ge, but this difference becomes 2 orders of magnitude when comparing nanoporous materials with $r \sim 200$ nm at 10% porosity, or with $r \sim 1000$ nm at 60% porosity. Below this diameter, the decrease becomes faster in the non-alloys. Nonetheless, the absolute thermal conductivity of SiGe always stays smaller than that of Si or Ge for the same porosity and size, as one would expect.

The reason for the pore effect being noticeable in the alloy at considerably larger pore diameters than in the non-alloy case, is related to the very sharp dependence of the alloy scattering mean free path. Alloys have a reduced thermal conductivity well below that of their individual components, because atomic scale disorder can scatter short wavelength phonons very efficiently. Longer wavelength phonons, however, can have mean free paths many orders of magnitude larger than the short wavelength ones. For non-alloys, the contrast between long and short wavelength mean free paths is not so marked, and a considerable amount of heat is carried by the short wavelengths. Introducing nanopores affect the long wavelengths more strongly than the short ones. This is because the former have longer mean free paths than the latter, and according to Fig. 2.9, the effect of the pores becomes noticeable when their separation starts to be comparable to the bulk mean free path. Since heat in the alloys is carried by a very small range of phonon frequencies, with very long mean free paths, rather large pores are already able to block a large fraction of that heat. For non-alloys, heat is carried in a larger frequency range, so even if the pores can block the long mfp phonons, there is a non-negligible amount of shorter mfp phonons which still requires smaller pores in order to be affected. (A similar behavior has been identified in the case of nanodots embedded into a matrix [60].)

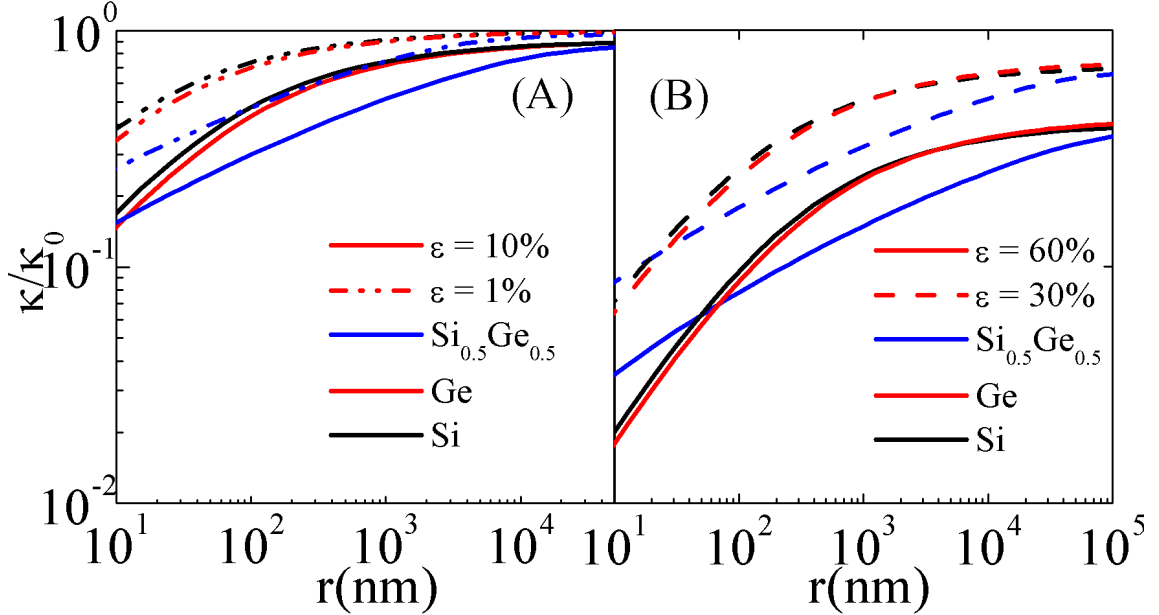


Figure 2.17: (A) Thermal conductivity of Si, Ge and $\text{Si}_{0.5}\text{Ge}_{0.5}$ at 1% and 10% porosity, normalized by their bulk values. (B) Thermal conductivity of Si and $\text{Si}_{0.5}\text{Ge}_{0.5}$ at 30% and 60% porosity, normalized by their bulk values.

In order to better assess the size effects, results can be compared with the macropore analytical limit, $\kappa_{macro} = (1 - \epsilon)\kappa_0$. Fig. 2.17(B), shows κ/κ_0 for a small porosity of 1%. For large pores the macroscopic limit $1 - \epsilon$ is retrieved. Size effects are more appreciable for SiGe than for Si, consistently with our previous discussion.

This is illustrated in Fig. 2.18. This figure shows, for each value of the mean free path Λ , the contribution to the bulk thermal conductivity of all phonons having mean free paths shorter than Λ .

For SiGe most of the heat is carried by phonons with mean free paths longer than $10 \mu\text{m}$. In contrast, in Si, a significant fraction of the heat is carried by phonons with shorter intrinsic mean free paths, which are less affected by the introduction of the pores.

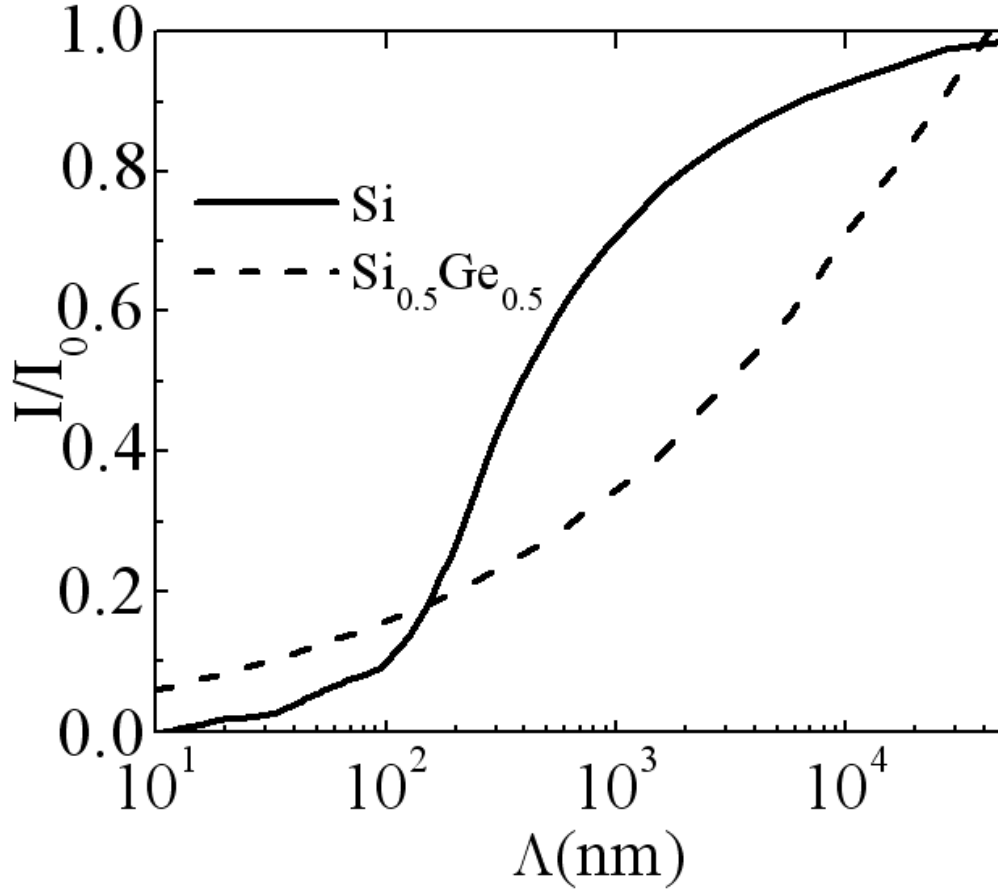


Figure 2.18: Relative contribution $I(\Lambda)$ to the thermal conductivity associated to phonons with mfp's shorter than Λ , plotted as a function of Λ , for bulk Si and $\text{Si}_{0.5}\text{Ge}_{0.5}$ at room temperature. ($I \rightarrow 1$ in the limit $\Lambda \rightarrow \infty$.)

Finally, it is interesting to look at the temperature behavior of the thermal conductivity of these systems. It is experimentally known that phonon scattering with pores or cavities can mask interphonon scattering, thus rendering the effective thermal conductivity nearly independent of temperature[85, 86]. Our calculation also yields this effect, as shown in Fig. 2.19. As expected, the effect is more pronounced for smaller pore sizes. SiGe is more strongly affected than Si at comparable pore sizes, for the reasons explained in the previous paragraph.

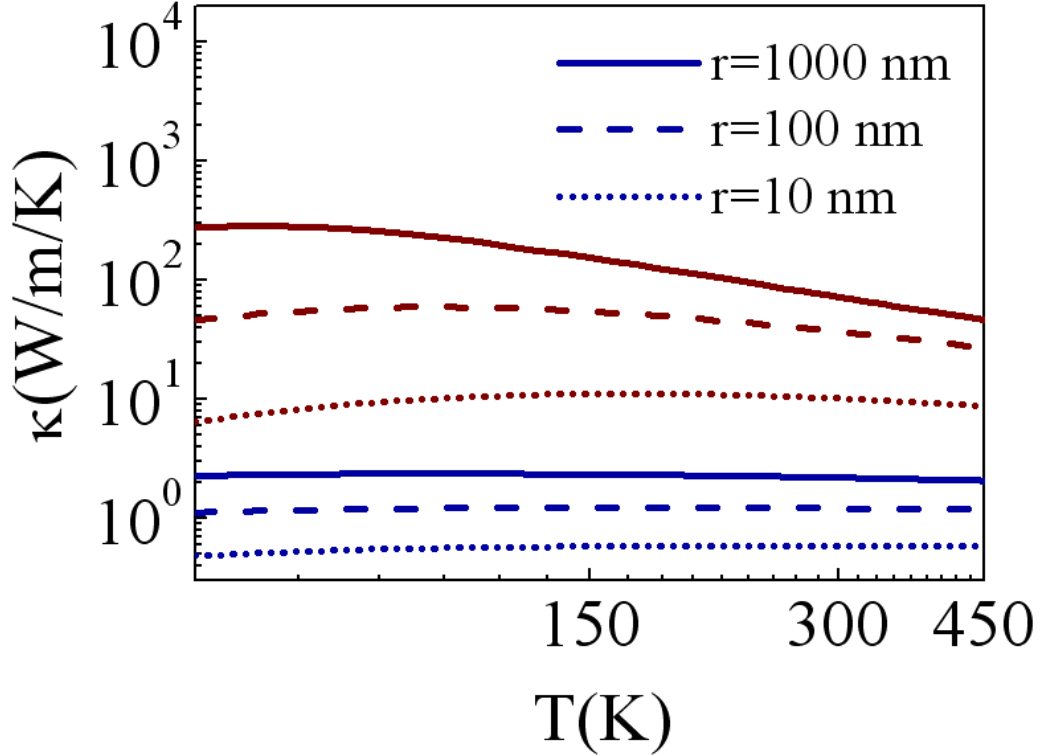


Figure 2.19: Temperature dependence of thermal conductivity for different pore sizes, for Si and Si_{0.5}Ge_{0.5} at 30% porosity.

The remarkable differences just described between the thermal conductivities of alloy and non-alloy nanoporous materials imply that nanoporous alloys may be very advantageous for certain applications. For example, nanoporous materials have been proposed as potentially interesting thermoelectrics [66, 87]. Difficulty to produce nanosized pores may however be an obstacle for their synthesis. Furthermore, the pore surfaces might in some cases act as charge traps and considerably decrease electron mobility [88]. Using a porous alloy instead would allow to take advantage of the thermal conductivity reduction at much larger pore sizes. Thus, they would be easier to synthesize, and additionally their surface to volume ratio would be smaller than in the non-alloy case, minimizing the problem of electron scattering by surface charges.

2.5 conclusion

1. By Monte Carlo simulation we have accurately evaluated the phonon mfp's of parallel nanoporous materials.
2. We have found that a previously used cylindrical geometry approximation yields an inadequate description of the actual mean free paths in the real system.
3. The behavior of the mfp with pore size and porosity can be understood as a combination of a wire and film behavior, and a suitable interpolation formula has been provided that accounts well for all the MC results.
4. For small pores, calculation of the thermal conductivity using the correct mfp's yields results considerably lower than those predicted in earlier publications. We have then investigated the thermal conductivity of porous Si, porous Ge, and porous SiGe alloy, obtaining an important qualitative difference between the alloy and the non-alloys.
5. The thermal conductivity of the alloy is strongly affected by pores even at large ($1\ \mu\text{m}$) diameters. In contrast, the thermal conductivity of Si or Ge is only affected when the pores are considerably smaller ($< 100\ \text{nm}$), due to the rather different competing phonon scattering mechanisms acting in alloys and non-alloys. These remarkable differences are highly relevant for applications targeting thermal conductivity reduction, such as nanostructured thermoelectric materials, where we have shown that the use of an alloy is potentially advantageous.

Chapter 3

Thermal Conductance of Nanowires

Contents

3.1 Introduction	53
3.2 Conductance of nano wire	55
3.2.1 Landauer Equation and Quantum of thermal conductance	55
3.2.2 Transmission function	56
3.2.3 Mean free path	58
3.2.4 Surface roughness	59
3.3 Transmissivity calculation by MC Simulation	61
3.4 Results	64
3.5 Conclusion	68

3.1 Introduction

A current major challenge in thermal physics is the control and manipulation of phonons, the quantized modes of vibration of the lattice, and hence the heat transfer at small length scale [30, 29]. Such control via nanoengineering, also termed nanophononics[89], may one day enable the development of thermal logic components analogous to those existing in electronics like thermal rectifiers [90, 91, 92], diodes or logic gates and memories [93]. The modification of phonon transport in nanoscale systems as compared to the bulk has been at the core of rare but significant experiments at low temperature [94, 95, 96, 97, 98, 50]. The effects of surface roughness and contact resistance on phonon transport through nanowires and nanotubes has been studied in numerous publications[59, 99, 100, 101, 102, 103]. However, only one work has investigated the effects induced by changes in the conductor's geometrical shape, in the particular case of a carbon nanotube (CNT)[104]. That experiment showed that strong bending of the CNT does not affect phonon transport significantly. In

contrast, in this chapter we show that changes in geometrical shape can strongly affect heat flow through Si nanowires. By engineering serpentine shaped nanowires, the phonon transmission is reduced by nearly 40% at temperatures below 5K. Experiments on this special kind of structure have been successfully carried out by our collaborator [105]. We will show that this amount of reduction is strikingly large and cannot be understood by a simple Casimir type model. We have performed a more detailed transmission function analysis, which unveils the fact that transverse modes are strongly filtered out at the interface between the nanowire and the thermometer. This model yields a very satisfactory agreement with experimental measurements.

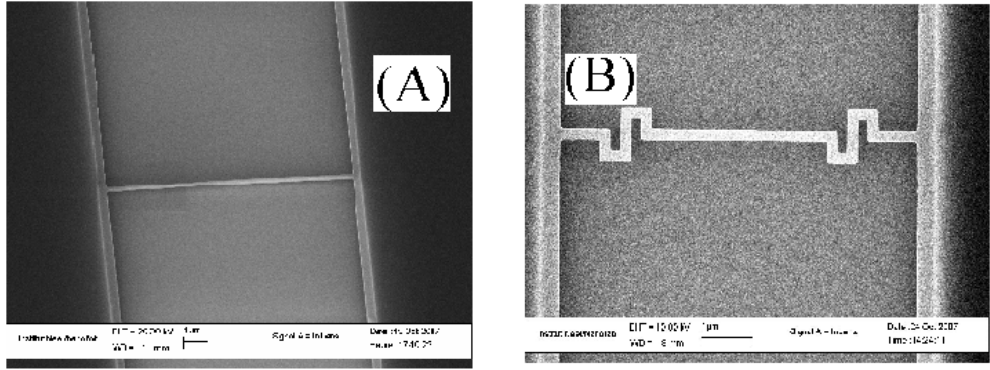


Figure 3.1: SEM pictures of the different studied systems. These nanowires are fabricated and experimentally characterized by J-S Heron *et. al.*, in Institute Néel. Ref.[105] **A**, The straight nanowire $10\mu\text{m}$ long with a section of $200\text{nm}\times 100\text{nm}$; it will be used as the reference sample. **B**, Top view of the serpentine nanowire composed of two double bend connection to the heat bath, the phonon trap.

The total length of each nanowire structure has been purposely set to $10\mu\text{m}$ in order to easily compare the thermal measurement of the two systems. The section of the nanowires (100 nm by 200 nm) as well as the double bend structure (400 nm long) are of the order of the dominant phonon wave length ($\lambda_{dom} \cong hv_s/2.82k_B T$, where v_s is the sound velocity [18]) in silicon at 1K: $\lambda_{dom} \cong 100\text{ nm}$. We have considered the exact geometry and the dimension for the numerical calculation.

The hottest point is located in the middle of the systems, and heat flows from the center of the nanowire to the heat bath on both sides. Therefore, the nanowire length, L , must be taken as the distance between the center of the structure and the heat

bath, i.e. $5\mu\text{m}$. For the measurement of the thermal conductance, a typical power of a few tens of femtowatts is dissipated in the niobium nitride (NbN) transducer deposited on top of the nanowire creating a temperature gradient smaller than 1mK [52].

3.2 Conductance of nano wire

The values of the experimentally measured thermal conductance are around a few universal quanta of thermal conductance $\sigma_0 = \pi^2 k_B^2 T / 3h \sim 10^{-12} \text{TW/K}^2$. The universal quantum of the thermal conductance for the 1-D wire is theoretically calculated in the Ref.[58] starting from the Landauer formula for heat flux[106, 107].

3.2.1 Landauer Equation and Quantum of thermal conductance

From the Landauer formula, the energy flux carried by a wire connecting two reservoirs labeled R and L can be written as,

$$\dot{Q} = \sum_{\alpha} \int_0^{\infty} \frac{dk}{2\pi} \hbar \omega_{\alpha}(k) v_{\alpha}(k) (\eta_R - \eta_L) \mathcal{T}_{\alpha}(k) \quad (3.1)$$

where $\omega_{\alpha}(k)$ and $v_{\alpha}(k)$ are the frequency and velocity of mode α of the quantum wire with wave vector k , $\mathcal{T}_{\alpha}(k)$ is the phonon transmission probability through the wire, and $\eta_i(\omega) = 1/(e^{\hbar\omega/k_B T_i} - 1)$ represents the thermal distribution of phonons coming from the left and right, assumed to be a Planck distribution at temperature T_i .

Now as the phonon velocity $v_{\alpha}(k) = \partial\omega_{\alpha}/\partial k$ is canceled by 1-D density of states $g(\omega_{\alpha}) = \partial k/\partial\omega_{\alpha}$, Eqn.3.1 transforms to,

$$\dot{Q} = \frac{1}{2\pi} \sum_{\alpha} \int_0^{\infty} d\omega \hbar \omega_{\alpha} (\eta_R(\omega) - \eta_L(\omega)) \mathcal{T}_{\alpha}(\omega) \quad (3.2)$$

The reservoir to reservoir thermal conductance of the wire is,

$$\sigma = \dot{Q}/\Delta T \quad (3.3)$$

where $\Delta T = T_R - T_L$ is the temperature difference between the reservoirs.

Now from Eqn.3.2 and Eqn.3.3 the harmonic phonon thermal conductance can be written as[59],

$$\sigma(T) = N_\alpha \int_0^\infty \mathcal{T}(\omega) \hbar\omega \frac{df}{dT} \frac{d\omega}{2\pi}, \quad (3.4)$$

Where $\frac{df}{dT} = \frac{\eta_R - \eta_L}{\Delta T} = \frac{\hbar\omega}{k_B T^2} \frac{e^{\hbar\omega/k_B T}}{(e^{\hbar\omega/k_B T} - 1)^2}$ and N_α is the number of massless modes. In a suspended wire, there are 4 acoustic modes, as described in figure.3.2

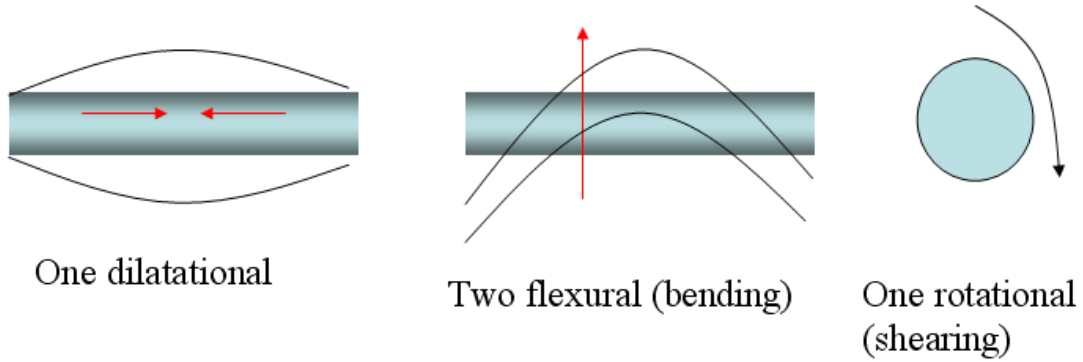


Figure 3.2: Different modes in the wire.

For the suspended nanowire, when we assume perfectly adiabatic contact between the thermal reservoir and the ballistic quantum wire, we can consider $\mathcal{T}(\omega) = 1$ and the solution of the Eqn.3.4 becomes $\sigma = N_\alpha \frac{k_B^2 \pi^2 T}{3\hbar}$. Therefore, the theoretical low temperature thermal conductance of a nanowire with no contact resistance is $4\sigma_0$ [58]. The values of the thermal conductance are thus presented in unit of $4\sigma_0$ (Fig.3.8), and correspond to the $5\mu m$ long nanowires (half of the total length of the structure).

3.2.2 Transmission function

In the real geometry, where the thermal conductance is not independent of the length, L of the systems, we can describe the thermal conduction by the concept of transmission channels, as it was shown by Landauer for the electron transport in the small microelectronic system[108]. At frequencies above the quantized regime ($\omega > 2\pi c/\sqrt{A} \sim 0.2THz$, in our wires, where A is the wire's cross section), phonon dispersion are practically bulk like, the transmission function simply can be written

as [59]:

$$\mathcal{T} = \frac{A}{4\pi^2} \sum_{\alpha=1}^3 \int_0^{\omega/c_\alpha} \tilde{t}^\alpha(\vec{k}_\perp, \omega) d^2k_\perp \equiv \frac{A}{4\pi} \sum_{\alpha=1}^3 t^\alpha(\omega) \frac{1}{c_\alpha^2} \omega^2, \quad (3.5)$$

where $t^\alpha(\omega) \equiv \int_0^{\omega/c_\alpha} \tilde{t}^\alpha(\vec{k}_\perp, \omega) d^2k_\perp / \int_0^{\omega/c_\alpha} d^2k_\perp$ is the average phonon transmission probability across the structure at that frequency.

The transmission probabilities $t^\alpha(\omega)$ are the most important magnitudes in the expression Eqn.3.5, since they account for all the geometry related effects on the thermal conductance. They can be adequately modeled as the sum of the inverse transmission probabilities associated with the different scattering obstacle along the wire[109].

There is contribution from the nanowire's boundary, proportional to the ratio between the boundary mean free path, $\lambda(\omega)$ and the total nanowire length L . If the wire is sufficiently long so that all phonons are transported diffusively, t is

$$t(\omega) = \frac{4}{3} \frac{\lambda(\omega)}{L}, \quad (3.6)$$

where L is the wire length and $\lambda(\omega)$ is the average phonon relaxation length. This equation yields the Callaway formula for bulk materials [50] when inserted into Eqs. 3.4 and 3.5.

For shorter L , a good interpolation formula between the ballistic and diffusive regimes is[110]

$$t(\omega) \simeq \frac{1}{1 + \frac{3L}{4\lambda(\omega)}}, \quad (3.7)$$

which correctly yields the diffusive limit when $L \rightarrow \infty$ and ballistic limit when $L \rightarrow 0$.

At frequencies lower than $\omega_l \sim 2\pi c/\sqrt{A}$, only the four lowest nanowire acoustic modes exist, and Eq. 3.5 is no longer valid. Instead we have $\mathcal{T} = \sum_{i=1}^4 t_i(\omega)$, where $0 < t_i < 1$ is the transmission probability of each of the four modes. If the contact junction is abrupt, the transmission is dominated by the contact. Chang and Geller have provided analytical expressions for the transmission probabilities, $0 \leq t(\omega) \leq 1$, from the contact into the four different branches. The largest contribution is that of the longitudinal acoustic branch, which at low frequency is [111]:

$$t_{\text{contact} \leftrightarrow \text{LA}} \simeq 0.923 \frac{A \omega^2}{\pi c_l^2}. \quad (3.8)$$

Except for the just slightly different prefactor, this expression is identical to the ballistic transmission function expression valid at higher frequencies, Eq. 3.5. The

other branches depend more rapidly on frequency so their contribution to the conductance is smaller. Expression 3.8 is only valid at low frequencies, and it is not applicable for frequencies larger than $c_t \sqrt{\pi/0.923}/\sqrt{A}$ (or else t would become larger than 1.) However, for fitting purposes, we will assume this to be the form of the transmission function in the quantized regime, for $\omega < \omega_l$, including an adjustable parameter of order 1, f_{adj} , as

$$\mathcal{T}_{low} \simeq f_{adj} 0.923 \frac{A \omega^2}{\pi c_t^2}. \quad (3.9)$$

The ultimate validity of this approximation is only confirmed by its ability to match the experimental data.

There are also significant contribution in the phonon transmission from the geometrical structure of the nanowires. By creating special kinds of geometrical structures we can provide obstacles to the phonon transmission along the wire. In the case of the nanowire geometry in Fig.3.1.(B), the serpentine in the wire provides this kind of obstacle to phonon transport. considering the contribution, t_{obs}^{-1} from this kind of localized obstacle, the final transmission equation can be written as,

$$t(\omega) \simeq \frac{1}{t_{obs}^{-1} + \frac{3L}{4\lambda(\omega)}}. \quad (3.10)$$

3.2.3 Mean free path

In Eqn.3.10, we have seen that the transmission probability calculation of the wire depends on the mean free path, $\lambda(\omega)$ of the phonon on that geometry. Therefore, accurately defining $\lambda(\omega)$ becomes important for the proper calculation of the thermal conductance. For the low temperature Casimir proposed a model of thermal transport[112] due to surface scattering of the wire. According to the Casimir model, thermal transport is described in the following way: the phonons are diffracted in all directions when they reach the surface of the wire, scattering occurs only at the boundaries of the nanowire, which are considered as perfect black bodies. Thus the mean free path is limited only by the cross section of the wire for the perfectly rough surface. For the different geometrical nanowire the mean free path, λ_{Cas} can be calculated from Eqn.2.7 given in Chapter.2 . The circular nanowire has mean free path $\lambda_{Cas} = 2R$ and rectangular nanowire have $\lambda_{Cas} = 1.12(L_A \times L_B)^{1/2}$, where $L_A \times L_B$ is the cross section of the wire. Later this Casimir model was modified by Ziman [113] for the case when the surface is not totally rough. According to this model a



Figure 3.3: (A). Scattering at the totally rough surface ($p = 0$). (B). Scattering at perfectly smooth surface ($p = 1$).

phenomenological parameter $p(l, T)$ can be considered which describes the probability of the phonon of wave length, l at the temperature T to be specularly reflected. The parameter $p(l, T)$ is defined between the $p = 0$, totally rough surface, an incident phonon on the surface will be scattered in all directions (Fig.3.3(A), this is the limit of the Casimir model for the perfectly rough surface) and $p = 1$, perfectly smooth surface, every single phonon will be specularly reflected when hitting the surface (Fig.3.3 (B)).

We can express the mean free path now as[18]

$$\lambda_{ph} = \lambda(l, T) \simeq \frac{p(l, T) + 1}{p(l, T) - 1} \lambda_{Cas}. \quad (3.11)$$

This definition of the scattering is the same as in the flow of the vary rarefied gas in the tube known as Kundsen gas [114, 115].

The value of p is not constant, it depends on the wave length of the phonon and the temperature. As the temperature decreases dominant phonon wave length increases, and the value of p starts to increase. The same surface can be rough for the small wave length phonons and very smooth for the high wave length phonons. As we see in Fig.3.4.

3.2.4 Surface roughness

Now parameter $p(l, T)$ can be expressed as a function of the root mean square deviation of the height of the surface from the reference plan, η . It was named as *asperity* parameter by Ziman.

When a plane wave incidents normally on the surface, a reflected wave will be propagated or retarded with a phase, ϕ depending on this *asperity* parameter as,

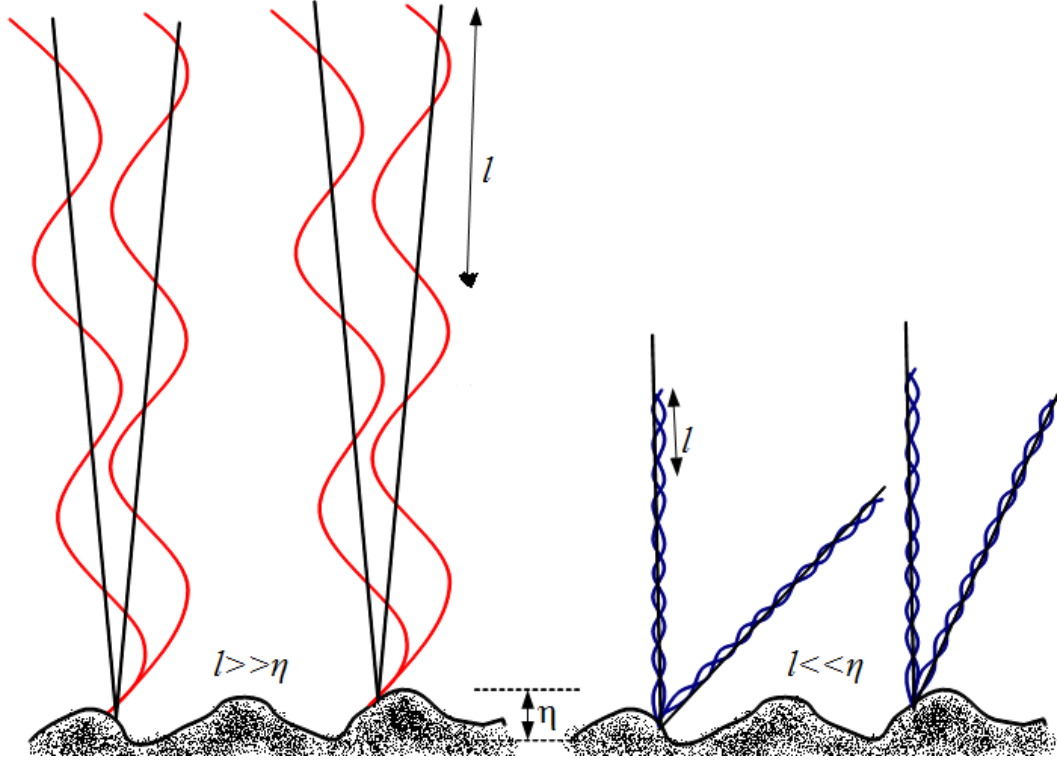


Figure 3.4: Same surface appears smooth for long wave length and rough for the small wave length.

$$\phi = \frac{4\pi\eta}{l} \quad (3.12)$$

Now the probability of specular or diffusive scattering will be

$$p'(l, T) = e^{-\pi\phi^2} = e^{-\frac{16\pi^3\eta^2}{l^2}}. \quad (3.13)$$

Eqn.3.13 very well defines the relative proportion of the specular or diffuse reflection. When $l \ll \eta$, p' is very small, the wave after the reflection get or loss phase randomly and scattered very widely. For larger values of l , much exceeding the *asperity* height, the change in phase will be negligible and the reflection become totally specular at p' closed to unity.

The *asperity* is not fixed for the surface, there may be some space where it is perfectly smooth again with some area with scratches and some other irregularities.

Therefore, there is a probability for the η itself, $P(\eta)$. Assuming an exponential distribution function for $P(\eta)$, we can express it as [98],

$$P(\eta) = \frac{1}{\eta_0} e^{-\eta/\eta_0}, \quad (3.14)$$

where η_0 can be seen as the mean value of the roughness.

Therefore, the average value of p' becomes,

$$\overline{p'(l, T)} = p(l, T) = \int_0^\infty P(\eta) e^{-\pi \frac{16\pi^2 \eta^2}{l^2}} d\eta \cong \int_0^{l_{dom}/4\pi} P(\eta) d\eta. \quad (3.15)$$

From Eqn.3.15, the polish of the surface can be understood as a function of the wave length. The fraction of phonon l which will be specularly reflected, is a measure of the fraction of the area of the surface where the asperities are less than $l/4\pi$ in height.

3.3 Transmissivity calculation by MC Simulation

We have done a MC simulation to understand the phonon transport in the serpentine nanowire (see Fig. 3.1) and straight nanowires. For the MC method, we consider the phonon as a particle with very large mean free path. Then we launch phonon (particle) from the one side of the wire and calculate the number arrives on the other side. To make similar as the 3ω experimental method we consider half length of the wire ($5\mu m$) as a system length. Because in 3ω method the heater was placed on the middle of the wire and the two thermometer at the end side. Therefore, the heat gradient is created only on the ($5\mu m$) length with one kink (Fig.3.5(A)).

We choose the random direction on two dimension (2D) by choosing an random number R_θ between -1 to 1. Therefore the direction of the phonon becomes $\Lambda_0 \text{Sin}\theta = \Lambda_0 R_\theta$. Where Λ_0 is the phonon mean free path which larger than the nano wire length L . Therefore, we can consider that phonon is only colliding with the nanowire surface before pass through the nano wire length (for specular reflection) or may be reflected in the same side (for diffusive case). When the surface is totally specular the incident phonon on the wall of the wire reflected with the same angle in opposite direction (Fig.3.5(B,C)). Then we also make a random sample of the surface roughness. For this we choose a random number R_s between 0 and 1 and we define the specularity of the surface by a number P_s . When phonons incidents on the surface, a random number was generated . If the random number, R_s , is less than the number P_s the reflection

is specular otherwise it is diffusive. When the reflection is diffusive it can randomly reflect phonons in all directions (Fig.3.5(D)).

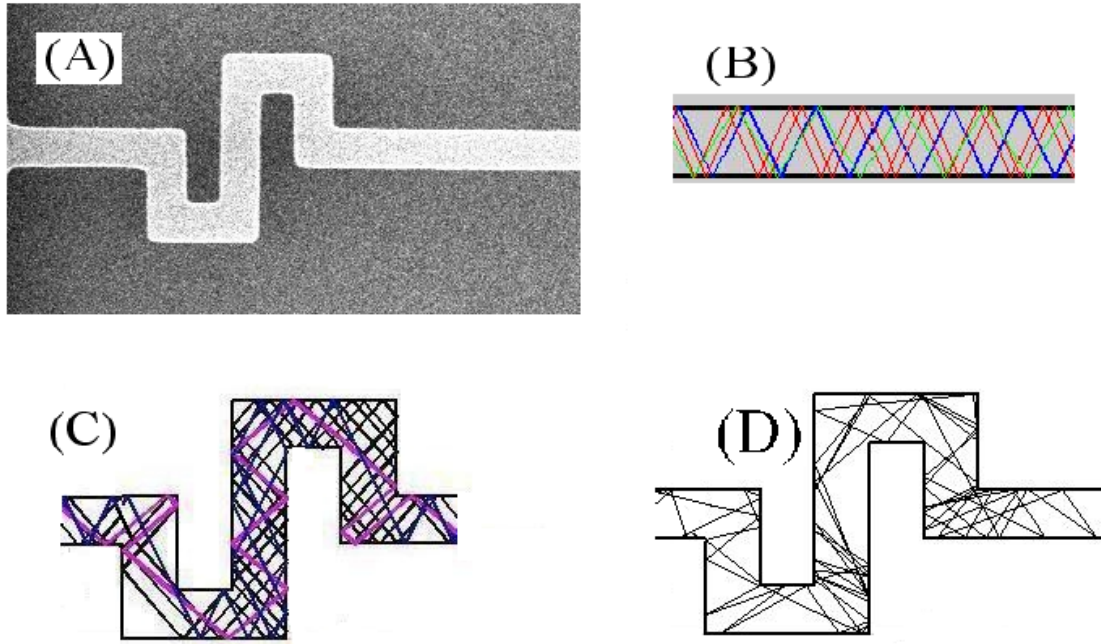


Figure 3.5: (A) The actual length of the nanowire is divided by two because the heater for the experimental measurement is placed on the middle of the wire. (B) Totally specular reflection on the straight nanowire, all the phonon transmitted to the opposite side. (C) Totally specular reflection on the nanowire with one kink. (D) Diffusive type of reflection from the nanowire surface for the kink nanowire.

We did the calculation of the transmissivity for the straight and the bent wire by changing the specularity of the wire from totally specular ($P_s = 1$) to totally diffusive ($P_s = 0$). For the totally specular wire all the phonons launch from the one side of the wire pass through the wire. Therefore the transmissivity is 100 %. In the case of the wire with kink we found the transmittivity is only 40 %. So implementing this bend structure we can block the 60 % of phonons to pass through the wire. When we change the specularity, the difference between the phonon transmittivity of the bent and straight wire decreases and in the totally diffusive case transmissivity for the two

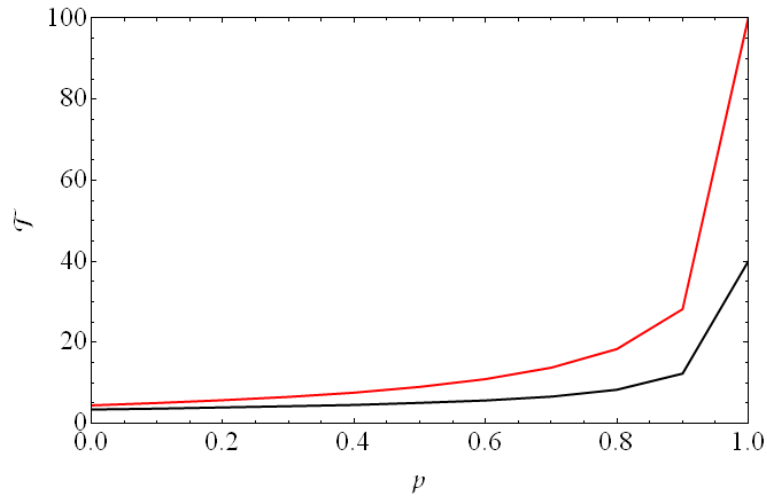


Figure 3.6: Transmissivity(\mathcal{T}) of the straight and bent nanowire for the different specularity (p).

wires are almost same (See Fig.3.6). Because in this case the phonon mean free path became comparable to the nanowire cross section (Casimir's mfp), as the cross section of the both wire are same, the transmissivity also becomes almost equal.

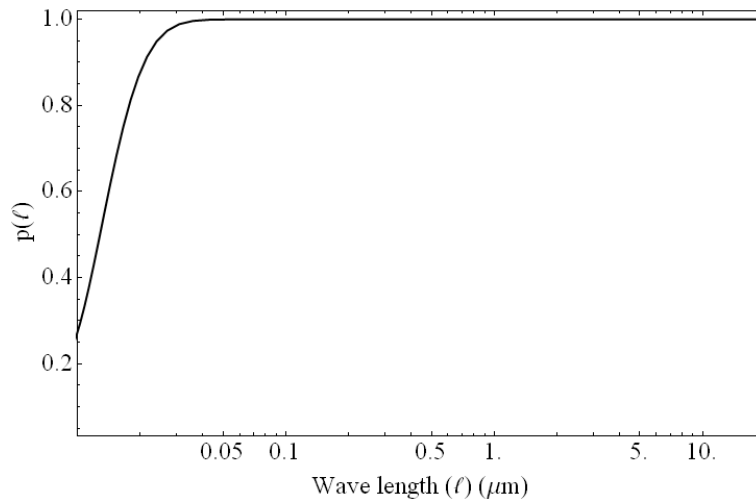


Figure 3.7: calculated specularity ($p(l, T)$) for the different wave length(l) of phonon at 2K temperature.

Now from Eqn.3.14 and Eqn.3.15, we can calculate the transmissivity of the phonon for the different wave length. In the case of the nanowire we made the dimension of the wire such that the dominant phonon wave length, $l_{dom} \gg \eta$. For our nanowire the average *asperity*, η_0 is 4.4 nm. From Eqn.3.15 we have found that the most of the phonon will be reflected specularly from the surface of the wire at very low temperature.

3.4 Results

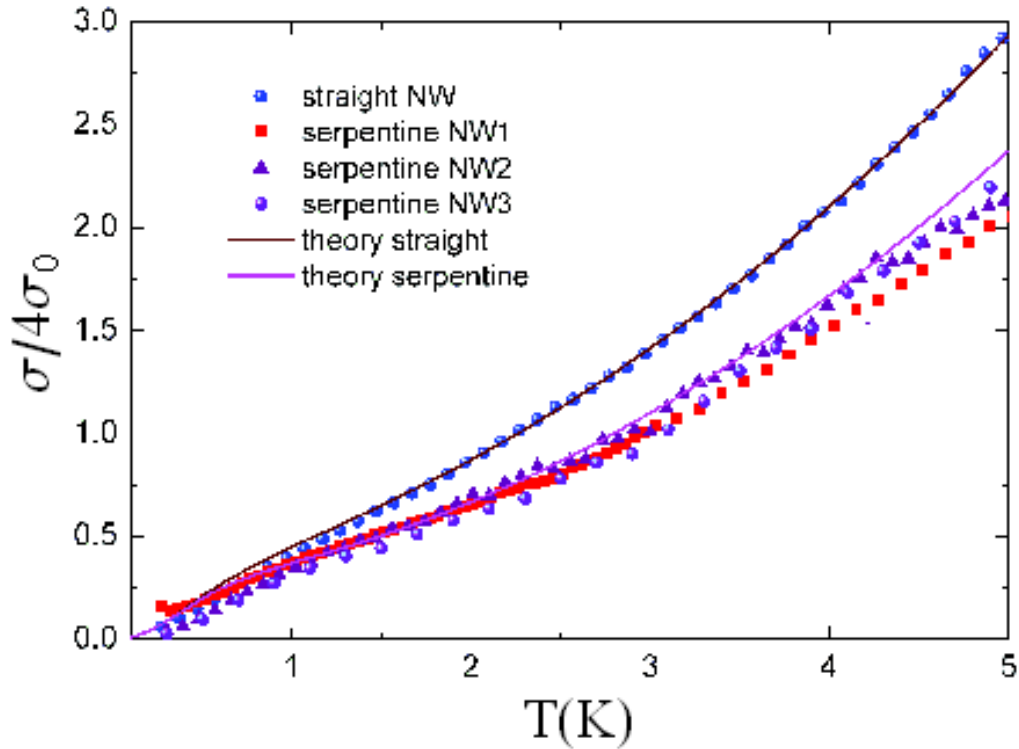


Figure 3.8: Thermal conductance of $5\mu\text{m}$ long nanowires normalized to four times the universal value of thermal conductance versus temperature and the related theoretical fits. The straight nanowire corresponds to the purple curve and the double bent nanowires (three different samples) to the violet curves.

Theoretical low temperature thermal conductance is equal to $4\sigma_0$. Thus the values of the experimental thermal conductance in Fig. 3.8 are presented in units of $4\sigma_0$, and correspond to the thermal conductance of $5\mu\text{m}$ long nanowires (half of the total length of the structures).

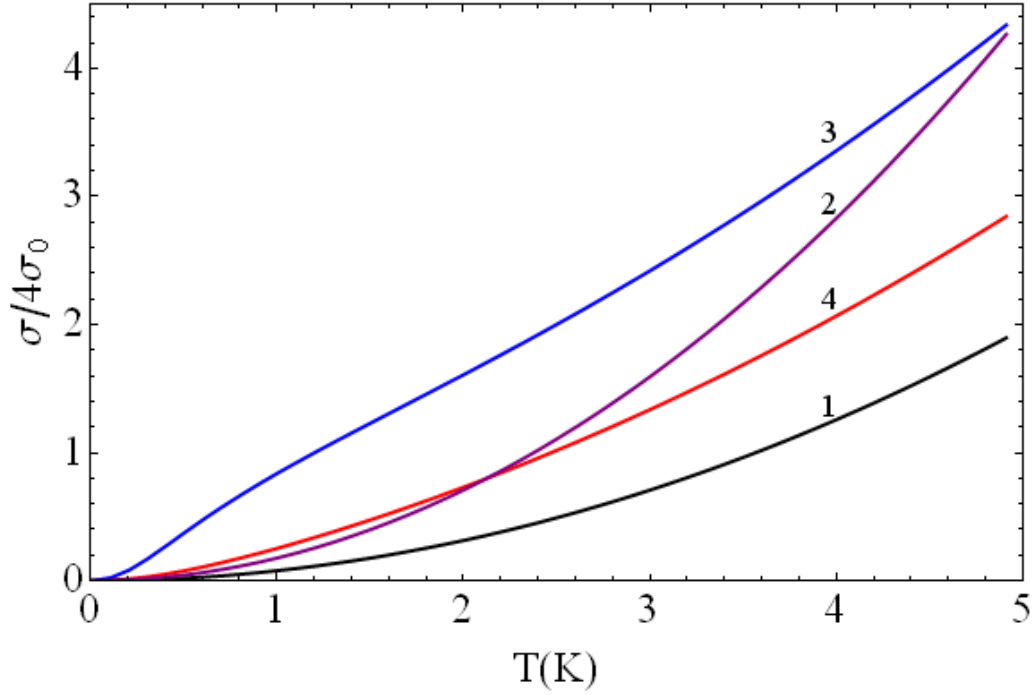


Figure 3.9: Thermal conductance of $5\mu\text{m}$ long straight nanowires normalized to four times the universal value of thermal conductance versus temperature. The curve 1 corresponds to the thermal conductance calculation with mean free path λ_{Cas} and speed of sound 9000m/s , the curve 2 corresponds to mean free path λ_{Cas} and speed of sound 6000m/s , the curve 3 corresponds to the mean free path λ_{ph} and speed of sound 9000m/s and curve 4 corresponds to the mean free path λ_{ph} with an additional resistivity from the interface and speed of sound is 9000m/s

In Fig. 3.8, we present the thermal conductance measured on the double bend nanowires (DBNW) in purple as compared to the measurement made on the straight nanowire in blue. The measurement on the three DBNW are quite reproducible, giving a value at 3K of the order of $\sim 4\sigma_0$, i.e. 12 pW/K . As expected, the thermal

conductance of each wire is continuously decreasing with the decrease of temperature. However major differences can be seen between the straight wire and the DBNW. The latter are conducting heat much less than their counterpart. The only difference between the two is the presence of the serpentine. This is the main result of this study: via a purely geometrical effect phonon transport can be strongly blocked, resulting in a reduction of the thermal conductance between 20% and 40%.

In order to understand this significant reduction of heat transfer in the DBNW, we have performed a numerical simulation of the phonon transport process through the structure. In the real experiment, heat is injected in the wire from the NbN transducer placed on top of it, all throughout the wire length. The largest fraction of this injected heat enters around the center of the structure, where the temperature gets highest. In the simulation we have made the simplifying assumption that heat is injected at the center of the structure, dissipating towards the two wire edges and into the bulk monolithic contacts. We thus calculate the thermal conductance of half the wire, which will be compared with the experimental results presented in Fig. 3.8.

First we did the simulation for the straight wire using equations 3.4, 3.5 and 3.10. For the straight wire t_{obs}^{-1} will be 1. The thermal conductance of the straight wire at this temperature range can not be explained with the simple Ziman or Casimir's model. In the Fig.3.9 we have shown the conductance calculated with the different transmission functions.

Considering totally diffusive surface as Casimir's model (when transmissivity becomes $\frac{4\lambda}{3L}$) and the average speed of sound as $6000m/s$, we have obtained very high conductance (line 2 in the Fig.3.9) and with the average speed of sound as $9000m/s$, the conductance (line 1 in the Fig.3.9) is lower than the experimentally measured values. Now considering the correction term for the roughness as given by Eqn.3.11, thermal conductance (line 3 in the Fig.3.9) of the nanowire with the dimension $100 \times 200nm^2$ and length $5\mu m$ and speed of sound $9000m/s$ is still higher than the experimental values. Therefore, to fit the experimental result, we considered an additional resistive contribution at the interface between the thermometer and the nanowire, in the form of an intrinsic reduction of the transmission probability of the transverse modes. This additional contribution $t_{interface}^T$ is added as in Eq. 3.10. This implicitly assumes that scattering with asperities does not mix different branches. Using a value of $t_{interface}^T = 0.017$, and a mean asperity of 4 nm yields a very good match between theoretical and experimental curves (line 4 in Fig.3.9). We stress that this only works if it is the transverse modes that are blocked. Trying to block the longitudinal mode only, or all three modes in the same amount, does not yield a reasonable agreement with experimental data. Further support of this hypothesis comes from the fact that the wire with the serpentine can be fitted very well using this assumption,

with the same parameters as for the straight wire (see next paragraph). Additional investigation of thermal transport across the NbN:Si interface might provide further evidence on whether this strong mode selectivity is truly occurring.

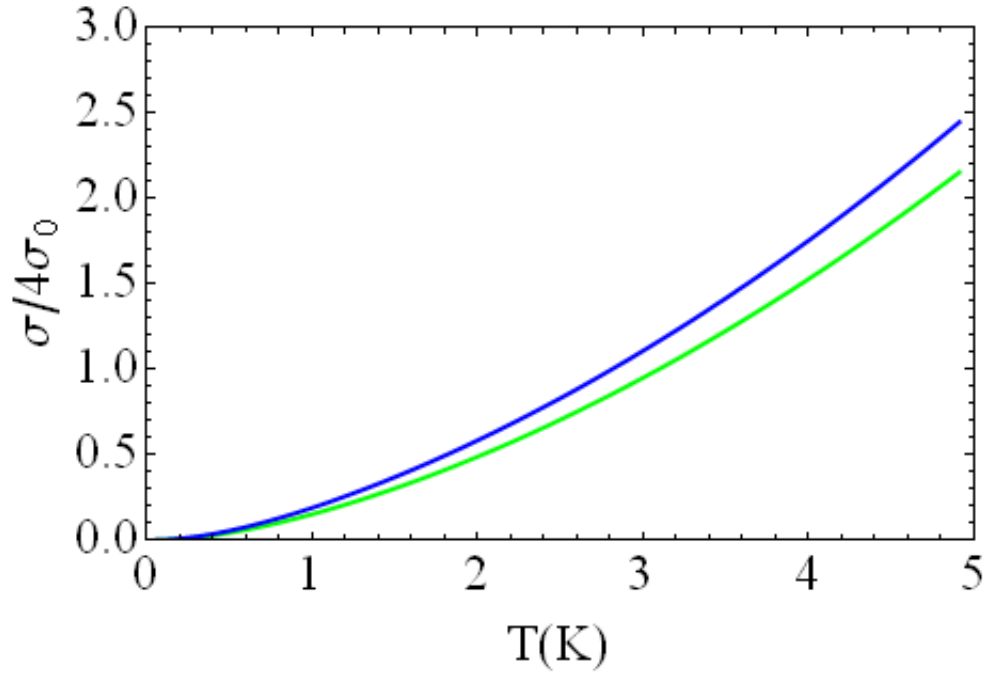


Figure 3.10: Thermal conductance of $5\mu\text{m}$ long bend nanowires normalized to four times the universal value of thermal conductance versus temperature. The blue curve corresponds to the thermal conductance calculation with $t_{obs} = 0.4$ and speed of sound 9000m/s and the green line corresponds to the $t_{obs} = 0.2$ and speed of sound 9000m/s .

To model the conductance of the nanowire with the serpentine, we use Eq. 3.10 in place of Eq. 3.7. The simplest is to assume that t_{obs} is frequency independent. This allows us to estimate its value by fitting the experimental curve. A best fit is obtained for $t_{obs} = 0.2$ (corresponds to the green curve in Fig. 3.10 and violet line in Fig. 3.8).

Blue line in the Fig. 3.10 corresponds to $t_{obs} = 0.4$. We have obtained $t_{obs} = 0.4$ for the bent wire with the MC simulation. Calculated thermal conductance with $t_{obs} = 0.4$ is little bit higher than the experimentally obtained values. So we consider t_{obs} equal to 0.2 which is the same order as the numerically obtained value. The numerical discrepancy with the best fit result may be due to some of the simplifying assumptions used in the model, and the classical character of the Monte Carlo approach, and/or

some degree of experimental uncertainty. The model thus allowed us to estimate an intrinsic 80% reduction in phonon transmission probability due to the serpentine. The thermal conductance reduction is not as large, because this effect is acting in series with the resistive effect of asperity scattering, which masks the former.

The fitted mean asperity value of 4 nm is of the same order of the SEM observed irregularities, thus the asperity treatment developed above appears to be adequate. The lowest temperature part of the measurements matches well with the theory for a value of $f_{adj} = 0.5$, which is of order 1 as expected. This confirms the adequacy of approximated Eq. 3.9 to analyze the low temperature conductance(Fig.3.8).

3.5 Conclusion

1. We have obtained a striking 20-40% reduction of conductance at low temperature due to a double-bend junction in the nanowire.
2. To model this reduction theoretically, we find that a simple Casimir's type model is not adequate to explain these results. Therefore, we adopted an frequency independent transmissivity calculation for these nanowires.
3. The experimental conductance of these nanowires only can be explainable with the phonon of the longitudinal branch. We have blocked the transverse phonon in the theoretical calculation. The result can not be obtained by blocking the transverse branch and longitudinal branch of same amount. Therefore, we conclude that only longitudinal phonon frequency can transmitted at the contact of the wire and thermometer.
4. The geometrical effect reported could be further enhanced by using nanowires having very smooth surfaces. Furthermore, it might be possible to implement the bent structure in smaller nanowires at the scale of 1 nm to be effective at room temperature.

Chapter 4

Thermo Electric Properties of SiGe NanoPowder

Contents

4.1 Introduction	69
4.2 Thermal Conductivity	72
4.2.1 Experimental Measurement	72
4.2.2 Theoretical model of Lattice Thermal conductivity	75
4.3 Electrical Properties	76
4.3.1 Experimental Measurement	76
4.3.2 Theoretical model for the Electrical Properties	76
4.4 Results	81
4.4.1 Modelling of Bulk Materials	81
4.4.2 Modelling of Nanograined sintered materials	88
4.4.3 Characterization and Modelling of larger grain sintered materials	91
4.4.4 The potential for further ZT improvement in nanograined SiGe .	93
4.5 Conclusion	98

4.1 Introduction

Recent experimental discovery that nanostructured alloy materials can improve the figure of merit, ZT , has lead us to an investigation on the nanostructured SiGe alloy material. In some recent publications[116, 117], we have observed that nanostructured bulk alloys pose very low thermal conductivity compared to their bulk materials[118, 119]. The same approach has also been demonstrated in Bi_2Te_3 and other alloys [120, 121, 122]. The main reason behind these enhancements is an important reduction in lattice thermal conductivity due to increased phonon scattering

at the grain boundaries. This idea had been proposed some decades ago, and theoretical analyses predicted the feasibility of reducing κ and enhancing ZT in SiGe by grain boundary phonon scattering [123, 124]. Experimental decrease of κ was also observed [85]. During the last two decades, bulk SiGe alloy has been analyzed very rigorously due to their low thermal conductivity, which is very useful for different modern thermo electric applications [117, 125, 126, 127]. Although bulk SiGe alloys poses low thermal conductivity for the alloy disorder scattering, the figure of merit, $ZT = S^2\sigma T/\kappa$, does not improve as expected[127]. Recently nanostructured SiGe bulk material, fabricated by ball milling and hot pressing procedure, has shown considerable improvement on the figure of merit. In these nanocomposite alloy materials the grain size is $\approx 15 - 50$ nm, so the phonon which have mean free path comparable with the grain size, are scattered very much by the grain boundary and the electrons which have much lower mean free path are not affected so much. This grain boundary phonon scattering further reduced the thermal conductivity and also improved the ZT values. This nanostructured SiGe will be very useful in the power generator application[128]. Recently Silicon-Germanium alloy has been used for power generation in temperature range $600^\circ\text{C} - 900^\circ\text{C}$ in radio isotope power generators (RTGs) for deep space missions to convert radio isotopes energy into electrical power. The optimal efficiency of the power generator is defined by Eqn.4.1

$$\eta = \frac{Th - Tc}{Th} \frac{\sqrt{1 + ZT} - 1}{\sqrt{1 + ZT} + Tc/Th}, \quad (4.1)$$

where Th and Tc are the hot-end and cold-end temperature of the thermoelectric materials, and T is the average temperature of the system between Th and Tc. So it is important to use materials with high ZT value for this kind of application and an improved and better ZT will provide more energy efficient power generation.

In this chapter we will present experimental measurements of the thermal conductivity, Seebeck coefficient and electrical conductivity at high temperature of $Si_{0.8}Ge_{0.2}$ alloy materials. We also present a theoretical model to predict these thermo electric properties of SiGe alloys at different temperature for different carrier concentration and for different volume fraction of Ge.

*p*type and *n*type $Si_{0.2}Ge_{0.8}$ were fabricated by ball milling and hot pressing procedure. This fabrication technique is very simple and also very low cost. Therefore we can use this method very easily for the commercial production of TE materials. The ball-milling and hot pressing method has been employed to produce thermo-electric composites since 1960's. In the early stage, only micrometer sized particles were obtained from the ball milling. Grain size of these particles varies from several micrometers to one hundred micrometers. Thermal conductivity of these hot-pressed

materials decreased from that of the single crystal mainly due to imperfection scattering by the boundary. The ZT peak of the materials consisting of micrometer size grain was increased by nearly 20%. Recently, using high-energy ball-milling procedure, large quantity of nano size powder can be produced. After the hot-pressing the size of the grains still remain in the nano meter range. Here, first, nano powder is made by ball milling. The size of nano powder grains are in average $5 - 15nm$. These sizes depended on the milling time. Then the bulk nano composites were made by an optimized mechanical alloying step. Hot Uniaxial Pressure (HUP) and Spark Plasma Sintering (SPS) have been used for sintering the powders, enabling very different thermal ramp time scale during compaction cycles. For the former method, heating is generated by standard thyristor with a typical thermal heating rate of $10^{\circ}C/min$, while the latter reaches $300^{\circ}C/min$. After the hot pressing, we got the bulk nano composite materials Fig.4.1. The detailed fabrication technique of these materials was given in Ref.[129].

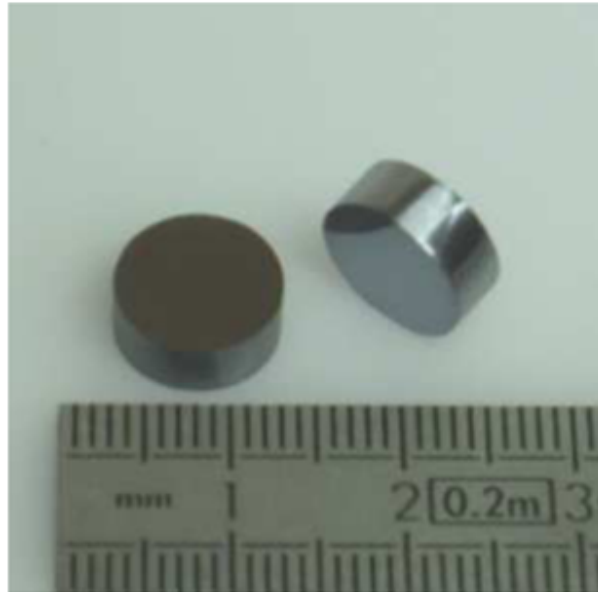


Figure 4.1: $Si_{0.2}Ge_{0.8}$ bulk nano composites materials. This materials was fabricated by the group in LITEN/DTBH/LCTA Ref.[129].

Then we measured the thermal diffusivity, α , by the laser flash technique and the specific heat, C_p , by differential scanning calorimetry (DSC). After that we calculated the thermal conductivity for different temperature by $\kappa = \alpha\rho c_p$, where κ is the thermal

conductivity, and ρ is the density of the materials. Electrical conductivity was also measured by four probe method and Seebeck coefficient was measured by a tool applying temperature difference on the two sides of the materials.

4.2 Thermal Conductivity

Thermal conductivity of a nanostructured material can differ from the bulk material due to several reasons. First, boundary and interface scattering effects may dominate over the volumetric effects such as umklapp and alloy scattering. Secondly, since the nanostructured materials are generally made by technique such as chemical vapor deposition, and sintering methods, they may contain micro-structure or porosity that is different from the bulk sample.

4.2.1 Experimental Measurement

There are different techniques to measure the thermal conductivity of materials. These techniques can be divided in two general categories depending on the time dependent of the heating source, i.e. whether the heating is steady or transient. Steady state techniques use a time independent heat flux to impose a temperature gradient on the sample. The temperature difference over a known distance is then measured and the thermal conductivity is readily calculated. Steady state techniques offer the advantage of generally being simple to use, however they have several drawbacks. One such disadvantage is that heat losses due to blackbody radiation can result in a large amount of error. Furthermore, low conductivity samples can be particularly troublesome as a larger fraction of heat is lost to the surroundings. This error can be reduced through the use of radiation shields or carefully shaped samples, however this complicates the experimental setup and sample preparation. Another shortcoming is that long periods of time are often required in order to reach steady state conditions.

Additional problems arise for steady-state measurements of thin films as temperature gradients across a film are often small and the process of measuring these small temperature differences can often influence the actual temperature itself. Moreover, in order to measure the temperature gradient across a film, extensive processing may be required to place a temperature sensor on both the top and bottom of a film. This makes it difficult to measure the conductivity of a particular film directly without having to fabricate separate samples, which may be different than the actual sample of interest.

Transient techniques utilize a time-dependent heat flux, typically in the form of a periodic heat source or as a heat pulse, and measure the time dependent temperature

change and compare this value with an analytical or numerical solution of the heat equation. As a result of the time dependent nature of the heat flux, instead of measuring the thermal conductivity directly, most transient techniques actually measure the thermal diffusivity α , which is defined as $\kappa/\rho C_p$ [130] where κ is the thermal conductivity, ρ is the density, and C_p is the specific heat per unit mass. Therefore, in order to extract the value of the thermal conductivity, the density and specific heat must also be known which can be a source of uncertainty. One significant advantage of transient techniques is that long equilibration times are not needed, as most techniques require only a few periods of heating which generally is on the order of a few seconds.

For the *SiGe* nano composite materials we used the Laser Flash Technique to measure thermal diffusivity and specific heat for different temperature. The Laser Flash Technique is based on the transient approach.

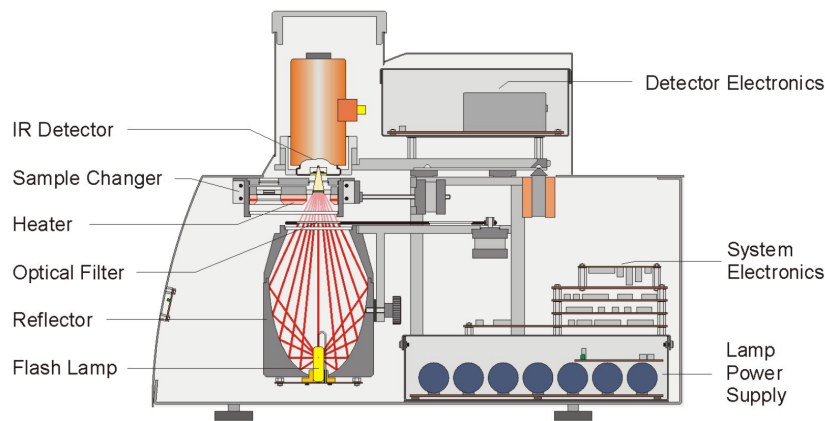


Figure 4.2: schematic diagram of Laser Flash Technique.

Using this method, the front side of a plane-parallel sample with a well defined thickness is heated by a short light or laser pulse. The resulting temperature rise on the back surface is measured versus time using an infrared detector. Analyzing the measured detector signal with appropriate mathematical models yields information on thermal diffusivity and the specific heat of a material. Together with the density of the material the thermal conductivity can be determined.

Samples are generally prepared with diameter of 10 mm, and 1 mm width. The sample is then placed inside a holder and the front surface is heated by a short light pulse. The temperature rise on the rear surface is measured versus time using an IR detector.

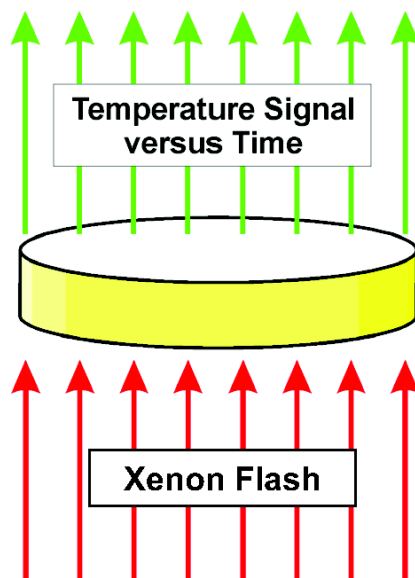


Figure 4.3: Thermal diffusivity and specific heat measurement by Laser flash.

The total thermal conductivity was calculated from $\kappa_T = \alpha \times \rho \times C_p$, by individually measuring α and c_p . Thermal diffusivity measurement of different samples was given in Fig.4.4

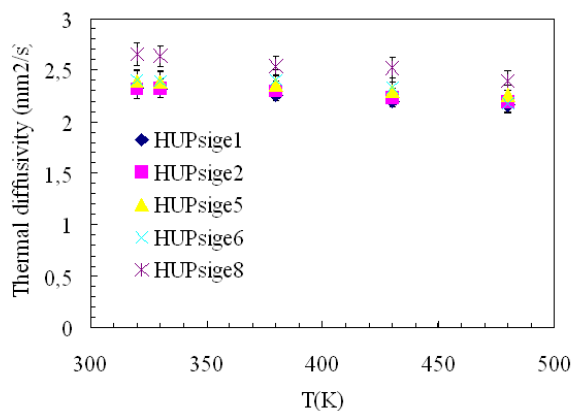


Figure 4.4: Thermal diffusivity Vs Temperature for the ptype and ntype $Si_{0.8}Ge_{0.2}$, measured by the Laser flash technique.

And specific heat was measured by differential scanning microscope(DSC),

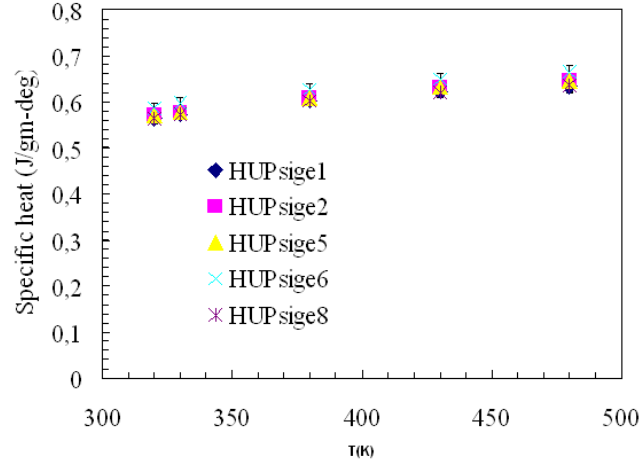


Figure 4.5: Specific heat Vs Temperature for the ptype and ntype $Si_{0.8}Ge_{0.2}$, measured by Differential scanning calorimetry .

4.2.2 Theoretical model of Lattice Thermal conductivity

The lattice thermal conductivity of the alloy can be defined by using callaway model,

$$\kappa_{la} = \frac{1}{\pi c} \int_0^{\omega_c} \frac{df_B}{dT} \tau(\omega) \omega^2 \hbar \omega d\omega / 2\pi, \quad (4.2)$$

where $\tau(\omega)$ is the total relaxation rate, c is the speed of sound in the material, and f_B is the Bose distribution. The relaxation rate of bulk $Si_{(1-x)}Ge_x$ due to anharmonic scattering, alloy scattering and ionized impurity is given as[83, 84, 79]

$$\frac{1}{\tau_{an}} = BT\omega^2 e^{-C/T} \quad (4.3)$$

$$\frac{1}{\tau_{al}} = x(1-x)A\omega^4 \quad (4.4)$$

$$\frac{1}{\tau_{dop}} = D\omega^4 \quad (4.5)$$

where A, B, C and D are parameters adjusted for the high T dependence of the single crystal materials. The anharmonic scattering is a gross simplification of Umklapp Scattering. For doped n type and p type nanocomposites materials, we

included the extra scattering rate due to the doping concentration. The impurity scattering and alloy scattering are derived from the Rayleigh formula.

The grain boundary scattering for the SiGe alloy can be defined from Ref.[131].

$$\frac{1}{\tau_{gb}} = \frac{v}{LB_1} \quad (4.6)$$

where v is speed of sound in SiGe and L is grain size of the nano composite and $B_1^{-1} = \frac{1}{36}\gamma^2\varphi^2$. Here γ is the Gruneisen constant for SiGe. Value of the Gruneisen constant of SiGe for different Ge volume fraction is given in Ref.[132] as $\gamma = 1.01$. φ is the angle of misfit.

4.3 Electrical Properties

4.3.1 Experimental Measurement

Experimental measurement of the electrical conductivity, Seebeck coefficient and mobility was performed by collaborators of our group on the SiGe samples [133]. These measurement techniques are from the state of art method. Electrical conductivity of the samples are measured by the four probe point technique. For some samples we had performed Hall effect to the carrier concentration and carrier mobility.

To measure the Seebeck coefficient we applied a temperature gradient. Cold-side was fixed at $25^\circ C$ and the temperature of the other side was increased and then we measured the voltage created by this temperature difference. We get a curve of voltage versus the difference of temperature and the slope of this curve is the Seebeck coefficient.

4.3.2 Theoretical model for the Electrical Properties

To model the electrical conductivity, Seebeck coefficient and electronic part of the thermal conductivity, we use the Boltzmann transport equation in the relaxation time approximation. Previously different authors modeled the thermo electric properties of bulk SiGe[134, 118, 135], by considering different scattering mechanisms. In Ref[118, 136], they parameterized the acoustic scattering and ionized impurity scattering to explain the experimental result for the degenerate SiGe bulk materials. These two authors predicted different values of DOS effective mass, the dielectric constant and the deformation potential. From the Ref[136], the intervalley scattering and the alloy scattering is not also clear. In Ref[135, 137], the authors had defined the alloy scattering for the non-degenerate values, and as in the degenerate materials the

doping concentration is very high, there will be significant change in alloy scattering and ionized impurity scattering. Here we present theoretical calculation of Seebeck coefficient and electrical conductivity and electronic part of thermal conductivity by considering relaxation rate due to the acoustic scattering, τ_{ac} , intervally scattering, τ_{in} , impurity scattering, τ_{ii} , and alloy scattering, τ_{al} . For the SiGe alloy materials we used two conduction bands and one valence band extrema. As in the SiGe alloy have two conduction band minima at X($\langle 111 \rangle$) and L ($\langle 100 \rangle$) point. Since SiGe is a non polar material and intervalley *scattering in* rate is canceled due the selection rule[138]in this kind of material, we can consider there are no inelastic scattering. Therefor the relaxation time approximation is appropriate for the SiGe alloy.

In the relaxation time approximation, we can express the transport equation as,[139]

$$\sigma = e^2 \int_{-\infty}^{+\infty} d\epsilon \left(-\frac{\partial f_0}{\partial \epsilon}\right) \Sigma(\epsilon) \quad (4.7)$$

$$S = \frac{e}{T\sigma} \int_{-\infty}^{+\infty} d\epsilon \left(-\frac{\partial f_0}{\partial \epsilon}\right) \Sigma(\epsilon) (E - \delta) \quad (4.8)$$

$$\kappa_{el} = \frac{1}{T} \int_{-\infty}^{+\infty} d\epsilon \left(-\frac{\partial f_0}{\partial \epsilon}\right) \Sigma(\epsilon) (E - \delta)^2 - \sigma S^2 T \quad (4.9)$$

For the parabolic band approximation the transport distribution function can be written as $\Sigma(\epsilon) = N(\epsilon)v(\epsilon)\tau(\epsilon)$, where v is the group velocity of the carrier, $N(\epsilon)$ is the density of states, e is the carrier charge, δ is the level of chemical potential at a particular temperature, T , and τ is the total relaxation rate. We get the total relaxation rate by using Mathiessen's rule,

$$\frac{1}{\tau} = \sum \frac{1}{\tau_i} \quad (4.10)$$

Now the different relaxation rates can be expressed as explained below [140, 137]. Electron scattering by lattice vibration, i.e. by the the phonon eigenstates was described by the Bardeen and Shockley[141]. Phonons disturb the lattice, that moves the atoms from their original position in the lattice. An electron is affected by this position changing and may liable to be deflected or scattered. For a parabolic band considering isotropic valley, the differential scattering rate was proposed by[140]. The relaxation rate for the acoustic deformation potential was given by

$$\frac{1}{\tau_{ac}} = \frac{e^2 k T E_1^2 m^*}{\pi \hbar^3 c_l} \quad (4.11)$$

where E_1 is the intravalley deformation potential, c_l is the longitudinal elastic constant.

Acoustic relaxation rate $\frac{1}{\tau_{ac}}$ is proportional to k and leads to nearly constant mean free path. The corresponding partial mobility due to acoustic scattering is proportional to $T^{-3/2}$. All the parameter in Eqn.4.11 depend on the materials. For Si, Ge, and SiGe we have listed all this parameter at Table.4.1 from literature.

The relaxation rate of electron scattering due to ionized impurity was given in Eqn.4.12 [140].

$$\frac{1}{\tau_{ii}} = \frac{e^4 N m^*}{8\pi \epsilon_0^2 \hbar^3 k^3} \left(\ln \left(1 + \frac{4k^2}{\beta} \right) - B \right) \quad (4.12)$$

The relaxation rate due to ionized impurity $\frac{1}{\tau_{ii}}$, is approximately proportional to $1/k^3$ and gave a $T^{3/2}$ partial mobility dependence, aside from screening factors. Screening effects appears only in the logarithmic term and through the B term in Eqn.4.12. Where $B = 4k^2/(\beta^2 + 4k^2)$, ϵ_0 is the low frequency dielectric constant. When the Born approximation ($4k^2/\beta^2 \gg 1$) is valid, we can consider the screening length as given by Dingle's expression [138] neglecting the neutral impurity concentration. The inverse screening length β is given by as

$$\beta^2 = (e^2/\epsilon_0 kT) \int (k/\pi)^2 f(1-f) dk \quad (4.13)$$

For the ntype f is the Fermi distribution function of the electron and for the ptype it is the Fermi distribution function of the positive charge, i.e.; holes. In this approximation we assume that all impurities are ionized. Besides that the other approximation in this scattering is that the electron or hole interacts with only one ionized center at a time.

For the indirect band crystal such as Si and Ge besides the above two scattering, we have to include an intervalley scattering. We assume that various indirect equivalent minima are isotropic and parabolic. In Si there are six isotropic valleys in conduction band.

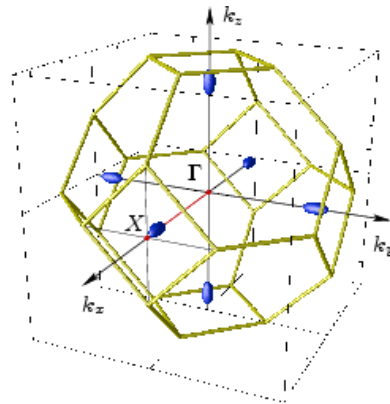


Figure 4.6: First Brillouin zone conduction band valleys.

Now in these different valleys, there are two types of scattering, denoted by f and g scattering. In Fig.4.7 below, from valley 1 transition to valley 2 (g -scattering), requires an X -directed phonon participating in an Umklapp process. For the transitions to the remaining valleys (f -scattering), the phonon labeled f in the figure extends beyond the first Brillouin zone. Hence, reduction of this same phonon to the first Brillouin zone yields the phonon labeled S [27].

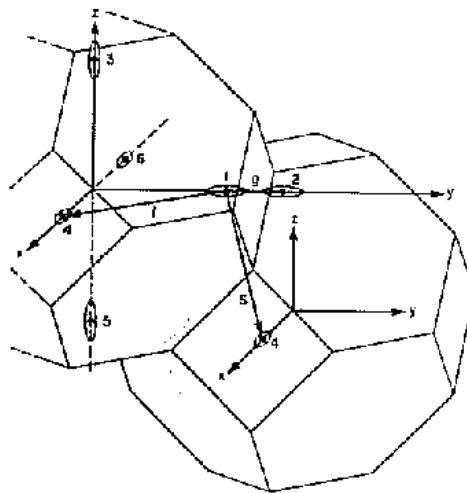


Figure 4.7: Scattering between Si-like minima consists of two different type scattering as illustrated here [27].

Electron effective masses for indirect band gap materials are generally large and the Fermi energy level lies always very close to the band edge. Thus we can consider parabolic band approximation for these materials and the relaxation rate can be expressed as,

$$\frac{1}{\tau_{in}} = (N + 1 - f^-) \frac{e^2 D_e^2 (Z - 1) m^* k^-}{e^2 \pi \rho \hbar^2 \omega_p} + (N_e + f^+) \frac{e^2 D_e^2 (Z - 1) m^* k^+}{e^2 \pi \rho \hbar^2 \omega_p} \quad (4.14)$$

where N is the total number of carrier, $N = \int Z \frac{1}{4\pi^3} 4\pi k^2 f(k) dk$. Z is the number of isotropic valleys at each band. For Si, $Z = 6$ and for Ge, $Z = 4$. D_e is the intervalley deformation potential.

f^\pm is the distribution function evaluated at energy $\delta' = \delta \pm \hbar\omega_p$, $\hbar\omega_p$ is the phonon energy. The intervalley scattering rate is proportional to k' and at high temperature it mimic the acoustic scattering and leads to a $T^{-3/2}$ mobility dependence.

Though the mobility of different materials predominantly depends on the impurity and phonon scattering, in the case of alloy materials it is also affected by disorder arising from aperiodic atomic position and atomic potential. For alloy scattering the relaxation rate can be expressed as,[137]

$$\frac{1}{\tau_{al}} = 2\pi(x - 1)x \frac{A_1 (\sum_i f s_i Z_i g_i(E) \Delta_i)^2}{g_i(E) Z_i} \quad (4.15)$$

where $i = X$ or L and $g(E)$ is the density of carriers in a particular band minimum, $g(E) = (2m^*)^{3/2} E^{1/2} / 4\pi^2 \hbar^2$ and $A_1 = 0.95 \times 10^5$ is a parameter. The value of A_1 is adjusted to obtain the experimental values. For SiGe Δ is defined from Ref.[135]. x is the Ge volume fraction in the SiGe alloy, $f s$ is the s fraction of the density of states, Δ_i is the band gap parameter for the indirect band gap materials. Z_i is the number of isotropic valley, in the case of SiGe number of Z depend on the Ge volume fraction in the alloy. The values of all these parameters are listed in the Table.4.1.

Now for the nanostructured materials, we have defined a scattering rate due to the grain boundary as

$$\frac{1}{\tau_{gb}} = v/l \quad (4.16)$$

Band structure parameter	Symbol (Units)	Value
Low frequency dielectric constant	ϵ_0/ϵ	$11.7(1-x) + 15.98x$
Longitudinal elastic constant	$c_l(N/m^2)$	$19.02(1-x) + 15.03x$
Inter-valley deformation potential, X/L	E_1 (eV)	$7.5(1-x) + 9.5x$
Number of equivalent valleys, X/L	Z	$6/4$
Lattice mass density	$\rho(gm/cm^3)$	$2.33(1-x) + 5.32x$
Inter-valley phonon Debye temperature	$T_e(K)$	$542(1-x) + 382x$
Electron DOS effective mass, X/L	m^*/m	$0.42/0.22$
Hole DOS effective mass	m^*/m	1.5
s fraction in the density of states, X/L	f_s	$0.333 + 0.05(1-x)/0.632 + 0.13(1-x)$
Band gap energy, X	$E_g(eV)$	$0.8941 + 0.0421(1-x) + 0.1691(1-x)^2$
Band gap energy, L	$E_g(eV)$	$0.7596 + 1.086(1-x) + 0.3306(1-x)^2$
Hole- deformation potential	$E_1(eV)$	4.8

Table 4.1: Band structure parameter used in the theoretical calculation of TE properties of Si, Ge and SiGe

4.4 Results

4.4.1 Modelling of Bulk Materials

The modeling of thermoelectric properties by using Boltzmann transport equation is very common practice. For Seebeck coefficient, electrical conductivity and electronic contribution to the thermal conductivity we have calculated the different scattering mechanisms for alloy materials as mentioned in the previous section. Experimental measurements of bulk Si, Ge and SiGe alloy at high doping concentration were reported in Refs.[119, 118, 142, 143]. There are also theoretical models to calculate the mobility of alloy materials [127, 136, 144] considering only impurity scattering and acoustic scattering for six valleys. We have first validated the parameters by reproducing bulk transport properties.

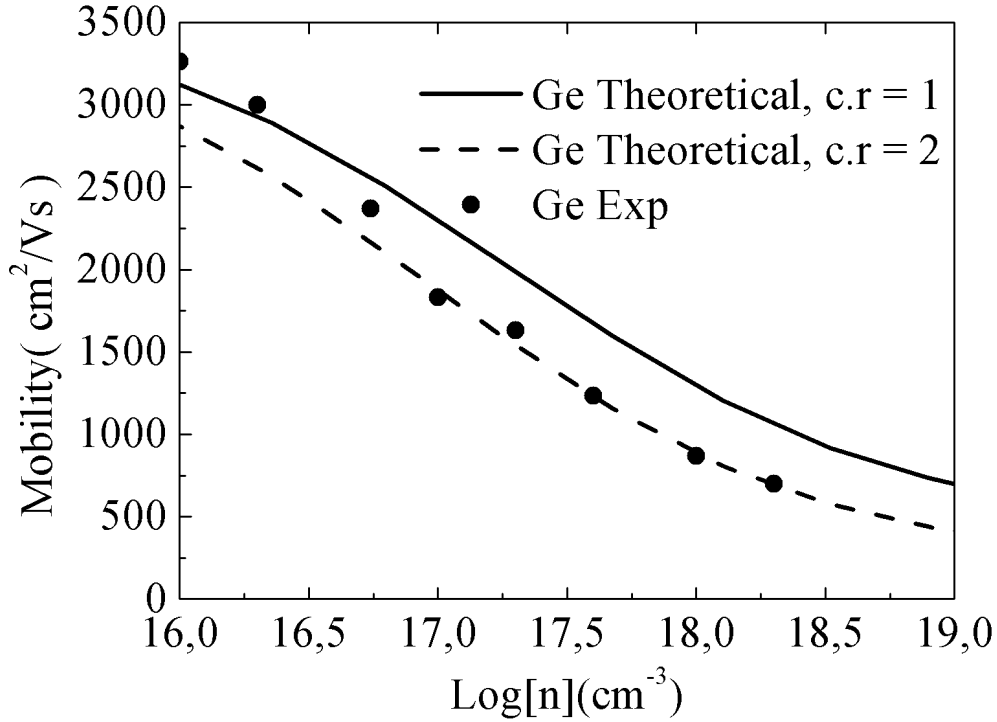


Figure 4.8: Mobility of Ge for different carrier concentration at $T = 300K$, compensation ratio(c.r) 1 and 2. Experimental points are from Ref.[145].

Electrons mobility as a function of carrier density for Ge at high doping is shown in Fig.4.8, and compared with measurements from Ref.[145].

In the case of thermoelectric materials where the carrier concentration or doping level is generally high, transport properties of materials become different than non-degenerate materials. In this case the DOS effective mass of carrier changes from the non-degenerate values and the ionized impurity scattering has an important contribution. In Ref.[140], the high carrier concentration experimental results were well explained by using a compensation ratio greater than unity. At 300K temperature we changed the level of chemical potential with the value of doping and calculated mobility of pure *Si* and *Ge* for different doping level.

Mobility of *Si* for different doping concentration is shown in Fig.4.9.

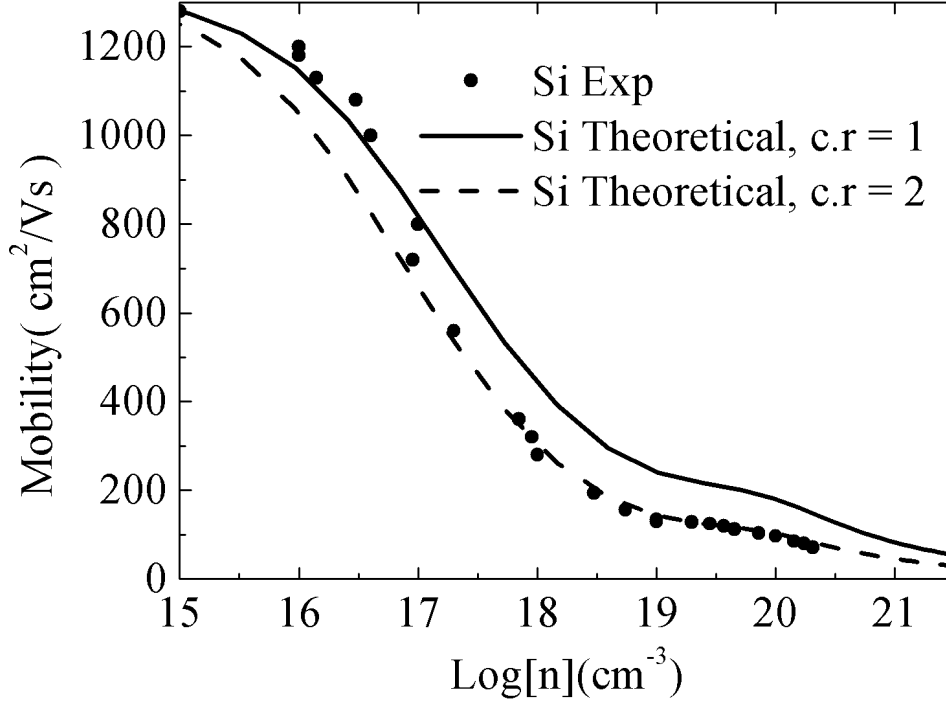


Figure 4.9: Mobility of Si for different carrier concentration at $T = 300K$.

Thus it was clear that higher compensation ratio could better explain the experimental result of pure Si and Ge at the high carrier concentrations. This is mainly due to the change of the scattering mechanisms for the high concentrations. Fischetti has shown that in order to properly match the high concentration mobility for pure Si one needs to include additional scattering mechanisms on top of acoustic and ionized impurity, in particular electron-plasmon and electron-electron interactions[72]. To avoid these complications we have followed Rode, using an ionized impurity compensation ratio of 2 in order to properly match the high concentration data[145].

Therefore, we have also calculated the transport properties of alloy materials for the high doping level with compensation ratio 2. In the Fig.4.10 we plot the mobility of $Si_{0.7}Ge_{0.3}$ and Si for the degenerate carrier concentration. The experimental results which are from Ref.[143] match very well with our theoretical calculation.

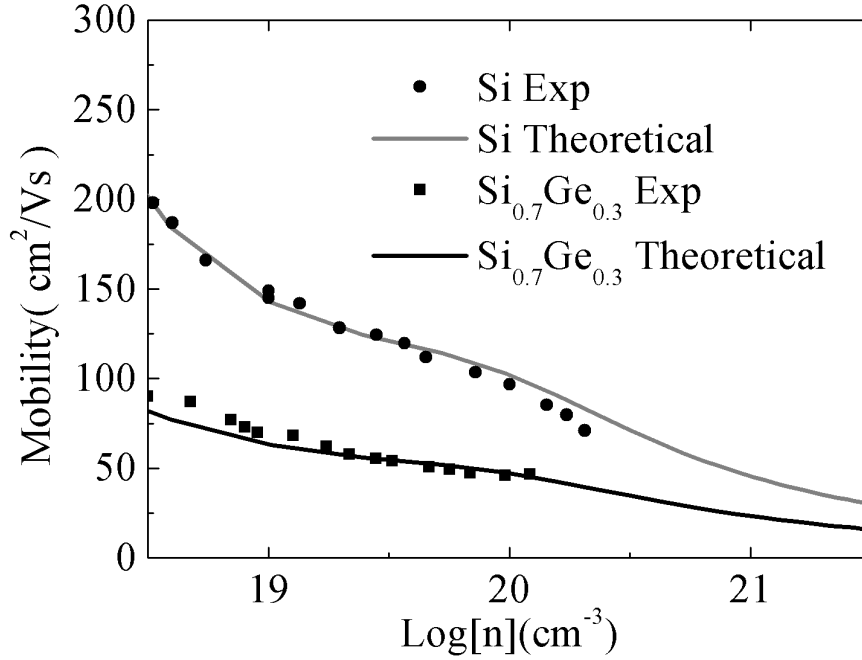
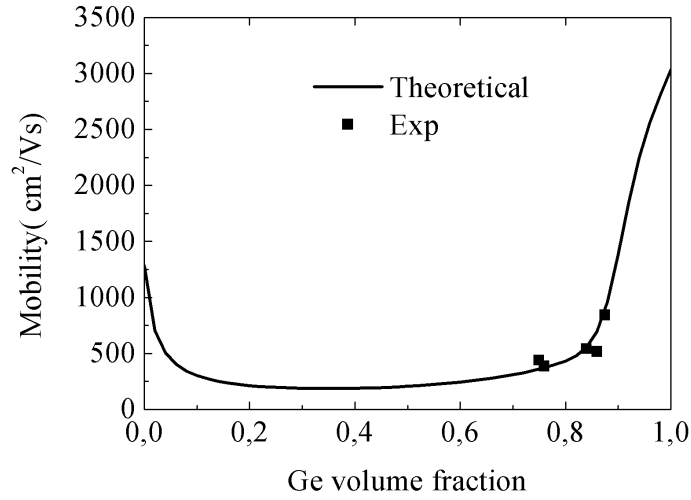


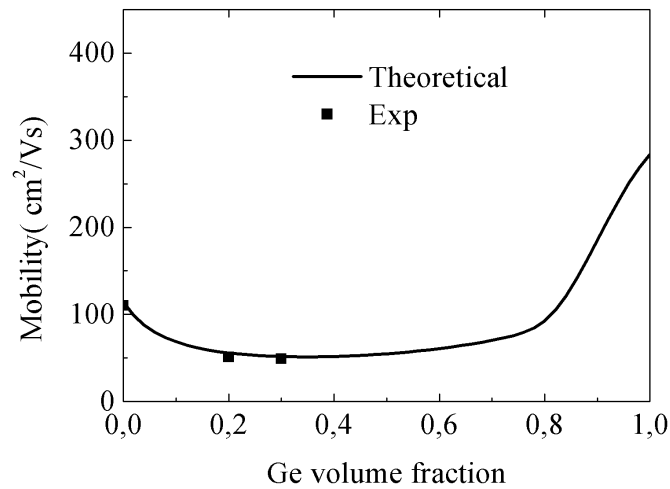
Figure 4.10: Mobility of Si(Black line) and $Si_{0.7}Ge_{0.3}$ (gray line) at 300K for different carrier concentration. Experimental results are from Ref.[143]

We have used all the band structure parameters from Table.4.1. We also implemented two conduction bands minima, X and L(where as in Ref.[127, 136], they used only one conduction band) and there are 6 and 4 degeneracy in these minima respectively.

The carrier mobility of $SiGe$ for different Ge volume fraction at non-degenerate doping concentration have been calculated with the band gap parameter given in Table.4.1 and compensation ratio of impurity scattering as 1. In Fig.4.11, we have presented the calculation of the mobility for different Ge volume fraction in $SiGe$ alloy at low carrier concentration.



Mobility of SiGe for different Ge volume fraction at non-degenerate carrier concentration, $N = 1.4 \times 10^{16}$ at $T = 300K$.



Mobility of SiGe for different Ge volume fraction at degenerate carrier concentration, $N = 5.0 \times 10^{19}$ at $T = 300K$

Figure 4.11: Mobility of SiGe for different Ge volume fraction.

SiGe mobility very much depended on the Ge volume fraction. We had adjusted the compensation ratio of impurity scattering at 2 to obtain the experimental result

of degenerate doping concentration.

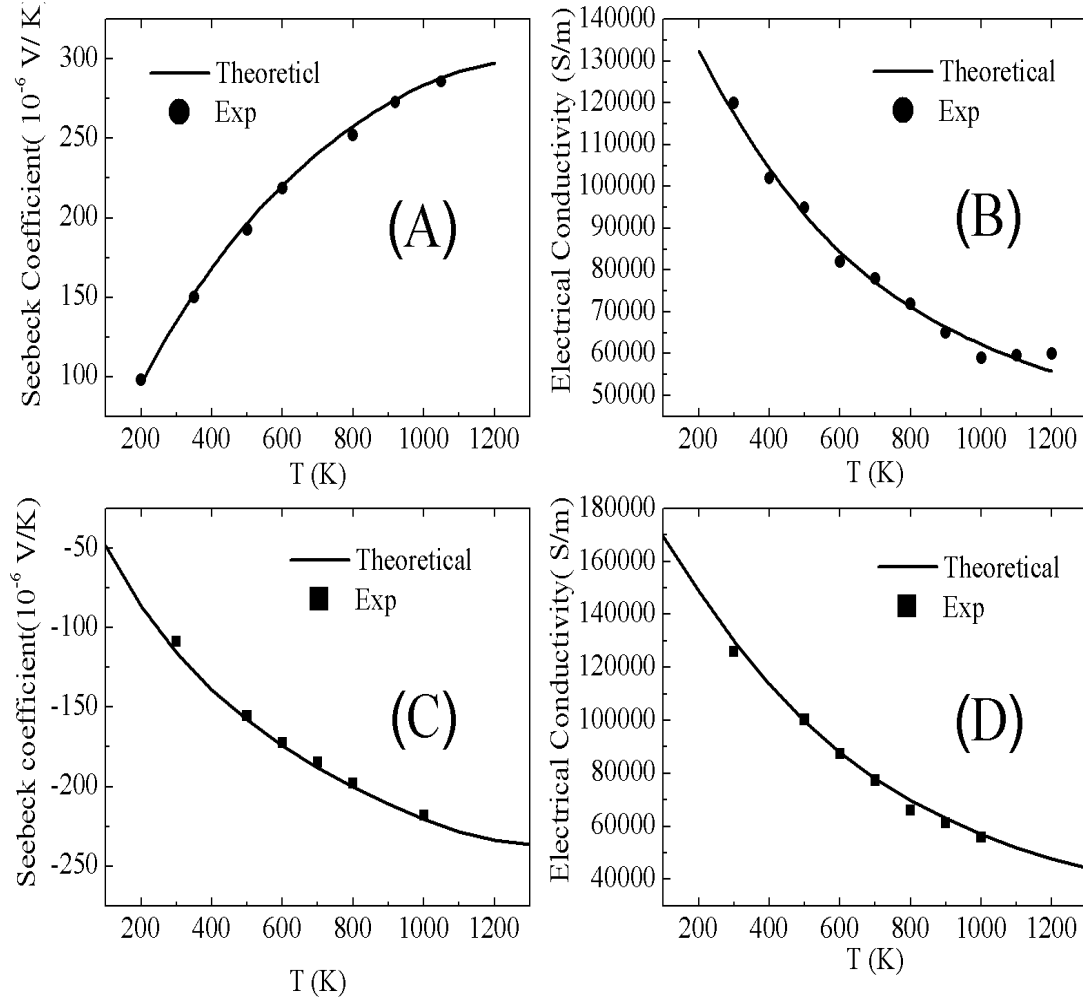


Figure 4.12: (A) Seebeck coefficient of sintered bulk ntype $Si_{0.8}Ge_{0.2}$. Experimental results are from ref.[118]. (B) Electrical conductivity of sintered bulk ntype $Si_{0.8}Ge_{0.2}$. (C) Seebeck coefficient of sintered bulk ptype $Si_{0.8}Ge_{0.2}$. Experimental results are from ref.[119] (C) Electrical conductivity of sintered bulk ptype $Si_{0.8}Ge_{0.2}$.

Seebeck coefficient and electrical conductivity of both ntype and ptype $Si_{0.8}Ge_{0.2}$

have been also calculated from the theoretical model by calculating the chemical potential at high temperature. We have obtained good agreement with the bulk sintered $Si_{0.8}Ge_{0.2}$ experimental results from ref.[119, 118] for both ntype and ptype materials.

Doping concentration are $1.7 \times 10^{20} cm^{-3}$ and $1.8 \times 10^{20} cm^{-3}$ for n and ptype case respectively.

We have also represented electrical conductivity and Seebeck coefficient of the bulk sintered $Si_{0.8}Ge_{0.2}$ for the different carrier concentrations as represented by Jonker in Fig.4.13.

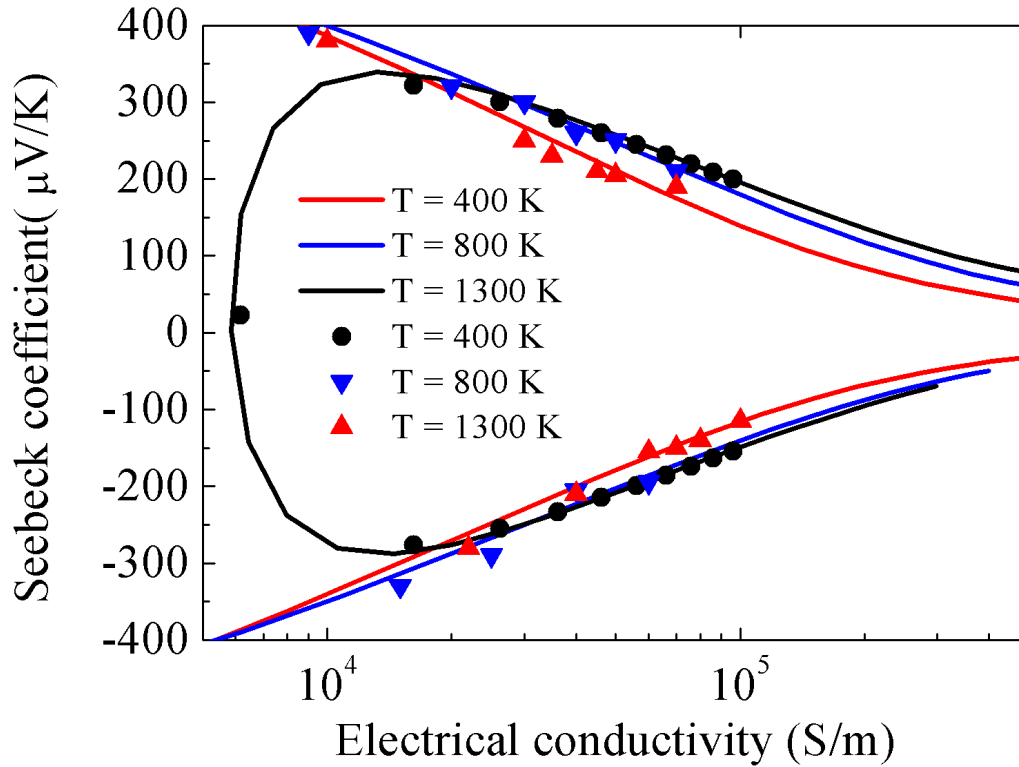


Figure 4.13: Seebeck Coefficient versus Electrical conductivity. Solid lines are the theoretical calculation and the dots are experimental result from Ref.[146] .

In the above Fig.4.13, we have changed the doping concentrations of both ntype and ptype materials at a fixed temperature. Theoretical results of these bulk sintered

materials match well with the experimental results which validate our theoretical model.

4.4.2 Modelling of Nanograined sintered materials

For the nanostructured sintered material, there is a grain boundary scattering for both electrons and phonons by the nanograin. The carrier mean free paths are in general in the order of ~ 5 nm. Thus the effect of grain size on electronic transport is not expected to be large for grains above this size. We have therefore considered a simple form of the carrier scattering rate due to grain boundaries proportional to the grain size, $\tau_{gb}^{-1} \simeq v_e/l_{gb}$, where v_e is speed of the electron and l_{gb} is the grain size. In Fig.4.14 we show the theoretical result for ntype $Si_{0.8}Ge_{0.2}$ along with the experimental result from Ref.[117].

In this theoretical calculation of ntype materials, we have considered that the grain size is 12 nm and the carrier concentration is $2.0 \times 10^{20} cm^{-3}$. In the Ref.[117] the carrier concentration are between $1.8 \times 10^{20} cm^{-3}$ to $2.5 \times 10^{20} cm^{-3}$ and the grain size are 10 to 15 nm. Therefore, the theoretical values are accurate as the experimental values changed 10% in different measurement. We have calculated the lattice thermal conductivity for the materials using the Eqn.4.2 for the nanostructured materials and then we have calculated the total thermal conductivity of the materials by adding the lattice thermal conductivity, κ_l and electronic contribution in the thermal conductivity, κ_e . Total thermal conductivity of different materials match well with the experimental results. Lattice thermal conductivity has been calculated with the mean free path of the grain boundary scattering adjusted by the parameter B_1 . We have adjusted, $B_1 = 20$, to obtain the total thermal conductivity which match well with the experimental thermal conductivity.

In the case of ptype materials we have obtained all the thermoelectric properties with the effective mass of hole (given in the Table.4.1) and the other band structure parameter for the valence band also listed in Table.4.1 . Additionally for the nano size materials we have considered a grain boundary scattering same as ntype materials. The grain size in the bellowing calculation is 20nm and the carrier concentration is $1.8 \times 10^{20} cm^{-3}$. These values are in the range of the experimentally measured values in Ref.[116].

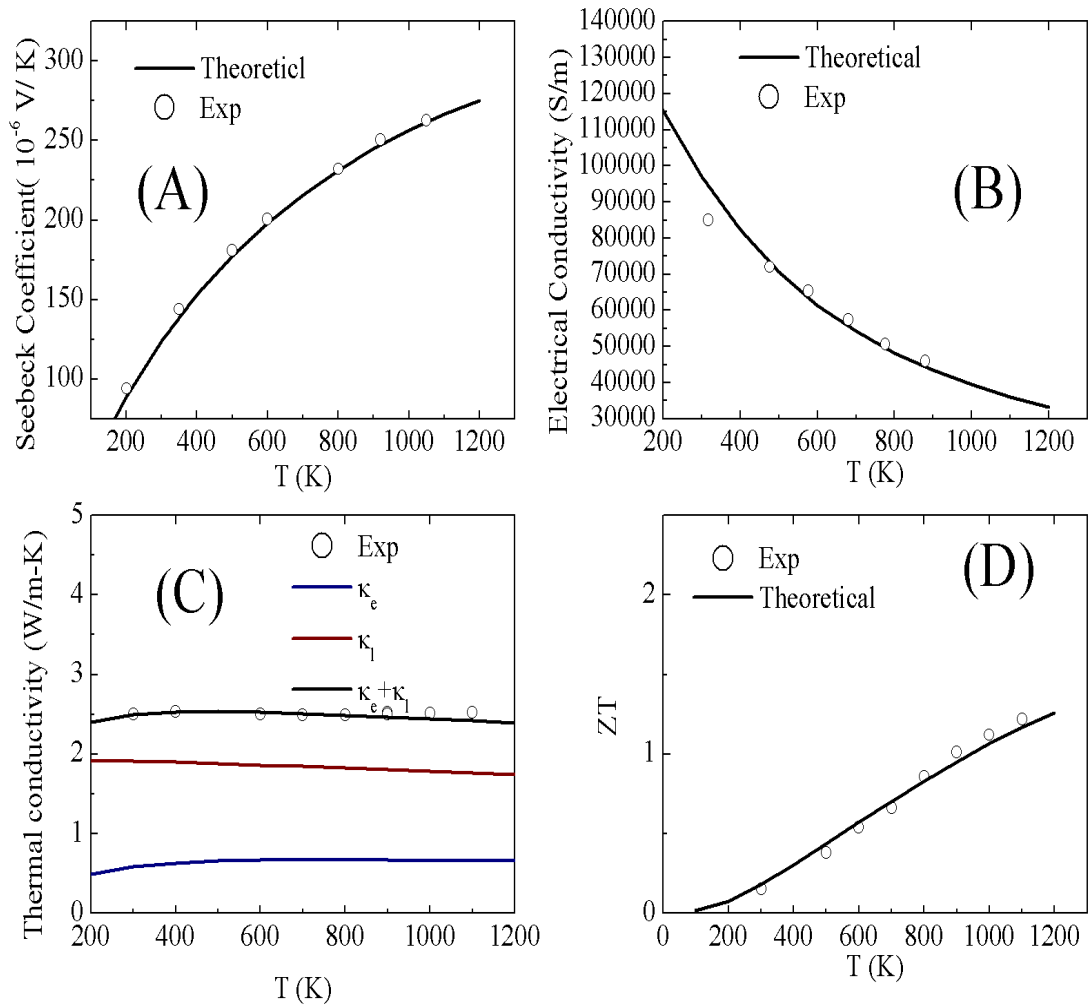


Figure 4.14: (A) Seebeck coefficient of sintered nanostructured n-type $Si_{0.8}Ge_{0.2}$ with grain size 12 nm. Experimental points are from Ref.[117]. (B) Electrical conductivity. (C) Electronic thermal conductivity, lattice conductivity and total thermal conductivity, (C) Figure of merit, ZT .

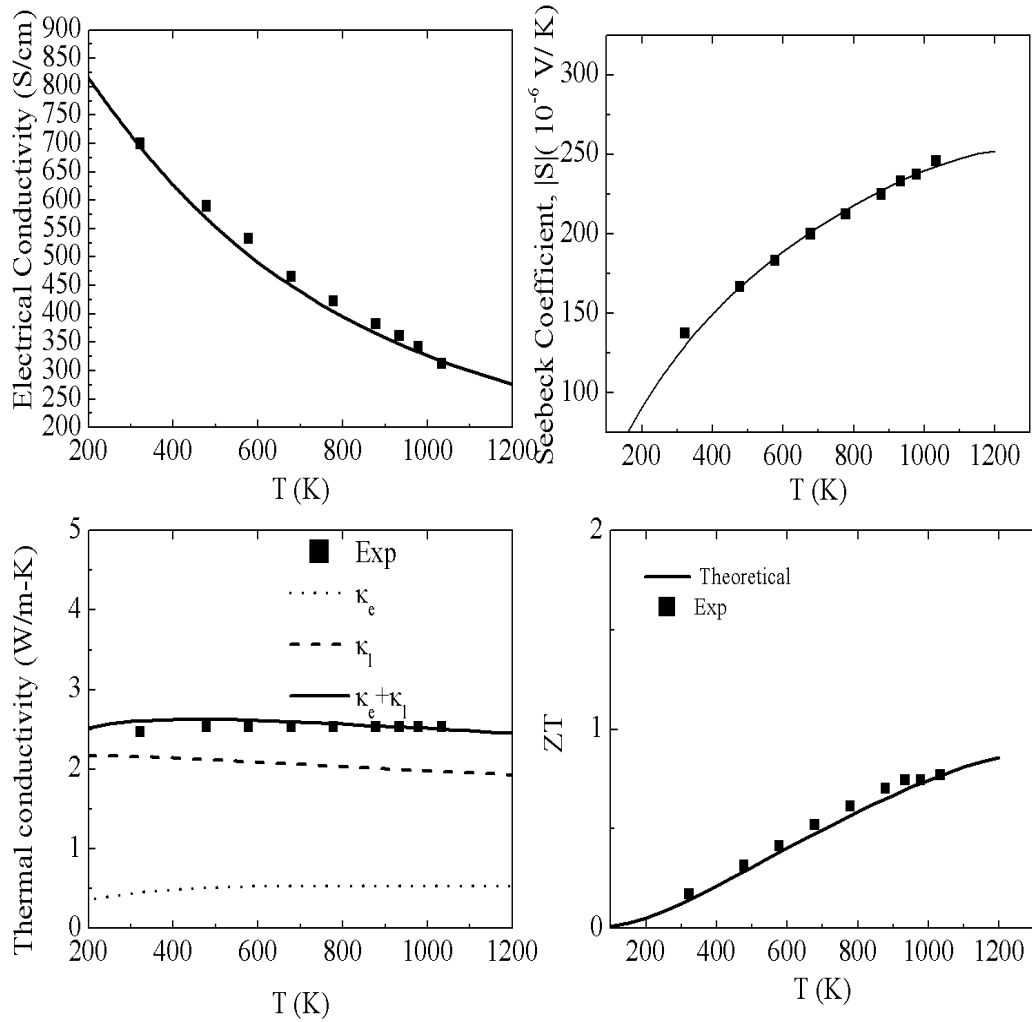


Figure 4.15: (A) Seebeck coefficient of sintered nanostructured p-type $Si_{0.8}Ge_{0.2}$ with grain size 20 nm. Experimental points are from Ref.[116]. (B) Electrical conductivity. (C) Electronic thermal conductivity, lattice conductivity and total thermal conductivity, (D) Figure of merit, ZT .

4.4.3 Characterization and Modelling of larger grain sintered materials

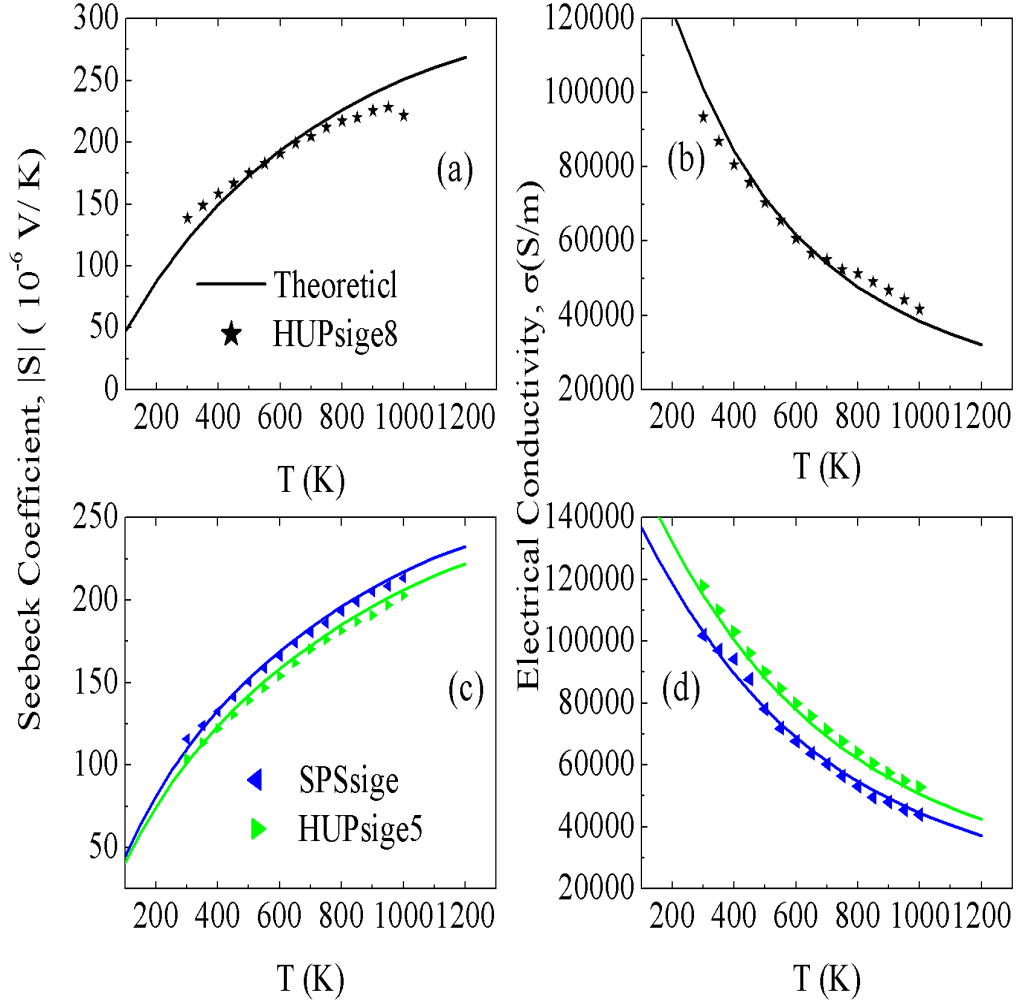


Figure 4.16: (a) Seebeck coefficient of sintered ntype $Si_{0.8}Ge_{0.2}$ reported in this article, (b) Electrical conductivity. (c) Seebeck coefficient of of sintered ptype $Si_{0.8}Ge_{0.2}$ reported in this article, (d) Electrical conductivity.

We measured thermal diffusivity, specific heat, Seebeck coefficient and electrical conductivity of sintered $Si_{0.8}Ge_{0.2}$ at high temperature. $Si_{0.8}Ge_{0.2}$ sample was fabricated by ball milling and hot-pressing procedure by our collaborators and the measurement

of Seebeck coefficient and electrical conductivity also have been done by our collaborators. The experimental results of the thermal conductivity was discussed in detail in the previous section. Here in Fig.4.16 we have presented the experimental results of Seebeck coefficient and electrical conductivity of these samples with the theoretical model.

The doping level for the ntype material is $2.2 \times 10^{20} \text{ cm}^{-3}$ and grain size is 80nm and for the ptype material doping levels are $2.5 \times 10^{20} \text{ cm}^{-3}$ and $2.9 \times 10^{20} \text{ cm}^{-3}$ and the grain size is 40 nm.

The measured thermal conductivity is shown in Fig.4.17. The grain boundary phonon transparency used in the theoretical curve is the same as for the nanograined case above, i.e. $B_1 = 20$.

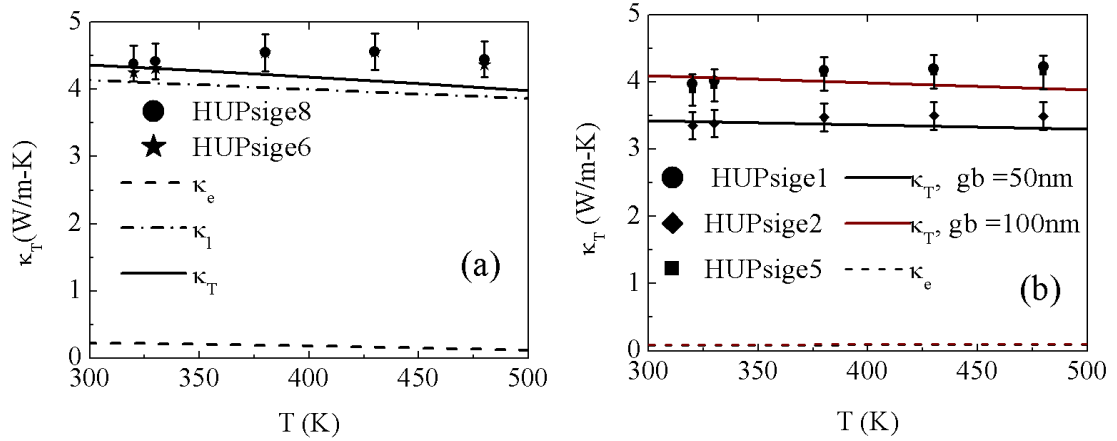


Figure 4.17: (a) Thermal conductivity of of sintered ntype $\text{Si}_{0.8}\text{Ge}_{0.2}$ reported in this article, (b) Thermal conductivity of of sintered ptype $\text{Si}_{0.8}\text{Ge}_{0.2}$ reported in this article.

Thus, it is clear from these result that as the grain size is large, thermal conductivity was not reduced much by the grain boundary scattering of phonons.

Sample	Type	n ($10^{19}cm^{-3}$)	μ (cm^2/Vs)	σ (S/m)	S ($\mu V/K$)	κ ($W/m - K$)	ZT
HUPsige1	p	2.88	194	8.94×10^4	103	3.47	0.109
HUPsige2	p	2.94	230	1.08×10^5	87	4.12	0.079
HUPsige5	p	13.8	50.1	1.1×10^5	95	4.17	0.095
SPSsige	p	22		9.8×10^5	115.67	4.13	0.1
HUPsige6	n	16.7	37.2	9.94×10^4	-105	4.54	0.096
HUPsige8	n	3.89	154	9.57×10^4	-140	4.461	0.168

Table 4.2: Summary of the thermoelectric properties of sintered $Si_{0.8}Ge_{0.2}$ at room temperature.

4.4.4 The potential for further ZT improvement in nanograined SiGe

We now address the question of whether ZT is likely to be improved in nanograined SiGe, beyond the values already demonstrated in Refs.[136]. First of all we will discuss whether, keeping the same kind of grain boundary structure, ZT could be still improved by fine tuning the doping level. A very clear pictorial way to do this is to represent experimental results together with theoretical ones in a modified 'Jonker' plot. This means plotting the Seebeck coefficient as a function of the ratio of electrical and thermal conductivities, i.e. S versus σ/κ , for samples of different doping concentrations. (The standard Jonker plot is just S versus σ .) In the same graph, we also represent curves of constant ZT . It is then easy to locate the best optimized sample by finding the point along the $S(\sigma/\kappa)$ curve that is tangent to the iso- ZT curve.

As we had mentioned above that for the SiGe alloy in degenerate case the ionized impurity play a important role in the transport properties, in our theoretical calculation for the alloy materials we had changed the compensation ratio of the ionized impurity. The compensation ratio was defined as,[138] the ratio of

$$\text{concentration of fixed ionized centers/concentration of mobile charges} = \frac{N^+ + N^-}{n+p}.$$

For ntype materials where free-hole concentration, p is negligible and for the ptype where free-electron concentration, n is negligible it becomes unity. For the mobility calculation in Fig.4.10 and thermoelectric properties calculation, we had used the compensation ratio as 2 which modified the ionized impurity scattering rate in these highly doped materials. This is considerable because for these highly doped materials, the validity of the Born approximation is questionable. With these approximations the electrical conductivity and Seebeck coefficient and the electronic thermal conductivity of the bulk $Si_{0.8}Ge_{0.2}$ are plotted in Fig.4.12 and introducing a grain boundary

scattering proportional to the grain size, we had calculated the thermoelectric properties of nanostructured $Si_{0.8}Ge_{0.2}$ (See Fig.4.14). From Fig.4.18 it was understood that we can achieve an optimum ZT by choosing the proper doping concentration.

In Fig.4.18, we represent the modified Jonker's plot for different grain size at 400K. Here the Seebeck coefficient of ntype and ptype are plotted in opposite sign.

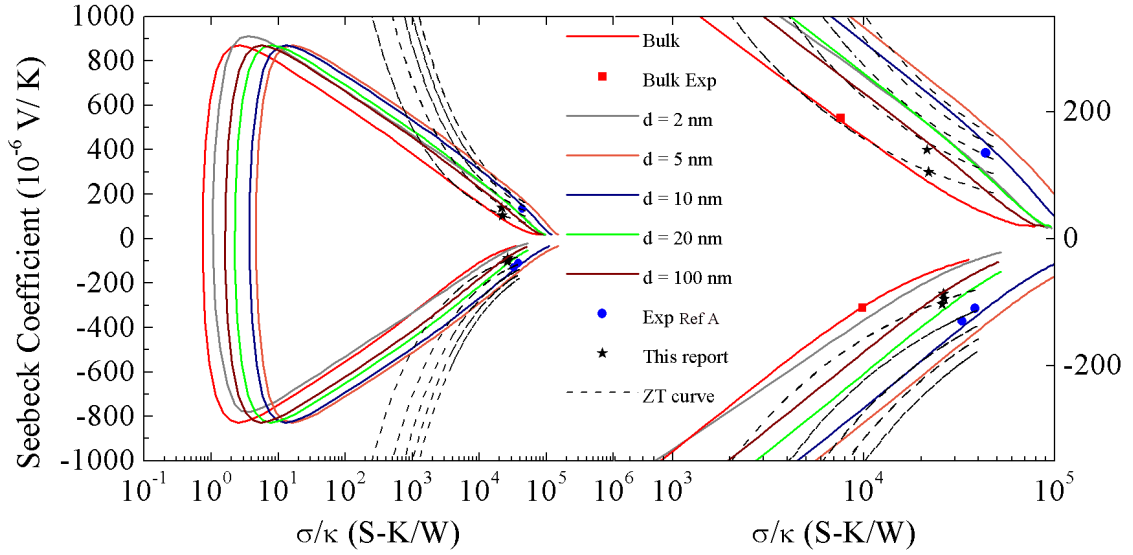


Figure 4.18: Seebeck coefficient Vs (electrical conductivity/ thermal conductivity) for different grain sized at 400K. Black lines are the constant ZT curve at 0.1, 0.2, 0.3, 0.4 and 0.5. Ref A is [116, 117].

From Fig.4.18 it is clearly understood that the we can achieve an optimum ZT by choosing the proper doping concentration on which the $\frac{\sigma}{\kappa_{total}}$ depends. By varying doping concentration for different grain size we can improve the ZT values at a particular temperature. Where the dots are the experimental points and moving these point from right to left, we can have better ZT values. We can see that at 400K temperature, some slight ZT enhancement can be achieved using slightly reduced doping levels. The theoretical optimized values for the transport parameters are $S = 202.28\mu V/K$, $\sigma = 612.5S/cm$, $\kappa = 2.3W/m - K$ for the n-type, and $163.3\mu V/K$, $536.65S/cm$, $2.35W/m - K$ for the p-type material with grain sizes $12nm$ and $20nm$ respectively. Furthermore, if slightly smaller grains are used, ZT could be enhanced a bit more, up to about 0.5.

For the modified jonker's plot of high temperature (1000K), it is also clearly

noticed that the further improvement of the ZT is possible by only changing the doping concentration.

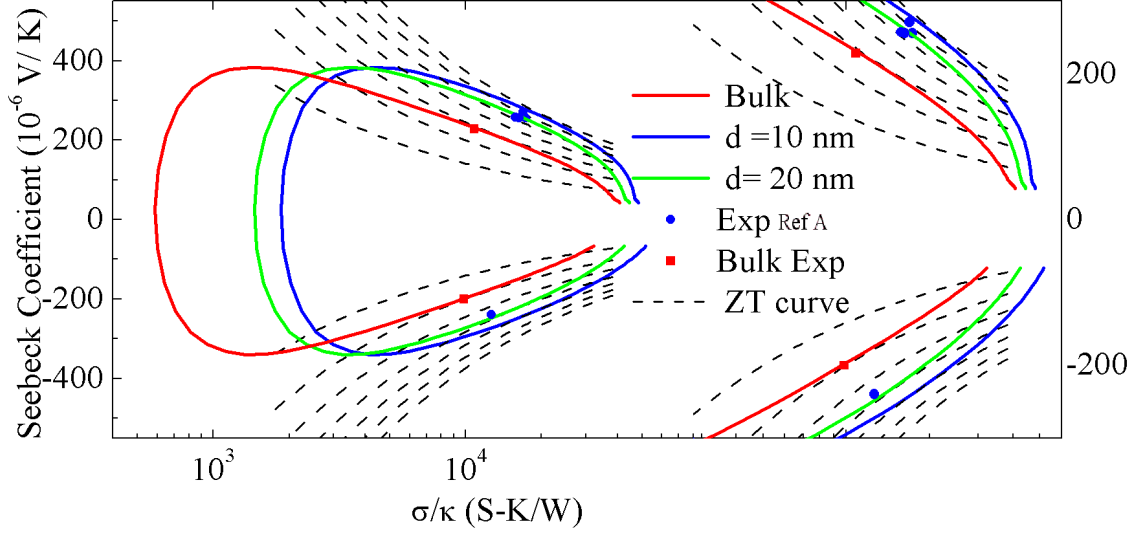


Figure 4.19: Seebeck coefficient Vs (electrical conductivity/ thermal conductivity) for different grain size at 1000K. Black lines are the ZT curve at 0.4, 0.6, 0.8 and 1.0, 1.2 and 1.4.

The exact enhancement of the ZT values for different temperature is given in the Fig.4.21 (for ntype) and the Fig.4.22 (for the ptype).

At a temperature of 1000K the samples are essentially at the optimum point on the plot, and a different doping level at the same grain size would only reduce ZT . However, reducing the grain size and simultaneously adjusting the doping would further increase ZT . Within the simple description of electron grain boundary scattering employed, we expect that ZT would continue to improve up to grain sizes around 5 nm, potentially reaching $ZT = 0.5$ at 400K. When the grain size becomes smaller than the mean free path of the electron ZT starts decreasing.

In the Fig.4.20, ZT values of ntype $Si_{0.8}Ge_{0.2}$ is given at grain size 10 nm for three different temperature for different carrier concentrations.

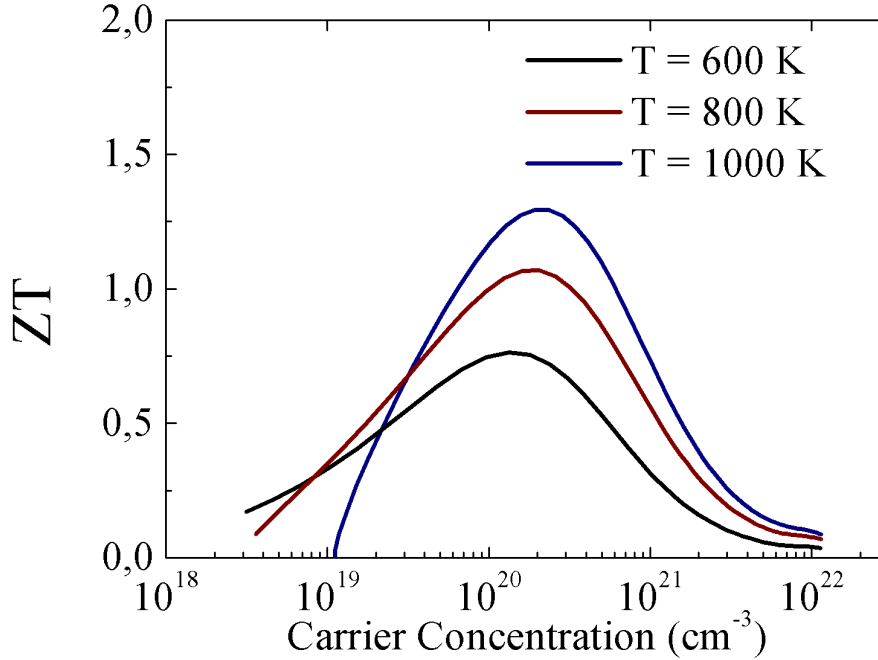


Figure 4.20: ZT for different carrier concentration at 600K, 800K and 1000K at grain size 10 nm.

For degenerate materials ZT depends very much on the doping level of impurity. In Fig.4.21 we have presented the ZT for the bulk sintered materials, ZT values of our sintered sample and the ZT values of the nanostructured samples with the grain size 12 nm. We can still optimize the ZT values of nanograin materials at 12 nm grain size by optimizing its doping level at all temperature. Our calculations suggests that further optimization of current state of the art ntype (ptype) material could possibly lead to $\sim 6\%$ (5%) ZT enhancement at 1000K and 25% (4%) at room temperature. Even larger enhancements should be possible if the phonon scattering probability of the grain boundaries could be increased beyond its present value of 10% . In the previous section we saw that the grain boundaries are quite transparent to phonons, a fact that had also been pointed out in ref.[136]. Roughly, a phonon needs to traverse about 10 grain boundary interfaces in order to experience a diffusive scattering event. In principle one could envisage nano grains with rougher boundaries, which would scatter phonons more efficiently. A plausible limit to the degree of diffusivity of the interface is that of the diffuse mismatch model. In this model, every time a phonon

reaches a grain boundary it loses memory and it is randomly scattered. The result is a phonon mean free path equal to the grain size. Thus for a totally diffusive grain boundary, the phonon mfp would be one order of magnitude smaller than for the state of the art nanograined SiGe. The calculated result for such diffusive grain boundaries yield an available ZT of 2 for ntype, or 1.5 for ptype material at 1000K, i.e. more than 30% increase over the so far demonstrated values. It is questionable whether the grain boundary roughness can be increased without simultaneously creating charge traps for the electrons. Interfacial charge trapping could have catastrophic effects on the electrical conductivity, by creating large potential barriers for electrons. To avoid this, it is probably important to minimize the formation of defects and dislocations. A step in this direction has been recently demonstrated in Ref.[147, 148], where well defined fully diffusive phonon barriers were fabricated in a single crystalline Si/SiGe system. We believe that a direction for further improvement of sintered nano grain thermoelectric materials may be through the development of techniques that can effectively enhance the phonon diffusivity of the grain boundaries, possibly through the introduction of well lattice matched secondary phases, such as embedded nanoparticles, at the interfaces between grains.

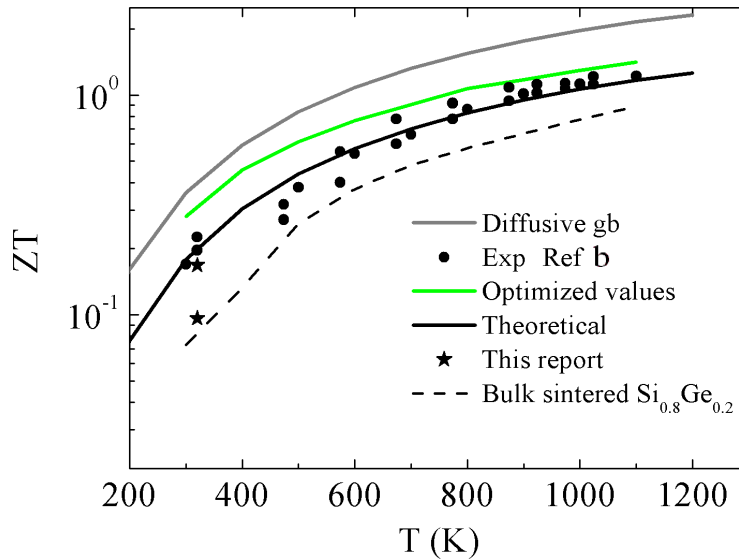


Figure 4.21: Comparison between ZT of different sintered ntype $Si_{0.8}Ge_{0.2}$. Ref b is [117].

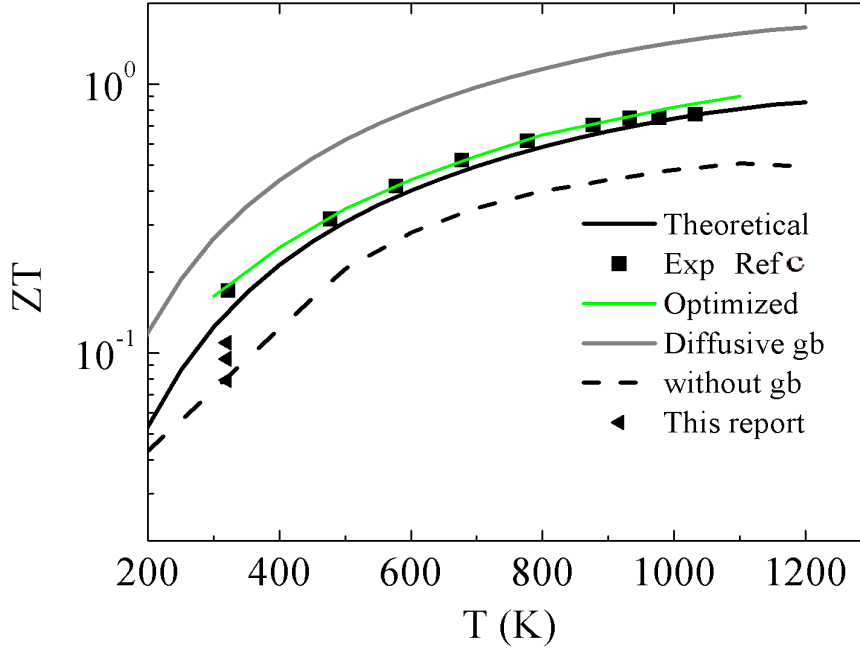


Figure 4.22: Comparison between ZT of different sintered $Si_{0.8}Ge_{0.2}$. Ref c is [116].

From the Fig.4.18 it is also clear that when grain size becomes comparable to the mean free path (m.f.p) of the electron(5 nm) we achieve the maximum ZT . When the grain size became much smaller than the m.f.p of the electron ZT start decreasing. In this case Boltzmann transport equation may also not be satisfied [149].

4.5 Conclusion

1. In this Chapter we have presented a theoretical model for the thermoelectric properties of $SiGe$ nanocomposite materials. In our theoretical model we implemented different types of scattering mechanisms for both electrons and phonons scattering.
2. By analyzing the experimental results of the sintered materials fabricated by the ball milling and hot pressing technique we have understood that we can improve ZT by optimizing grain size and doping concentration. Further optimization of

the ZT could be possible if phonon scattering by grain boundaries could be made to reach the phonon diffuse mismatch limit.

3. Finally, we have seen that the nanostructuring also reduced the electrical conductivity of the materials. So the power factor of the nano structure materials also decreased with the thermal conductivity reduction.

Chapter 5

Conclusions and Future Work

Contents

5.1	Conclusions	101
5.2	Future Direction	103

5.1 Conclusions

The physics of the heat and charge carrier transport in nanocomposites is only partially understood. A more complete understanding is required in designing and improving the performance of a wide variety of devices and materials including microelectronics, thermoelectrics, heat spreaders, thermal insulators, and composites. This dissertation presents a better insight in the heat and charge transport mechanisms across the nanostructured materials.

In Chapter 2, thermal properties of porous alloy and non-alloy materials are calculated by measuring effective mean free path in these materials by a numerical and an analytical method. We found that thermal conductivity of the porous alloy is much more affected by the pore radius of $100nm$ compare to the non-alloy materials at room temperature. Where for the non-alloy materials decrease in the thermal conductivity started after the pore size $100nm$, in the alloy materials we have obtained the reduction for much larger pore radius. Without pores thermal conductivity of $Si_{0.5}Ge_{0.5}$ is one order of magnitude smaller than the pure Si and Ge thermal conductivity. With pores this difference becomes 2 order of magnitude at pore radius $1000nm$ for 60% porosity and at pore radius $100nm$ for 10% porosity. This study on the porous materials explain the pore radius effect in thermal conductivity more clearly and we have understood the proper dependencies of the conductivity on the pore radius, interpore distances, and porosity. This model also modified the previous model based on the simple cylindrical boundary geometry approximation. Also from the analytical model, we can calculate the porous materials thermal conductivity for any porosity and pore radius very efficiently and quickly.

In Chapter 3 of this dissertation, we have presented a study of heat transport in nanowires. Experimental thermal conductance of a straight and bent nanowires are strikingly much low than their ballistic conductance. For a $200 \times 100nm^2$ Si nanowire, the ballistic thermal conduction would be like $124 \times 4\sigma_0$ at temperature $5K$. The measured thermal conductivity is 40 times smaller than the ballistic thermal conductance and introducing double kink in the straight wire further reduced the thermal conductance by 40%. This large reduction in the thermal conductance is not clearly proven by the Casimir's model. To properly understand the physics behind this reduction, we have performed a simple MC simulation of phonon transmittivity in the straight and bent nanowires. We indeed found that for the bent junction there will be 60% reduction in the phonon transport compared to the straight wire with total specular reflections. When the surface starts to become diffusive this difference also decreases and in the totally diffusive region this difference is very small. Though only this back scattering for the bent junction does not enough to explain this high reduction in thermal conductivity. We further consider that transverse phonon mode contribution to the thermal conductance was diminished by an interface between wire and thermostat. With this additional assumption, we can exactly explain the experimental results.

In Chapter 4, the effect of grain size on the overall thermoelectric properties of nanocomposites were studied. Thermoelectric properties of nanograined *SiGe* alloy were calculated using a theoretical model. From this model, we can predict the maximum ZT of the materials for a particular temperature. This model includes all the scattering mechanisms for electrons and phonons. We have obtained very good agreement between the theoretical calculations and the experimental results of the mobility, the electrical conductivity and the Seebeck coefficient of the $Si_{0.8}Ge_{0.2}$ alloy. This model predicts that further optimization can be possible by optimizing the doping level and the grain size. From the model, it is evident that thermoelectric properties of the alloy can be improved until the grain size becomes comparable to the electron mean free path ($5nm$ for the SiGe alloy) because the electronic transport is not affected largely by the grain size above this diameter. If we further reduce the grain size, it strongly affected the electronic transport and reduce the ZT . To sum up, optimization of current state of the art ntype (ptype) material would be feasible by optimizing doping level and grain size, leading to $\sim 6\%$ (5%) ZT enhancement at $1000K$ and 25% (4%) at room temperature. More interestingly, we have shown that further reduction in the thermal conductivity is possible considering complete diffusive grain boundary. This modification can increase the ZT almost 2 times for the ntype and ptype SiGe alloys at $1200K$. This could be possible by engineering the synthesis of the nanograined composite materials.

5.2 Future Direction

There are several issues that future work in this area should address. One vital issue is determining the thermal conductivity of the porous alloy experimentally with different pore radius, which will establish the theory of the calculation in Chapter 2. More experimental measurements and theoretical calculations are required for the thermal conductivity of nanoporous and nanocomposites materials with quantum dots or tubes inside bulk or superlattices to understand more evidently the size effect of dots or pores or wires in the composite. It is very much challenging to prepare and measure the conductivity of these types of structures. Though recently there are lot of improvement on the measurement technique on nanoscale, some new techniques such as 3ω method, time-domain thermoreflectance (TDTR) method, scanning thermal microscopy (SThM), Laser flash technique are providing more accurate measurements on nanoscale. More detailed model on the phonon transport of the composite materials and the detailed understanding of the scattering mechanisms responsible for reducing the thermal conductivity is necessary for further improvements of the materials.

Similarly, phonon transport in nanowires also required more details investigation. Surface and structure of the nanowires affected the phonon transport very much in the low temperature range. Again both growth condition and temperature affected the quality of the surface. So different growth techniques need to be investigated in more details. It is also not clearly understood how the frequency dependencies of the contact and structure modifies the resistance of nanowires. Further investigation should be done on these to have a clear knowledge on the phonon transport in nanowires. In future that could help to make nanowires, which can also be useful in the application at high temperatures and these could also enhance the properties of the nanowires.

Finally, applications of the TE materials in power generator that directly convert heat to electricity, or refrigeration devices that use electricity to pump heat from cold to hot, need to include improved figure of merit, ZT to achieve more efficient devices. Currently the best thermoelectric materials are the alloys of antimony and bismuth tellurides with some other doping elements which show the ZT reaching 1 at room temperature. TE coolers with ZT of 1 operate at only 10% of Carnot efficiency. Some 30% of Carnot efficiency (comparable to home refrigeration) could be reached by a device with a ZT of only 4. Increasing ZT by a factor of 4 has remained a formidable challenge.

There are lot of research going on to achieve a better ZT and to optimize the devices. Though we understood from Chapter 4 that by reducing lattice thermal conductivity on the alloy or by optimizing the doping level we could increase the ZT . Another way for this may be increasing the electronic power factor of the materi-

als. In this direction some model proposed "Phonon blocking/Electron transmitting Structure" [5, 42] to block the phonon without affecting the electrical resistance. The other possible ways to increase the ZT could be (a) a high symmetry crystal structure (high number of degeneracies of band extrema near Fermi level) which would increase the power factor, with a large number of heavy elements per unit cell which will decrease lattice conductivity (b) small electronegativity differences between the elements in the compound which will higher the mobility or increase the scattering time, (c) at least one high effective mass. This list of needs remains daunting, because the structure of most new materials cannot be predicted. Recent advanced in determining the electronic band structure based on the density functional theory [150] gives some details about the TE material properties. More detailed understanding of the crystal structure is necessary to understand properly the energy band diagram of the complex materials which could give the knowledge about the band structure parameters and the ability to produce TE materials which will generate maximum efficiency.

Appendix A

Appendix

Mathematica code for MC Simulation of MFP for CGA with a cylinder pore Function definition

This function generates a random free path:

```
RandLamb:=-Log[Random[]]
```

This function generates a random direction 3D unit vector:

```
RandVel:=#/ &@{Random[Real,{-1.,1.}],  
Random[Real,{-1.,1.}],Random[Real,{-1.,1.}]}
```

This function generates a random 2D starting point, bound between inner (rin) and outer (rout) radius

```
RandX[rin_, rout_] :=  
Module[{rm}, If[rin >= rout, Abort[]];  
rm = {Random[Real, {-rout, rout}], Random[Real, {-rout, rout}]};  
While[Sqrt[rm.rm] < rin || Sqrt[rm.rm] > rout,  
rm = {Random[Real, {-rout, rout}], Random[Real, {-rout, rout}]};  
rm]
```

**Full program, using the slope method
(*Results for different diameters*)**

```
Timing[flxwdiam = {}];  
Do[systemlength =.; {rout, rin} = {1., Sqrt[0.4]}*10.^idiam;  
endcty = {}];  
Do[convergence = 1; systemlength = 10.^sysl; nrefl = 0;  
nthrough = 0;
```

```

Do[newx = RandX[rin, rout]~Join~{0.};
  lamb = RandLamb;
  newv = {#[[1]], #[[2]], Abs#[[3]]} &[RandVel]; ii = 0;
  Do[x = newx; v = newv; xp = x + lamb*v;
    x2d = x[{{1, 2}}]; xp2d = xp[{{1, 2}}];
    v2d = #/Sqrt[#.#] &[v[{{1, 2}}]];
    wunit = v2d; yunit = {v2d[[2]], -v2d[[1]]};
    y = (x2d.yunit) yunit;
    w = (x2d.wunit) wunit;
    case = .;
    If[Norm[y] <= rin &&
      v2d.x2d < 0. && (Norm[xp2d] < rin || v2d.xp2d > 0.), (case =
        1; rimpacted = rin; signroot = -1),
      If[Norm[xp2d] >= rout, (case = 2; rimpacted = rout;
        signroot = 1), case = 3]];
    If[case == 3, r = xp2d,
      r = y + signroot Sqrt[rimpacted^2 - y.y] wunit];
    phi = #/Sqrt[#.#] &[{r[[2]], -r[[1]]}];
    runit = #/Sqrt[#.#] &[r];
    If[case == 2, newv2d = -(v2d.runit) runit + (v2d.phi) phi;
      newv = Join[newv2d*Norm[v[{{1, 2}}]], {v[[3]]}],
      newv = RandVel];
    newx =
      Join[r, {x[[3]] + (xp[[3]] - x[[3]])*
        Norm[r - x2d]/Norm[xp2d - x2d}]];
    If[case == 2, lamb = lamb - Norm[newx - x], lamb = RandLamb];
    ii++;
    If[newx[[3]] < 0., Return[{ii, nrefl++}]];
    If[newx[[3]] > systemlength, Return[{ii, nthrough++}]];
    If[iconv == 50000, convergence = 0], {iconv,
      50000}], {numphonons = 50000}];
  Print["convergence=", convergence].Print[nrefl, " ", nthrough,
    " ", systemlength*nthrough/numphonons // N, " ",
    numphonons/nthrough // N];
  AppendTo[
    cndcty, {systemlength, systemlength*nthrough/numphonons // N,
      numphonons/nthrough // N}], {sysl, -0.2, .5, .7}];
  AppendTo[

```

```
flxwdiam, {rout, #[[1]]/#[[3]] &@(cndcty[[-1]] -
  cndcty[[1]])}, {idiam, -2, 2, 0.2}]]];
```

Mathematica code for MC Simulation of MFP for periodic square boundary with a cylinder pore Function definition

This function generates a random free path:

```
RandLamb:=-Log[Random[]]
```

This function generates a random direction 3D unit vector:

```
RandVel:=#/ &@{Random[Real,{-1.,1.}],
  Random[Real,{-1.,1.}],Random[Real,{-1.,1.}]}
```

This function generates a random 2D starting point, bound between inner (rin) and outer (rout) radius

```
RandX[rin_,rout_]:=Module[{rm},If[rin \geq rout,Abort[]];
  rm={Random[Real,{-rout,rout}],Random[Real,{-rout,rout}]};
  While[<rin,rm={Random[Real,{-rout,rout}],Random[Real,{-rout,rout}]}];rm]
```

**Full program, using the slope method
(*Results for different diameters*)**

```
Timing[flxwdiam = {}];
  Do[systemlength =.; {rout, rin} = {1., 2*Sqrt[0.4/\[Pi]]}*10.^idiam;
    cndcty = {}];
  Do[convergence = 1; systemlength = 10.^sysl; nrefl = 0;
    nthrough = 0;
    Do[newx = RandX[rin, rout]~Join~{0.};
      lamb = RandLamb;
      newv = {#[[1]], #[[2]], Abs[#[[3]]]} &[RandVel]; ii = 0;
      Do[x = newx; v = newv; xp = lamb*v + x;
        x2d = x[{{1, 2}}]; xp2d = xp[{{1, 2}}];
        v2d = #/Sqrt[#.#] &[v[{{1, 2}}]];
        wunit = v2d; yunit = {v2d[[2]], -v2d[[1]]};
          y = (x2d.yunit) yunit;
          w = (x2d.wunit) wunit;
```

```

A = (xp2d[[2]] - x2d[[2]])/(xp2d[[1]] - x2d[[1]]);
xr1 = ((rout - x2d[[2]])/A) + x2d[[1]];
yr1 = rout;
xr2 = rout;
yr2 = x2d[[2]] + ((rout - x2d[[1]])*A);
xr3 = ((-rout - x2d[[2]])/A) + x2d[[1]];
yr3 = -rout;
xr4 = -rout;
yr4 = x[[2]] + ((-rout - x2d[[1]])*A);
d[1] = {xr1, yr1};
d[2] = {xr2, yr2};
d[3] = {xr3, yr3};
d[4] = {xr4, yr4};
case = .;
If[Norm[y] <= rin &&
  v2d.x2d <
  0. && (Norm[xp2d] \[LessSlantEqual] rin ||
  v2d.xp2d > 0.), (r = y - Sqrt[rin^2 - y.y] wunit;
  rf = y - Sqrt[rin^2 - y.y] wunit; newv = RandVel;
  case = "InnerCollision"),
If[(xp2d[[1]] >=
  rout) || (xp2d[[1]] <= -rout) || (xp2d[[2]] >=
  rout) || (xp2d[[2]] <= -rout), case = "OuterCollision";
Linepoint = {};
Do[If[(d[i] - x2d).v2d >= 0 && (d[i] - x2d).(d[i] - x2d) !=
  0.0, AppendTo[Linepoint, {d[i], i}], {i, 4}];
newLinepoint =
  Sort[Linepoint, (#1[[1]] - x2d).(#1[[1]] - x2d) <= (#2[[1]] -
  x2d).(#2[[1]] - x2d) &];
If[(newLinepoint[[1, 2]] == 1) || (newLinepoint[[1, 2]] ==
  3), (r = {newLinepoint[[1, 1]][[
  1]], -newLinepoint[[1, 1]][[2]]};
  rf = newLinepoint[[1, 1]]),
If[(newLinepoint[[1, 2]] == 2) || (newLinepoint[[1, 2]] ==
  4), (r = {-newLinepoint[[1, 1]][[1]],
  newLinepoint[[1, 1]][[2]]}); rf = newLinepoint[[1, 1]]],
(case = "BulkCollision"; r = xp2d; rf = xp2d;
  newv = RandVel)];

```

```

newx1 =
  Join[rf, {x[[3]] + (xp[[3]] - x[[3]])*
    Norm[rf - x2d]/Norm[xp2d - x2d}}];
newx = Join[
  r, {x[[3]] + (xp[[3]] - x[[3]])*
    Norm[rf - x2d]/Norm[xp2d - x2d}}];
If[case == "OuterCollision", lamb = lamb - Norm[newx1 - x],
  lamb = RandLamb]; ii++;
If[newx[[3]] < 0., Return[{ii, nrefl++}]];
If[newx[[3]] > systemlength, Return[{ii, nthrough++}]];
If[iconv == 90000, convergence = 0], {iconv,
  90000}], {numphonons = 30000}];
Print["convergence=", convergence].Print[nrefl, " ", nthrough,
  " ", systemlength*nthrough/numphonons // N, " ",
  numphonons/nthrough // N];
AppendTo[
  cndcty, {systemlength, systemlength*nthrough/numphonons // N,
  numphonons/nthrough // N}], {sysl, -0.2, 0.4, 0.6}];
AppendTo[
  flxwdiam, {rout, #[[1]]/#[[3]] &@(cndcty[[-1]] -
  cndcty[[1]])}], {idiam, -2, 2, 0.2}]];

```

Bibliography

- [1] A.N. Goldstein, C.M. Echer, and A.P. Alivisatos. Melting in semiconductor nanocrystals. *Science*, 256(5062):1425–1427, 1992.
- [2] S.H. Tolbert and A.P. Alivisatos. High-pressure structural transformations in semiconductor nanocrystals. *Annual Review of Physical Chemistry*, 46(1):595–625, 1995.
- [3] R. Goswami, S. Banerjee, K. Chattopadhyay, and A. K. Raychaudhuri. Superconductivity in rapidly quenched metallic systems with nanoscale structure. *Journal of Applied Physics*, 73(6):2934, 1993.
- [4] F. Einar Kruis, Heinz Fissan, and Aaron Peled. Synthesis of nanoparticles in the gas phase for electronic, optical and magnetic applications—a review. *Journal of Aerosol Science*, 29(5-6):511–535, June 1998.
- [5] Francis J. DiSalvo. Thermoelectric cooling and power generation. *Science*, 285(5428):703–706, July 1999.
- [6] M. S. Dresselhaus, G. Chen, M. Y. Tang, R. G. Yang, H. Lee, D. Z. Wang, Z. F. Ren, J.-P. Fleurial, and P. Gogna. New directions for Low-Dimensional thermoelectric materials. *Advanced Materials*, 19(8):1043–1053, 2007.
- [7] F.D. Rosi. Thermoelectricity and thermoelectric power generation. *Solid-State Electronics*, 11(9):833–848, IN1–IN2, 849–868, September 1968.
- [8] G. Jeffrey Snyder and Eric S. Toberer. Complex thermoelectric materials. *Nat Mater*, 7(2):105–114, February 2008.
- [9] John W Fairbanks. Vehicular thermoelectric applications session DEER 2009, 2009.

-
- [10] L. D. Hicks and M. S. Dresselhaus. Effect of quantum-well structures on the thermoelectric figure of merit. *Physical Review B*, 47(19):12727, May 1993.
- [11] L. D. Hicks, T. C. Harman, and M. S. Dresselhaus. Use of quantum-well superlattices to obtain a high figure of merit from nonconventional thermoelectric materials. *Applied Physics Letters*, 63(23):3230, 1993.
- [12] L. D. Hicks and M. S. Dresselhaus. Thermoelectric figure of merit of a one-dimensional conductor. *Physical Review B*, 47(24):16631, June 1993.
- [13] D. G. Cahill, S. K. Watson, and R. O. Pohl. Lower limit to thermal conductivity of disordered crystals. *Phys. Rev. B*, 46:6131–40, 1992.
- [14] Neil W. Ashcroft and N. David Mermin. *Solid state physics*. Holt, Rinehart and Winston, 1976.
- [15] B. R. Nag. *Theory of electrical transport in semiconductors*. Pergamon Press, 1972.
- [16] Energy bands. http://ecee.colorado.edu/~bart/ecen3320/newbook/chapter2/ch2_3.htm.
- [17] Richard M. Martin. *Electronic structure: basic theory and practical methods*. Cambridge University Press, April 2004.
- [18] J. M. Ziman. *Electrons and phonons*. Clarendon Press, 2001.
- [19] Riccardo Tubino. Lattice dynamics and spectroscopic properties by a valence force potential of diamondlike crystals: C, si, ge, and sn. *The Journal of Chemical Physics*, 56(3):1022, 1972.
- [20] Charles Kittel and Herbert Kroemer. *Thermal physics*. W. H. Freeman, 1980.
- [21] David Lacroix, Karl Joulain, and Denis Lemonnier. Monte carlo transient phonon transport in silicon and germanium at nanoscales. *Physical Review B*, 72(6), 2005.
- [22] Scott Thomas Huxtable. *Heat transport in superlattices and nanowire arrays*. University of California, Berkeley, 2002.
- [23] C. M. Bhandari. *CRC handbook of thermoelectrics*, 1995.
- [24] George S. Nolas, Jeffrey Sharp, and H. J. Goldsmid. *Thermoelectrics: basic principles and new materials developments*. Springer, 2001.
- [25] William Jones and Norman Henry March. *Theoretical solid state physics*. Wiley-Interscience, 1973.

-
- [26] Jasprit Singh. *Physics of semiconductors and their heterostructures*. McGraw-Hill, 1993.
- [27] D.L. Rode, R.K. Willardson, and Albert C. Beer. Chapter 1 Low-Field electron transport. volume Volume 10, pages 1–89. Elsevier, 1975.
- [28] S. Volz (Ed.). Micro and nanoscale heat transfer. *Springer*, 2005.
- [29] V. P. Carey, G. Chen, C. Grigoropoulos, M. Kaviani, and A. Majumdar. A review of heat transfer physics. *Nanoscale and Microscale Thermophysical Engineering*, 12(1):1, 2008.
- [30] David G. Cahill, Wayne K. Ford, Kenneth E. Goodson, Gerald D. Mahan, Arun Majumdar, Humphrey J. Maris, Roberto Merlin, and Simon R. Phillpot. Nanoscale thermal transport. *Journal of Applied Physics*, 93(2):793, 2003.
- [31] G. Q. Lu. Nanoporous Materials-An overview. *Nanoporous materials: science and engineering*, page 1, 2004.
- [32] N. Chen. Macroscopic thermoelectric inhomogeneities in $(\text{AgSbTe}_2)_x(\text{PbTe})_{1-x}$. *App. Phys. Lett.*, 87:171903, 2005.
- [33] David Michaël Rowe. *Thermoelectrics handbook: macro to nano*. CRC Press, 2006.
- [34] Terry M. Tritt. *Thermoelectric materials: new directions and approaches : symposium held March 31-April 3, 1997, San Francisco, California, USA*. Materials Research Society, 1997.
- [35] Milton Ohring. *The materials science of thin films: deposition and structure*. Academic Press, 2002.
- [36] Guozhong Cao. *Nanostructures & Nanomaterials: Synthesis, Properties & Applications*. Imperial College Press, 1 edition, April 2004.
- [37] Carlo Jacoboni and Lino Reggiani. The monte carlo method for the solution of charge transport in semiconductors with applications to covalent materials. *Reviews of Modern Physics*, 55(3):645, July 1983.
- [38] Leo Esaki. The evolution of nanoscale quantum effects in semiconductor physics. *Nanostructured Materials*, 12(1-4):1–8, 1999.
- [39] Paul Alivisatos. The use of nanocrystals in biological detection. *Nat Biotech*, 22(1):47–52, January 2004.

-
- [40] Ravi Prasher. Transverse thermal conductivity of porous materials made from aligned nano- and microcylindrical pores. *Journal of Applied Physics*, 100(6):064302, 2006.
- [41] Sebastian Volz. *Thermal Nanosystems and Nanomaterials*. Springer, 2010.
- [42] Rama Venkatasubramanian, Edward Siivola, Thomas Colpitts, and Brooks O’Quinn. Thin-film thermoelectric devices with high room-temperature figures of merit. *Nature*, 413(6856):597–602, October 2001.
- [43] Allon I. Hochbaum, Renkun Chen, Raul Diaz Delgado, Wenjie Liang, Erik C. Garnett, Mark Najarian, Arun Majumdar, and Peidong Yang. Enhanced thermoelectric performance of rough silicon nanowires. *Nature*, 451(7175):163–167, January 2008.
- [44] T. C. Harman, P. J. Taylor, M. P. Walsh, and B. E. LaForge. Quantum dot superlattice thermoelectric materials and devices. *Science*, 297(5590):2229–2232, September 2002.
- [45] H. S. Carslaw and J. C. Jaeger. *Conduction of heat in solids*. Clarendon, 1984.
- [46] A. Majumdar. Microscale heat conduction in dielectric thin films. *Journal of Heat Transfer*, 115(1):7–16, February 1993.
- [47] Ryōgo Kubo, Morikazu Toda, and Natsuki Hashitsume. *Statistical physics II: nonequilibrium statistical mechanics*. Springer, 1985.
- [48] Sandip Mazumder and Arunava Majumdar. Monte carlo study of phonon transport in solid thin films including dispersion and polarization. *Journal of Heat Transfer*, 123(4):749–759, 2001.
- [49] Jaona Randrianalisoa and Dominique Baillis. Monte carlo simulation of cross-plane thermal conductivity of nanostructured porous silicon films. *Journal of Applied Physics*, 103(5):053502, 2008.
- [50] Renkun Chen, Allon I. Hochbaum, Pdraig Murphy, Joel Moore, Peidong Yang, and Arun Majumdar. Thermal conductance of thin silicon nanowires. *Physical Review Letters*, 101(10):105501, 2008.
- [51] Arden L. Moore, Sanjoy K. Saha, Ravi S. Prasher, and Li Shi. Phonon backscattering and thermal conductivity suppression in sawtooth nanowires. *Applied Physics Letters*, 93(8):083112, 2008.
- [52] Olivier Bourgeois, Thierry Fournier, and Jacques Chaussy. Measurement of the thermal conductance of silicon nanowires at low temperature. *Journal of Applied Physics*, 101(1):016104, 2007.

-
- [53] Aaron Szafer and A. Douglas Stone. Theory of quantum conduction through a constriction. *Physical Review Letters*, 62(3):300, January 1989.
- [54] E. G. Haanappel and D. van der Marel. Conductance oscillations in two-dimensional sharvin point contacts. *Physical Review B*, 39(8):5484, March 1989.
- [55] George Kirczenow. Theory of the conductance of ballistic quantum channels. *Solid State Communications*, 68(8):715–718, November 1988.
- [56] J. Seyler and M. N. Wybourne. Acoustic waveguide modes observed in electrically heated metal wires. *Physical Review Letters*, 69(9):1427, 1992.
- [57] T. S. Tighe, J. M. Worlock, and M. L. Roukes. Direct thermal conductance measurements on suspended monocrystalline nanostructures. *Applied Physics Letters*, 70(20):2687, 1997.
- [58] L. G.C Rego and G. Kirczenow. Quantized thermal conductance of dielectric quantum wires. *Physical Review Letters*, 81(1):232–235, 1998.
- [59] N. Mingo and Liu Yang. Phonon transport in nanowires coated with an amorphous material: An atomistic green’s function approach. *Physical Review B*, 68(24):245406, December 2003.
- [60] N. Mingo, D. Hauser, N. P. Kobayashi, M. Plissonnier, and A. Shakouri. “Nanoparticle-in-Alloy” approach to efficient thermoelectrics: Silicides in SiGe. *Nano Letters*, 9(2):711–715, 2009.
- [61] Jae Dong Chung and Massoud Kaviany. Effects of phonon pore scattering and pore randomness on effective conductivity of porous silicon. *International Journal of Heat and Mass Transfer*, 43(4):521–538, February 2000.
- [62] Ravi Prasher. Thermal conductivity of composites of aligned nanoscale and microscale wires and pores. *Journal of Applied Physics*, 100(3):034307, 2006.
- [63] Ronggui Yang, Gang Chen, and Mildred Dresselhaus. Thermal conductivity of simple and tubular nanowire composites in the longitudinal direction. *Physical Review B*, 72(12), 2005.
- [64] J.-H. Lee, J. C. Grossman, J. Reed, and G. Galli. Lattice thermal conductivity of nanoporous si: Molecular dynamics study. *Applied Physics Letters*, 91(22):223110, 2007.

-
- [65] Ronggui Yang and Gang Chen. Thermal conductivity modeling of periodic two-dimensional nanocomposites. *Physical Review B*, 69(19), 2004.
- [66] N. Mingo and D. A. Broido. Thermoelectric power factor of nanoporous semiconductors. *Journal of Applied Physics*, 101(1):014322, 2007.
- [67] G. Casella C. P. Robert. Monte Carlo statistical method. *Springer*, 1999.
- [68] D. J. Tildesley M.P Allen. Computer simulation of liquids. *Clarendon Press*, 1987.
- [69] K. Binder. Monte Carlo and molecular dynamic simulation in polymer science. *Oxford University Press*, 1995.
- [70] N. Metropolis, R. Bivins, M. Storm, Anthony Turkevich, J. M. Miller, and G. Friedlander. Monte Carlo calculations on intranuclear cascades. i. Low-Energy studies. *Physical Review*, 110(1):185, April 1958.
- [71] E.S. Oran, C.K. Oh, and B.Z. Cybyk. DIRECT SIMULATION MONTE CARLO: recent advances and applications1. *Annual Review of Fluid Mechanics*, 30(1):403–441, 1998.
- [72] Massimo V. Fischetti and Steven E. Laux. Monte Carlo analysis of electron transport in small semiconductor devices including band-structure and space-charge effects. *Physical Review B*, 38(14):9721, November 1988.
- [73] P. Lugli, P. Bordone, L. Reggiani, M. Rieger, P. Kocevar, and S. M. Goodnick. Monte Carlo studies of nonequilibrium phonon effects in polar semiconductors and quantum wells. i. laser photoexcitation. *Physical Review B*, 39(11):7852, April 1989.
- [74] M. V. Fischetti and S. E. Laux. Monte Carlo study of electron transport in silicon inversion layers. *Physical Review B*, 48(4):2244, July 1993.
- [75] J. R. Howell. The Monte Carlo method in radiative heat transfer. *Journal of Heat Transfer*, 120(3):547–560, 1998.
- [76] Tom Klitsner, J. E. VanCleve, Henry E. Fischer, and R. O. Pohl. Phonon radiative heat transfer and surface scattering. *Physical Review B*, 38(11):7576, October 1988.
- [77] Yunfei Chen, Deyu Li, Jennifer R. Lukes, and Arun Majumdar. Monte Carlo simulation of silicon nanowire thermal conductivity. *Journal of Heat Transfer*, 127(10):1129–1137, October 2005.

-
- [78] Ming-Shan Jeng, Ronggui Yang, David Song, and Gang Chen. Modeling the thermal conductivity and phonon transport in nanoparticle composites using monte carlo simulation. *Journal of Heat Transfer*, 130(4):042410–11, April 2008.
- [79] N. Mingo. Calculation of si nanowire thermal conductivity using complete phonon dispersion relations. *Physical Review B*, 68(11), 2003.
- [80] M. S. P. Lucas. Electrical conductivity of thin metallic films with unlike surfaces. *Journal of Applied Physics*, 36(5):1632–1635, May 1965.
- [81] M. G. Holland. Analysis of lattice thermal conductivity. *Physical Review*, 132(6):2461, December 1963.
- [82] W. A. Harrison. Electronic structure and the properties of solid. *Dover*, 1989.
- [83] B. Abeles, D. S. Beers, G. D. Cody, and J. P. Dismukes. Thermal conductivity of Ge-Si alloys at high temperatures. *Physical Review*, 125(1):44, January 1962.
- [84] B. Abeles. Lattice thermal conductivity of disordered semiconductor alloys at high temperatures. *Physical Review*, 131(5):1906, 1963.
- [85] N. Savvides and H. J. Goldsmid. Boundary scattering of phonons in fine-grained hot-pressed Ge-Si alloys. II. theory. *Journal of Physics C: Solid State Physics*, 13:4671–4678, 1980.
- [86] D. W. Song, W.-N. Shen, B. Dunn, C. D. Moore, M. S. Goorsky, T. Radetic, R. Gronsky, and G. Chen. Thermal conductivity of nanoporous bismuth thin films. *Applied Physics Letters*, 84(11):1883, 2004.
- [87] D. Broido and N. Mingo. Theory of the thermoelectric power factor in nanowire-composite matrix structures. *Physical Review B*, 74(19), 2006.
- [88] M. Ben-Chorin, F. M?ller, and F. Koch. Nonlinear electrical transport in porous silicon. *Physical Review B*, 49(4):2981, January 1994.
- [89] Alexander A. Balandin. Nanophononics: Phonon engineering in nanostructures and nanodevices. *Journal of Nanoscience and Nanotechnology*, 5:1015–1022, July 2005.
- [90] Lei Wang and Baowen Li. Phononics gets hot. *physics world*, 21:27–29, 2008.
- [91] Rusen Yang, Yong Qin, Liming Dai, and Zhong Lin Wang. Power generation with laterally packaged piezoelectric fine wires. *Nature Nanotechnology*, 4(1):34–39, 2008.

-
- [92] C. W. Chang, D. Okawa, A. Majumdar, and A. Zettl. Solid-State thermal rectifier. *Science*, 314(5802):1121–1124, November 2006.
- [93] Lei Wang and Baowen Li. Thermal logic gates: Computation with phonons. *Physical Review Letters*, 99(17):177208, October 2007.
- [94] M. M. Leivo and J. P. Pekola. Thermal characteristics of silicon nitride membranes at sub-Kelvin temperatures. *Applied Physics Letters*, 72(11):1305, 1998.
- [95] K. Schwab, E. A. Henriksen, J. M. Worlock, and M. L. Roukes. Measurement of the quantum of thermal conductance. *Nature*, 404(6781):974–977, April 2000.
- [96] C. S. Yung, D. R. Schmidt, and A. N. Cleland. Thermal conductance and electron-phonon coupling in mechanically suspended nanostructures. *Applied Physics Letters*, 81(1):31, 2002.
- [97] W. Fon, K. C. Schwab, J. M. Worlock, and M. L. Roukes. Phonon scattering mechanisms in suspended nanostructures from 4 to 40 k. *Physical Review B*, 66(4):045302, July 2002.
- [98] J. S. Heron, T. Fournier, N. Mingo, and O. Bourgeois. Mesoscopic size effects on the thermal conductance of silicon nanowire. *Nano Letters*, 9(5):1861–1865, May 2009.
- [99] Ravi Prasher. Acoustic mismatch model for thermal contact resistance of van der waals contacts. *Applied Physics Letters*, 94(4):041905, 2009.
- [100] Yann Chalopin, Jean-Numa Gillet, and Sebastian Volz. Predominance of thermal contact resistance in a silicon nanowire on a planar substrate. *Physical Review B*, 77(23):233309, June 2008.
- [101] Wei-Qing Huang, Ming-Liang Zou, Gui-Fang Huang, Jing-Jing Yao, and Wangyu Hu. Material properties dependence of ballistic phonon transmission through two coupled nanocavities. *Journal of Applied Physics*, 105(12):124305, 2009.
- [102] Li Shi, Deyu Li, Choongho Yu, Wanyoung Jang, Dohyung Kim, Zhen Yao, Philip Kim, and Arunava Majumdar. Measuring thermal and thermoelectric properties of One-Dimensional nanostructures using a microfabricated device. *Journal of Heat Transfer*, 125(5):881–888, October 2003.
- [103] Davide Donadio and Giulia Galli. Atomistic simulations of heat transport in silicon nanowires. *Physical Review Letters*, 102(19):195901, May 2009.

-
- [104] C. W. Chang, D. Okawa, H. Garcia, A. Majumdar, and A. Zettl. Nanotube phonon waveguide. *Physical Review Letters*, 99(4):045901, July 2007.
- [105] J. S. Heron, Chandan Bera, T. Fournier, N. Mingo, and O. Bourgeois. Blocking phonons via nanoscale geometrical design. *Submitted in PRB*.
- [106] R. Landauer. Spatial variation of currents and fields due to localized scatterers in metallic conduction. 10.1147/rd.13.0223, 1957.
- [107] Rolf Landauer. Can a length of perfect conductor have a resistance? *Physics Letters A*, 85(2):91–93, September 1981.
- [108] Yoseph Imry and Rolf Landauer. Conductance viewed as transmission. *Reviews of Modern Physics*, 71(2):S306, March 1999.
- [109] S datta. *Quantum Transport: Atom to Transistor*. Cambridge University Press, New York, 2005.
- [110] M. J. M. de Jong. Transition from sharvin to drude resistance in high-mobility wires. *Physical Review B*, 49(11):7778, March 1994.
- [111] Chun-Min Chang and Michael R. Geller. Mesoscopic phonon transmission through a nanowire-bulk contact. *Physical Review B*, 71(12):125304, March 2005.
- [112] H.B.G. Casimir. note on the conduction of heat in crystals. *Physica*, 5(6):495–500, June 1938.
- [113] R. Berman, F. E. Simon, and J. M. Ziman. The thermal conductivity of diamond at low temperatures. *Proceedings of the Royal Society of London. Series A. Mathematical and Physical Sciences*, 220(1141):171–183, November 1953.
- [114] Martin Knudsen. Die gesetze der molekularströmung und der inneren reibungsströmung der gase durch röhren. *Annalen der Physik*, 333(1):75–130, 1909.
- [115] M. v. Smoluchowski. Zur kinetischen theorie der transpiration und diffusion verdünnter gase. *Annalen der Physik*, 338(16):1559–1570, 1910.
- [116] Giri Joshi, Hohyun Lee, Yucheng Lan, Xiaowei Wang, Gaohua Zhu, Dezhi Wang, Ryan W. Gould, Diana C. Cuff, Ming Y. Tang, Mildred S. Dresselhaus, Gang Chen, and Zhifeng Ren. Enhanced thermoelectric Figure-of-Merit in nanostructured p-type silicon germanium bulk alloys. *Nano Letters*, 8(12):4670–4674, 2008.

-
- [117] X. W. Wang, H. Lee, Y. C. Lan, G. H. Zhu, G. Joshi, D. Z. Wang, J. Yang, A. J. Muto, M. Y. Tang, J. Klatsky, S. Song, M. S. Dresselhaus, G. Chen, and Z. F. Ren. Enhanced thermoelectric figure of merit in nanostructured n-type silicon germanium bulk alloy. *Applied Physics Letters*, 93(19):193121, 2008.
- [118] C. B. Vining, W. Laskow, J. O. Hanson, R. R. Vanderbeck, and P. D. Gorsuch. Thermoelectric properties of pressure-sintered Si_{0.8}Ge_{0.2} thermoelectric alloys. *J. Appl. Phys.*, 69:4333–4340, 1991.
- [119] J. P. Dismukes, L. Ekstrom, E. F. Steigmeier, I. Kudman, and D. S. Beers. Thermal and electrical properties of heavily doped Ge-Si alloys up to 1300[degree]K. *Journal of Applied Physics*, 35(10):2899–2907, October 1964.
- [120] B. Poudel, Q. Hao, Y. Ma, Y. Lan, A. Minnich, B. Yu, X. Yan, D. Wang, A. Muto, D. Vashaee, X. Chen, J. Liu, M. S. Dresselhaus, G. Chen, and Z. Ren. High-Thermoelectric performance of nanostructured bismuth antimony telluride bulk alloys. *Science*, 320(5876):634–638, 2008.
- [121] Wenjie Xie, Xinfeng Tang, Yonggao Yan, Qingjie Zhang, and Terry M. Tritt. Unique nanostructures and enhanced thermoelectric performance of melt-spun BiSbTe alloys. *Applied Physics Letters*, 94(10):102111, 2009.
- [122] M Soulier, C Navone, J Simon, M Plissonnier, G Delaizir, and C Godart. Enhanced thermoelectric performance of nanostructured bismuth antimony tellurium bulk alloys. In *First International Conference on Materials for Energy*, page 507, Convention Center Karlsruhe, Germany, 2010.
- [123] H. J. Goldsmid and A. W. Penn. Boundary scattering of phonons in solid solutions. *Phys. Lett. A*, 27:523–524, 1968.
- [124] J E Parrott. The thermal conductivity of sintered semiconductor alloys. *Journal of Physics C: Solid State Physics*, 2(1):147–151, 1969.
- [125] C. Wood. Materials for thermoelectric energy-conversion. *Rep. Prog. Phys.*, 51:459–539, 1988.
- [126] D. M. Rowe, V. S. Shukla, and N. Savvides. Phonon-scattering at grain-boundaries in heavily doped fine-grained silicon-germanium alloys. *Nature*, 290:765–766, 1981.
- [127] Cronin B. Vining. A model for the high-temperature transport properties of heavily doped n-type silicon-germanium alloys. *Journal of Applied Physics*, 69(1):331–341, January 1991.

- [128] Yucheng Lan, Austin Jerome Minnich, Gang Chen, and Zhifeng Ren. Enhancement of thermoelectric Figure-of-Merit by a bulk nanostructuring approach. *Advanced Functional Materials*, 20(3):357–376, 2010.
- [129] Alexis MATHIA. Etude du matériau thermoélectrique sigé de la poudre au dmonstrateur. *Thesis de doctorant, 2010, Institut Polytechnique de Grenoble*.
- [130] Michael Bozlar, Delong He, Jinbo Bai, Yann Chalopin, Natalio Mingo, and Sebastian Volz. Carbon nanotube microarchitectures for enhanced thermal conduction at ultralow mass fraction in polymer composites. *Advanced Materials*, 22(14):1654–1658, 2010.
- [131] P.G. Klemens and G.H. Briggs. The scattering of low-frequency lattice waves by static imperfections. *Proc. Phys. Soc. A*, 68(1113), 1955.
- [132] J. S. Reparaz, A. R. Go ni, A. Bernardi, M. I. Alonso, and M. Garriga. Measurement of phonon pressure coefficients for a precise determination of deformation potentials in SiGe alloys. *physica status solidi (b)*, 246(3):548–552, 2009.
- [133] C Bera, M Soulier, C Navone, J Simon, G Roux, N Mingo, and S Volz. Thermoelectric properties of nano structured sigé: potential for further improvement. *To be submitted in JAP*.
- [134] Glen A. Slack and Moayyed A. Hussain. The maximum possible conversion efficiency of silicon-germanium thermoelectric generators. *Journal of Applied Physics*, 70(5):2694–2718, 1991.
- [135] Srinivasan Krishnamurthy, A. Sher, and A.-B. Chen. Band structures of SixGe1-x alloys. *Physical Review B*, 33(2):1026, January 1986.
- [136] A. Minnich, H. Lee, X. Wang, G. Joshi, M. Dresselhaus, Z. Ren, G. Chen, and D. Vashaee. Modeling study of thermoelectric SiGe nanocomposites. *Physical Review B*, 80(15), 2009.
- [137] Srinivasan Krishnamurthy, A. Sher, and An-Ban Chen. Generalized brooks’ formula and the electron mobility in si[sub x]Ge[sub 1 - x] alloys. *Applied Physics Letters*, 47(2):160–162, July 1985.
- [138] D. L. Rode and S. Knight. Electron transport in GaAs. *Physical Review B*, 3(8):2534, April 1971.
- [139] G. D. Mahan and J. O. Sofo. The best thermoelectric. *Proceedings of the National Academy of Sciences*, 93(15):7436, 1996.

- [140] D. L. Rode. Electron mobility in Direct-Gap polar semiconductors. *Physical Review B*, 2(4):1012, 1970.
- [141] J. Bardeen and W. Shockley. Deformation potentials and mobilities in Non-Polar crystals. *Physical Review*, 80(1):72, October 1950.
- [142] Maurice Glicksman. Mobility of electrons in Germanium-Silicon alloys. *Physical Review*, 111(1):125, July 1958.
- [143] Nobuyuki Sugii, Shigefumi Irieda, Jun Morioka, and Taroh Inada. Recrystallization, redistribution, and electrical activation of strained-silicon/Si_{0.7}Ge_{0.3} heterostructures with implanted arsenic. *Journal of Applied Physics*, 96(1):261, 2004.
- [144] G. Kaiblinger-Grujin, H. Kosina, and S. Selberherr. Influence of the doping element on the electron mobility in n-silicon. *Journal of Applied Physics*, 83(6):3096, 1998.
- [145] D. L. Rode. Electron mobility in ge, si, and GAP. *Phys. Status Solidi (b)*, 53:245, 1972.
- [146] C. B. Vining, W. Laskow, J. O. Hanson, R. R. Vanderbeck, and P. D. Gorsuch. Thermoelectric properties of pressure-sintered Si_{0.8}Ge_{0.2} thermoelectric alloys. *J. Appl. Phys.*, 69:4333–4340, 1991.
- [147] G. Pernot, M. Stoffel, I. Savic, F. Pezzoli, P. Chen, G. Savelli, A. Jacquot, J. Schumann, U. Denker, I. Mönch, Ch. Deneke, O. G. Schmidt, J. M. Rampnoux, S. Wang, M. Plissonnier, A. Rastelli, S. Dilhaire, and N. Mingo. Precise control of thermal conductivity at the nanoscale through individual phonon-scattering barriers. *Nat Mater*, 9(6):491–495, June 2010.
- [148] Helene Michel, Younes Ezzahri, Ali Shakouri, Gilles Pernot, Jean-Michel Rampnoux, and Stefan Dilhaire. Coherent phonons spectroscopy in Si/SiGe superlattices. <http://adsabs.harvard.edu/abs/2010APS..MARX25005M>, March 2010.
- [149] A. J. Minnich, M. S. Dresselhaus, Z. F. Ren, and G. Chen. Bulk nanostructured thermoelectric materials: current research and future prospects. *Energy & Environmental Science*, 2(5):466, 2009.
- [150] Eberhard K. U. Gross, Reiner M. Dreizler, and North Atlantic Treaty Organization. Scientific Affairs Division. *Density functional theory*. Springer, March 1995.

Résumé

Propriétés Thermoélectriques de Matériaux Nanocomposites

Cette thèse présente une étude théorique du transport de chaleur dans les matériaux composites nanoporeux et nanofils ainsi qu'une étude théorique des propriétés thermoélectriques de l'alliage $Si_{0.8}Ge_{0.2}$ confrontée à des mesures expérimentales réalisées pour une partie, dans le cadre de l'étude

La première étude démontre que les alliages poreux affichent des réductions de conductivité thermique à des dimensions de pores beaucoup plus grandes que les matériaux poreux non alliés de même porosité nominale. Si on considère une taille de pores de 1000nm, la conductivité thermique de l'alliage $Si_{0.5}Ge_{0.5}$ avec 0.1 de porosité est deux fois plus faible que la conductivité thermique d'un matériau non poreux, alors que les pores plus petits que 100 nm sont nécessaires pour obtenir la même réduction relative dans le Si ou Ge pur. Nos résultats indiquent que les alliages nanoporeux devraient être avantageux devant les matériaux nanoporeux non alliés, et ceux pour les applications nécessitant une faible conductivité thermique, tels que les nouveaux matériaux thermoélectriques.

La deuxième étude théorique sur la conductance thermique de nanofils révèle l'effet de la structure sur le transport des phonons. Avec un modèle théorique qui considère la dépendance en fréquence du transport des phonons, nous sommes en mesure quantitativement de rendre compte des résultats expérimentaux sur des nanofils droits et coudés dans la gamme de température qui montre qu'un double coude sur un fil réduit sa conductance thermique de 40% à la température de 5K.

Enfin, nous avons procédé à une approche théorique des propriétés thermoélectriques des alliages SiGe frittés, en les comparant aux mesures expérimentales nouvelles et antérieures, tout en évaluant leur potentiel d'amélioration. L'approche théorique a été validée par comparaison de la mobilité prévue et la conductivité thermique prévues, en faisant varier la quantité de Ge et les concentrations de dopage, dans une gamme de température comprise entre 300 et 1000K. Nos calculs suggèrent qu'une optimisation par rapport à l'état de l'art actuel est possible pour le matériau de type n et type p, conduisant potentiellement à une augmentation de 6% (5%) du ZT à 1000K et 25% (4%) à température ambiante. Même des améliorations plus grande devrait être possible si la probabilité de diffusion des phonons aux joints de grains pouvait être augmentée au-delà de sa valeur actuelle de 10%.

Abstract

Thermo Electric Properties Of Nanocomposites Materials

This dissertation presents a theoretical study of heat transport in nanoporous composites and in nanowire and also theoretical study of thermoelectric properties of the $Si_{0.8}Ge_{0.2}$ alloy with some experimental new and old measurements.

The first study on the porous alloys show that its can display thermal conductivity reductions at considerably larger pore sizes than nonalloyed porous materials of the same nominal porosity. The thermal conductivity of $Si_{0.5}Ge_{0.5}$ alloy with 0.1 porosity becomes half the nonporous value at 1000 nm pore sizes, whereas pores smaller than 100 nm are required to achieve the same relative reduction in pure Si or Ge. Using Monte Carlo simulations, we also show that previous models had overestimated the thermal conductivity in the small pore limit. Our results imply that nanoporous alloys should be advantageous with respect to nanoporous nonalloys, for applications requiring a low thermal conductivity, such as novel thermoelectrics.

The second theoretical study on the nanowire thermal conductance reveals the structure effect on the phonon transport. With a theoretical model that considers the frequency dependence of phonon transport, we are able to quantitatively account for the experimental results of straight and bent nanowires in the whole temperature range which shows that due to an double bend on the straight thermal conductance reduced by 40% at temperature $5K$.

Finally, we theoretically investigate the thermoelectric properties of sintered SiGe alloys, compare them with new and previous experimental measurements, and determine their potential for further improvement. The theorwtical approach is validated by extensive comparison of predicted bulk mobility, thermopower, and thermal conductivity, for varying Ge and doping concentrations, in the $300 - 1000K$ temperature range. The effect of grain boundaries is then included for $Si_{0.8}Ge_{0.2}$ sintered nanopowders , and used to predict optimized values of the thermoelectric figure of merit at different grain sizes. Our calculations suggest that further optimization of current state of the art n-type (p-type) material would be possible, possibly leading to 6% (5%) ZT enhancement at 1000K and 25% (4%) at room temperature. Even larger enhancements should be possible if the phonon scattering probability of the grain boundaries could be increased beyond its present value of 10%.
